NEAR QUANTUM LIMITED CHARGE DETECTOR AND BEYOND

A Thesis

Submitted to the Faculty

in partial fulfillment of the requirements for the

degree of

Doctor of Philosophy

in

Physics and Astronomy

by

Juliang Li

DARTMOUTH COLLEGE

Hanover, New Hampshire

May 15, 2018

Examining Committee:

Alexander J. Rimberg (Chair)

Miles Blencowe

Chandrasekhar Ramanathan

F. Jon Kull
Dean of Graduate and Advanced Studies

Kurt Jacobs

Abstract

During last three decades, with advances in solid-state electronics and quantum computation science, highly sensitive electrometers have found wide applications in diverse fields. Various designs and experiments have been carried out for achieving higher sensitivity and faster measurement.

A novel charge detection technique based on dispersive measurement of the resonant frequency shift of a superconducting coplanar wave guide (CPW) resonator embedded with a Cooper pair transistor (CPT) is introduced. The resonator was shunted by the nonlinear inductance of the CPT. Change of charges of the CPT island charge modify the inductance of the CPT and consequently shift the resonant frequency of the resonator. By monitoring the frequency shift while varying the charge on the CPT, a new world record of charge sensitivity $2.1 \times 10^{-7} e/\sqrt{Hz}$ using 200 microwave photons has been achieved. The nonlinear resonator has also found application as a parametric amplifier for microwave signal amplification and nonclassical photon state generation. Gain of 20 dB with bandwidth of 10MHz has achieved by parametric pumping on the CPT.

Acknowledgement

There are many people without whom this thesis would not be possible. Most importantly to my advisor, Alexander Rimberg. He gave me the freedom to explore the amazing world of quantum physics. His guidance, knowledge and patience were invaluable during the process. I am also very grateful to Miles Blencowe and Sekhar Ramanathan for their guidance and amusing conversations in the basement of Wilder.

My appreciation extends to my lab mates Ben Brock, Billy Braasch, Bhargava Thyagarajan, Sisira Kanhirathingal, Chunyang Tang, and Fei Chen. Their help was vital and more importantly they make the working environment in the lab very enjoyable.

Many thanks to my advisor at Umass Boston Kurt Jacobs. His guidance and patience were invaluable for me when I started making the first step into quantum physics. I also thank Professor Stephen Arnason at UMass Boston for his encouragement and support of me pursuing my dream of physics.

Great thanks to my good friends I have made at Dartmouth, especially Jannis, Dhrubo, Chuyang, Marco, Mallory, Lihuang, Whitey, John and Jim. Their friendship supported and encouraged me through my PhD. They are part of of my life inside and outside of the physics lab.

Finally I owe a lot to my family, who have always support and encouraged me to continue pursuing my dream. The sweet voice of my niece on the other side of the phone line lit up my path when I was in the dark.

Contents

Abstract i

Acknowledge ii

Contents iii

List of Figures vi

1 INTRODUCTION 1

2 TRANSMISSION LINE RESONATOR 3

2.1 The LCR Oscillator 3

2.2 Transmission line 4

2.3 Capacitively coupled transmission line resonator 6

2.4 Coplanar Waveguide Cavities 8

2.4.1 Properties of the CPW 8

2.4.2 Loss in the CPW 9

3 COOPER PAIR TRANSISTOR 11

3.1 Josephson junction 11

3.2 Band Structure of the CPT 13

4 PHOTOLITHOGRAPHY & ELECTRON BEAM LITHOGRAPHY 22

4.1 PhotoLithography . . . 22
4.1.1 Design of CPW . . . 22
4.1.2 Substrate . . . 24
4.1.3 Fabrication Steps . . . 25
4.2 Ebeam Lithography . . . 26
4.3 Plasma Cleaning . . . 27
4.4 Printed Circuit Boards and Sample Holders . . . 30

5 JOSEPHSON PARAMETRIC AMPLIFIER 33

6 CHARGE SENSITIVITY 52
6.1 current biasing regime . . . 55
6.2 linear sensitivity limited by noise and the amplification chain . . . 60

7 EXPERIMENTAL SETUP 62
7.1 filtering of gate and flux line . . . 64
7.2 SLUG amplifier . . . 66

8 EXPERIMENT RESULT 68
8.1 JPA Characterization . . . 68
8.1.1 Phase Modulation . . . 68
8.1.2 Gain of flux and gate pump . . . 68
8.1.3 Noise floor lowering . . . 71
8.1.4 Stimulated Emission and resonant frequency shift . . . 72
8.1.5 Frequency shift by input signal . . . 74
8.2 Frequency shift by gate and flux . . . 75
8.3 phase response . . . 79
8.4 Emission suppression . . . 81
8.5 'Normal mode splitting' . . . 83

8.6 Charge Sensitivity Characterization 83
8.6.1 Carrier plus Stimulated emission 83
8.6.2 Maximum sensitivity spot 84
8.7 Noise Measurement 84

9 CONCLUSION AND FUTURE WORK 93
9.1 frequency shift quantification 93
9.2 quantum state tomography 94
9.3 squeezing 94
9.4 magnetometer 94

A Q FACTOR MEASUREMENT 95

B 4^{TH} ORDER CALCULATION 103

C SLOPED SIDE WALL GENERATION FOR THIN NIOBIUM FILM 112

D DOUBLE ANGLE EVAPORATION OF JOSEPHSON JUNCTION 115

References 119

List of Figures

2.1 a. A parallel RLC resonator . . . 3

2.2 a. A transmission line with characteristic impedance Z_0 and length L. b). The transmission line can be represented as an infinite series of L's and C's. (33) . . . 4

2.3 transmission line resonator with characteristic impedance Z_l capacitively couple to the measuring circuit with impedance Z_c . . . 7

2.4 Sketch of coplanar waveguide. The ratio s/a determines the impedance, Z_0. The extent of the ground planes should be much larger than s so that they can be approximated as infinite. (33) . . . 8

3.1 Illustration of CPT. It consists of two JJs and an island with the charge on the island tunned by the gate voltage . . . 11

3.2 Sketch of a single Josephson junction (JJ) . . . 12

3.3 Pairs of conjugate variables in the transistors. $k's$ are Cooper pair numbers, $n's$ are electron numbers. $\phi's$ are the phases across the junctions . . . 13

3.4 Band structure of CPT in the three state model. Only the ground and first excited state are shown for clarity. . . . 17

3.5 Super current calculated from three band model . . . 18

3.6 Modulation of Josephson inductance L_J, resonant frequency f_o, super current I by the flux bias at two charge states. . . . 19

3.7 Modulation of Josephson inductance (L_J, resoant frequency f_o, super current I) by charge at two flux bias state. . . . 20

3.8 Modulation of Josephson inductance L_J, resonant frequency f_o, super current I by charge at two other flux bias states. 21

4.1 Design of the CPW quarter wave resonator with embedded CPT. 23

4.2 the coupling finger capacitor in our resonator which controls the couple coeffcient between the resonator and the external measurement circuit. 24

4.3 NIKON 8 I-liner Stepper (**a.**) and RIE Unaxis 790 (**b.**) in the clean room of the University of Wisconsin Madison used in the photo lithography process. 25

4.4 Illustration of the effect of having a sloped side wall during Nb etching. 26

4.5 Illustration of the principle of shadown evaporation. 27

4.6 SEM JEOL JSM-7000F equiped with NPGS system for Ebeam lithography 29

4.7 Thermal evaporator used to deposit thin Al films for JJ fabrication. 30

4.8 SEM images of the CPT imbedded in the CPW. 31

4.9 PCB and holders provide connection to the sample with minimum introduction of noise. 31

5.1 A JJ embedded in a quarter wavelength CPW 34

5.2 wave vector k_1 and amplitude at two JJ locations for $E_J/E_C = 0.15$ 43

5.3 wave vector k_1 and amplitude at two JJ locations for $E_J/E_C = 0.30$ 44

5.4 wave vector k_1 as function of E_J and insertion location x_{cpt} 45

6.1 Illustration of dispersive charge detection using a nonlinear resonator 53

6.2 A SQUID loop formed with two JJs. There is an internal current I_{loop} going on all the time and it determines the external current I_{ext} that could pass through the loop without biasing the JJs out of superconducting regime, or the other way around. 56

6.3 I_{ext} and loop inductance $L_{J,loop}$. Phase in the loop $\approx \pi$ 58

7.1 measurement setup in our dilution refrigerator. The lines to the right of the drawing are for a Y factor measurement of noise and gain calibration of the amplifier chain. 63

7.2 Dilution refrigerator setup. 64

7.3 The SLUG amplifier gain profiles and flux modulation of output voltage 66

8.1 Phase modulation of the gain of the JPA. It is a general proof that JPA is phase sensitive amplifier. 69

8.2 Gain of JPA by flux pump as function of pumping amplitude 70

8.3 Gain of JPA by gate pump as function of pumping amplitude 70

8.4 the stimulated emission from flux pumping 71

8.5 the stimulated emission power and frequency shift with various pump power at f_o = 5.756 GHz 73

8.6 Stimulated emission power and frequency shift for various pump power at $f_o = 5.766$ GHz 73

8.7 Stimulated emission power and frequency shift for various pump power at $f_o = 5.776$ GHz 74

8.8 Stimulated emission power and frequency shift for various pump powers at $f_o = 5.746$ GHz 75

8.9 frequency shift by the NA probing power at various resonant frequency point 76

8.10 frequency shift by flux bias at three charge states 77

8.11 frequency shift by gate biasing at three charge states of the CPT 79

8.12 3D plot of frequency shift by flux and gate bias 80

8.13 frequency shift shown in the coulomb blockade and charge degeneracy regime 81

8.14 **a.)** The foot ball traced out for specific frequency shift for a CPB capacitively coupled to a linear resonator through quantum capacitance. **b.**) The saddle traced out for specific frequency shift for a CPT inductively coupled to a linear resonator. The saddle marked out with yellow color is +20 MHz resonant frequency shift and the saddle with cyan color is −20 MHz resonant frequency shift. 82

8.15 Phase shift of the resonator for various flux and charge biasing. The phase data was recorded as expanded phase. 87

8.16 Phase shift and amplitude at various phase of CPT. 88

8.17 Reflection amplitude, phase change when the resonator went through critical coupling transition. The 3^{rd} polar plot shows that the circumference of the resonance circle will cross over the origin and sits right on the origin at critical coupling condition. The amplitudes of the three different coupling regime have been shifted to show the change in the resonance amplitude. 88

8.18 The amplitudes of the three different coupling regime have been shifted to show the change in the resonance amplitude. 89

8.19 Activated emission by activating signal and stimulated emission. 89

8.20 The amplitudes of the three different coupling regime have been shifted to show the change in the resonance amplitude. 90

8.21 Side bands by charge modulation on the gate 90

8.22 Side bands by charge modulation on the gate at maximum charge sensitivity 91

8.23 Simulated side bands by charge modulation on the gate 91

8.24 Illustration of Y-factor measurement 92

A.1 frequency sweep response of the resonator in polar format. The resonator traced out a circle around the resonance frequency f_o 97

A.2 Phase response around the resonance point. The sloped phase away from the resonance point indicates the cable delay and can be used to correct the cable delay after a linear fit 98

A.3 After correcting the cable delay the phase away from the resonance point become a flat line. 98

A.4 After correcting the cable delay, the two cross over curves away from the resonance shrink to minimize size 99

A.5 resonance circles with various coupling reactance. With larger coupling reactance the cirlce rotats further away from the real axis and shrink to a smaller diameter at the same time. 100

A.6 Resonance circles with various coupling reactances. With larger coupling reactance the cirlce rotats further away from the real axis and shrinks to a smaller diameter at the same time. 101

C.1 SEM image of Nb film after 12 minutes plasma etch. There was ≈ 20nm over etch on the Si substrate, the side wall has about 45 degree slope 113

C.2 SEM image of Nb film after 10 minutes plasma etch. The bright thin layer shows the Nb film was under etched 113

C.3 SEM image of Nb film after 15 minutes plasma etch. Over-etch on the Si substrate was more than 100 nm 114

D.1 Illustration of double angle evaporation 116

D.2 SET fabricated with double angle method with line width of ≈ 50 nm 117

D.3 SET fabricated with double angle method with larger tilting angle. The brighter parts to the right end of the horizontal patterns are Al film deposited on the resist wall, which become floating pieces after liftoff 118

Chapter 1

INTRODUCTION

Noninvasive charge detection has emerged as an important tool for uncovering new physics in nanoscale devices at the single-electron level or for high fidelity qubit-specific quantum state readout that is required for the implementation of a quantum computer. The single-electron transistor or SET uses the quantum phenomenon of tunneling to measure and control the movement of single electrons. Due to its capability of manipulating single electrons the SET is the most fundamental nanoscale single charge detector. (11) (3). However, SET is bandwidth limited by the resistance-capacitance product of the SET resistance and parasitic lead capacitance and is susceptible to $1/f$ noise.

Implemented in a resonant circuit, the radio-frequency single-electron transistor (RF-SET) matches the impedance of the SET to the characteristic impedance of microwave coaxial line and is the most sensitive and fastest charge detector to date. It has typical bandwidth of 10 MHz and a charge resolution of the order of $10^{-6}e/\sqrt{Hz}$ (32). RF-SET also works at high frequencies so that the $1/f$ noise effect is negligible. However, the RF-SET uses Josephson junctions (JJs) at a large voltage bias instead of on the supercurrent branch is susceptible to shot noise and heating effects from the quasiparticles and will have strong back action on the system connected to it. This uncontrolded electromagnetic back-action

can be completely avoided by using superconducting version of devices (SCDs), such as superconducting Cooper pair transistor (sCPT) (43), or Cooper pair boxes (CPB) (38).

An alternate approach to charge-state detection is based on the dispersive signal frequency shift from the quantum capacitance when electrons undergo tunneling. Dispersive measurement introduces less back action on the measured system and has found wide applications in a variety of quantum systems, including electrometers(**?**), superconducting qubits (39), and nanomechanical devices (22). When implemented as charge detector, it can in principle reach quantum mechanical limits for sensitivity (8)

We carried out charge detection based on dispersive measurement employing the nonlinear Josephson inductance of the CPT. It offers higher charge sensitivity using many fewer microwave photons than the RF-SET and promises to enable strong photon phonon coupling when a mechanical resonator is capacitively coupled to the gate of the CPT. (30)

The thesis is organized as follows: Chapter 2 describes the theory and design details of CPW resonator, Chapter 3 is about the CPT whose nonlinear Josephson inductance (L_J) can be tuned by the charge state of its island, Chapter 4 covers technical details of fabricating the CPW and CPT, Chapter 5 gives the theoretical framework of our Josephson parametric amplifier (JPA), Chapter 6 discusses the theoretical bases for the charge sensitivity; and Chapter 7 gives the is experimental setup of our measurement; Chapter 8 gives our experimental result. It covers the characterization of our nonlinear resonator, JPA gain and bandwidth, and the charge sensitivity as well as additional nonlinear effects we observed during our charge characterization. Chapter 9 gives our conclusions and future research directions based on current observations.

Chapter 2

TRANSMISSION LINE RESONATOR

2.1 The LCR Oscillator

When a capacitor C inductor L and resistor R are connected together in parallel as in Fig.2.1, the input impedance is calculated as

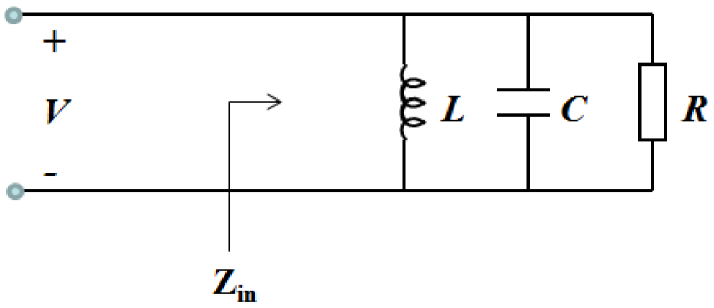

Figure 2.1: a. A parallel RLC resonator

$$Z_{\text{in,lcr}} = \left(\frac{1}{R} + \frac{1}{j\omega L} + j\omega C\right)^{-1} \tag{2.1}$$

Near the resonant frequency $\omega_o = 1/\sqrt{LC}$ the impedance of the inductor L equals to the impedance of the capacitor C, and by writing $\omega = \omega_o + \Delta\omega$, above equation can be rewritten

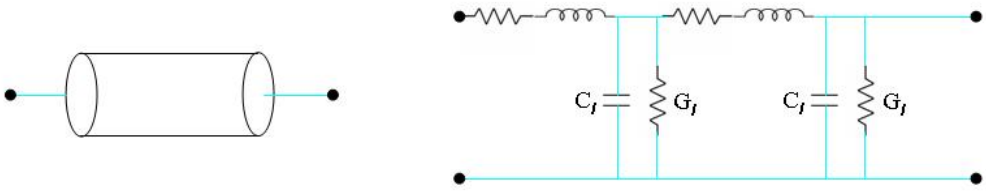

Figure 2.2: a. A transmission line with characteristic impedance Z_0 and length L. b). The transmission line can be represented as an infinite series of L's and C's. (33)

as

$$Z_{\text{in,lcr}} \approx \frac{R}{1 + 2jQ_o\Delta\omega/\omega_o} \tag{2.2}$$

with the internal quality factor Q_o defined as $Q_o = \omega_o RC$.

2.2 Transmission line

Reviewing transmission line theory of Pozar (28), A transmission line can be modeled as consisting of many small lumped elements that have the same impedances per unit length as the transmission line as shown in Fig. 2.2 (28).

where $R_l, L_l, G_l$and C_l are the resistance, inductance, conductance and capacitance per unit length of the transmission line.

with complex propogation constant

$$\gamma \quad = \quad \alpha + j\beta = \sqrt{(R_l + j\omega L_l)(G_l + j\omega C_l)} \tag{2.3}$$

and characteristic impedance

$$Z_o = \sqrt{\frac{R_l + j\omega L_l}{G_l + j\omega C_l}} \tag{2.4}$$

$$= \sqrt{\frac{L_l}{C_l}} \tag{2.5}$$

for a lossless line.

In our system, the transmission line resonator is a short circuited quarter wavelength resonator. Compared to a full wavelength resonator, the capacitance of the quarter wavelength is given as $C_{\lambda/4} = \frac{1}{4}C_\lambda$. By the relation $\omega_0 = \frac{1}{\sqrt{LC}}$ when oscillating at the same resonant frequency, $L_{\lambda/4} = 4L_\lambda$. A larger inductance will give a stronger cavity pull and a better performance. The inductance as well as other characteristic parameters of the quarter wavelength transmission line are calculated with the following steps.

The input impedance is (28)

$$Z_{in} = Z_0 \tanh\,(\alpha + j\beta)l \tag{2.6}$$

$$= Z_0 \frac{\tanh\,\alpha l + j\tan\,\beta l}{1 + j\tan\,\beta l\,\tanh\,\alpha l} \tag{2.7}$$

$$= Z_0 \frac{1 - j\tanh\,\alpha l\,\cot\,\beta l}{\tanh\,\alpha l - j\cot\,\beta l} \tag{2.8}$$

with $Z_0 = \sqrt{L_l C_l}$, the complex propagation coefficient $\gamma = \sqrt{(R_l + j\omega L_l)(G_l + j\omega C_l)}$, the attenuation constant $\alpha = Re[\gamma] \approx (R_l/Z_0 + G_l Z_0)/2$ and the phase $\beta = Im[\gamma]$. Consider only the fundamental mode of $\omega = \omega_{\lambda/4}$, $l = \lambda/4$ and let $\omega = \omega_{\lambda/4} + \Delta\omega$. Then, for a TEM line,

$$\beta l = \frac{\omega_{\lambda/4} l}{v_p} + \frac{\Delta\omega l}{v_p} = \frac{\pi}{2} + \frac{\pi\Delta\omega}{2\omega_{\lambda/4}} \tag{2.9}$$

When working in superconducting situation, the transmission line is near to the lossless

case so that $\tanh \alpha l \simeq \alpha l$. Also,

$$\cot\beta l = \cot(\frac{\pi}{2} + \frac{\pi\Delta\omega}{2\omega_{\lambda/4}}) = -\tan\frac{\pi\Delta\omega}{2\omega_{\lambda/4}} \simeq \frac{-\pi\Delta\omega}{2\omega_{\lambda/4}} \tag{2.10}$$

Substituting into equation 2.8 gives

$$Z_{in} = Z_0\frac{1 + j\alpha l\pi\Delta\omega/2\omega_{\lambda/4}}{\alpha l + j\pi\Delta\omega/2\omega_{\lambda/4}} \tag{2.11}$$

$$\simeq \frac{Z_0}{\alpha l + j\pi\Delta\omega/2\omega_{\lambda/4}} \tag{2.12}$$

as $\alpha l\pi\Delta\omega/2\omega_0 << 1$.

Comparing equation 2.12 to equation 2.1 we can see

$$\omega_0 = \omega_{\lambda/4} \tag{2.13}$$

$$R = Z_0/\alpha l \tag{2.14}$$

$$C = \frac{\pi}{4Z_0\omega_0} \tag{2.15}$$

$$L = \frac{1}{\omega_0^2 C} = \frac{4Z_0}{\pi\omega_0} \tag{2.16}$$

$$Q = \omega_0 RC = \frac{\pi}{4\alpha l} = \frac{\beta}{2\alpha} \tag{2.17}$$

$$\tag{2.18}$$

since $l = \pi/2\beta$ at resonance.

2.3 Capacitively coupled transmission line resonator

In our setup, the transmission line resonator was connected to the measurement circuit through a coupling finger capacitor as indicated in Fig.2.3. For a high Q resonator system, the resonator itself has a much higher internal Q than the measurement circuit. If it is

connected to the measurement circuit directly, the Q will degrade significantly and the energy in the resonator will be lost to the outside very quickly. The coupling capacitor creates an impedance mismatch so the photons in the resonator will bounce back and forth multiple times before escaping to the outside.

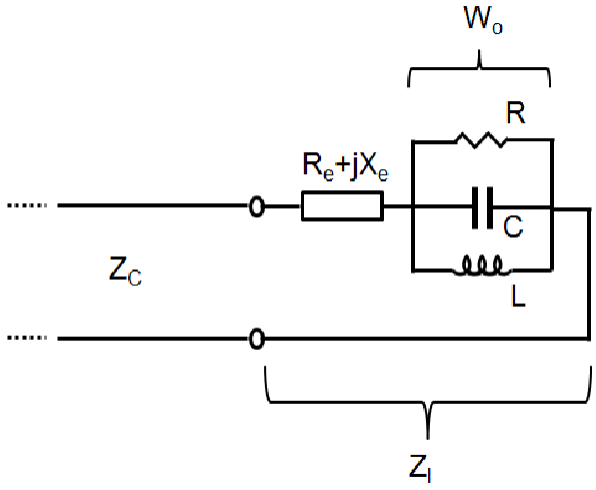

Figure 2.3: transmission line resonator with characteristic impedance Z_l capacitively couple to the measuring circuit with impedance Z_c

Including the coupling capacitor the total reflection coefficient Γ_i is given as

$$\Gamma_i = ae^{-2\pi j f \tau}\Gamma_d \left[\frac{1-\kappa+j2Q_o\delta_i - jX_eR_o/(Z_o^2+X_e^2)}{1+\kappa+j2Q_o\delta_i - jX_eR_o/(Z_o^2+X_e^2)}\right] \tag{2.19}$$

$$= ae^{-2\pi j f \tau}\Gamma_d \left[1-\frac{\frac{2\kappa}{1+\kappa}}{1+j2Q_L\delta_L}\right] \tag{2.20}$$

where Γ_d is the detuned reflection coefficient when the frequency is far away from the resonant frequency f_o, and κ is the coupling coefficient defined as $\kappa = Q_i/Q_L$. It is determined by the coupling capacitor or inductor. Procedure for measuring the loaded Q_L and internal Q_i is given in Appendix A.

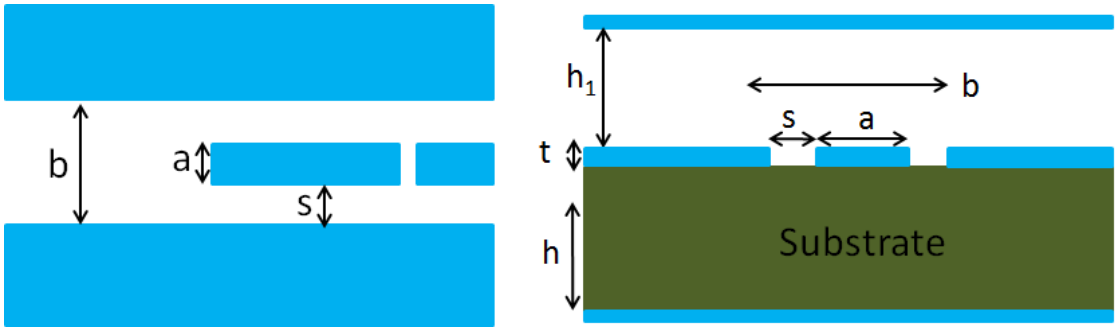

Figure 2.4: Sketch of coplanar waveguide. The ratio s/a determines the impedance, Z_0. The extent of the ground planes should be much larger than s so that they can be approximated as infinite. (33)

2.4 Coplanar Waveguide Cavities

In reality, the transmission line parameters are geometry dependent and one physical realization of transmission line needs to be chosen. Compared to other types as coplanar stripline (CPS) and microstrip, coplanar waveguide cavities (CPW) have convenient grounding which is essential for our purpose. The CPW has its center conduction pin and its ground in the same plane separated by a cap between them as shown in Fig.2.4. The separation gap could easily be adjusted from microns to millimeters scale with not much impedance variation, which facilitates Ebeam lithography in the following step. So the CPW will be the physical realization of the transmission line for our system.

2.4.1 Properties of the CPW

Properties of the CPW with finite dielectric thickness and cover shield, especially like impedance Z_o and phase velocity v is geometry depend and given by (15)

$$Z_o^{CPW} = \frac{60\pi}{\sqrt{\epsilon_{re}}} \frac{1}{K(k_1)/K'(k_1) + K(k_5)/K'(k_5)} \tag{2.21}$$

$$v = \frac{c}{\sqrt{\epsilon_{re}}} \tag{2.22}$$

with

$$k_1 = a/b \tag{2.23}$$

$$k_2 = \frac{\sinh(\pi a/4h)}{\sinh(\pi b/4h)} \tag{2.24}$$

$$k_5 = \frac{\tanh(\pi a/4h_1)}{\tanh(\pi b/4h_1)} \tag{2.25}$$

$$q = \frac{K(k_2)/K'(k_2)}{K(k_1)/K'(k_1) + K(k_5)/K'(k_5)} \tag{2.26}$$

$$\epsilon_{re} = 1 + q(\epsilon_r - 1) \tag{2.27}$$

ϵ_r is the dielectric constant of the substrate. K is the complete elliptic integral of the 1^{st} kind, which was calculated with MATLAB function 'ellipke'. Effect of the cover shield is inclued in the calculation of Equation (2.25)

2.4.2 Loss in the CPW

Three types of losses are present in CPW: dielectric, ohmic and radiation loss. Following reference (15) the dielectric loss is calculated as

$$\alpha_d = 2.73 \frac{\epsilon_r}{\sqrt{\epsilon_{re}}} \frac{\epsilon_{re} - 1}{\epsilon_r - 1} \frac{\tan\delta}{\lambda_o} \quad \text{dB/unit length} \tag{2.28}$$

with $\tan\delta$ the loss tangent. Ohmic loss is calculated as

$$\alpha_c^{CPW} = \frac{8.68 R_s \sqrt{\epsilon_{re}}}{480\pi K(k_1) K(k_1')(1-k_1^2)} \left\{ \frac{1}{a}\left[\pi + ln\left(\frac{8\pi a}{t}\frac{1-k_1}{1+k_1}\right)\right] + \frac{1}{b}\left[\pi + ln\left(\frac{8\pi b}{t}\frac{1-k_1}{1+k_1}\right)\right]\right\} \quad \text{dB/unit length} \tag{2.29}$$

which should be negligible for superconducting case. Radiation loss should have been minimized as we coated the internal surface of the sample box with a microwave absorbent

layer. The calculated losses are:

$$\begin{aligned} \alpha_d &= 0.0017 \quad \text{dB/unit length} \\ \alpha_c &\approx 0 \quad \text{dB/unit length (for lossless case)} \end{aligned} \tag{2.30}$$

And the corresponding internal quality factor $Q_i = 9,235$. It degraded to $Q_i = 1546$ after introducing Cooper pair transistor (CPT) into the CPW. Apparently the CPT added extra loss to the CPW resonator.

Chapter 3

COOPER PAIR TRANSISTOR

The Cooper-pair transistor (CPT) consists of two nanoscale superconducting Josephson junctions connected in series as shown in Fig.3.1 Due to its small size, the energy for adding a charge to the island is large so the electron transport through the junctions is controlled by the capacitvely coupled gate. The CPT can be regarded as a single Josephson-like element but with an extra charge degree of freedom.

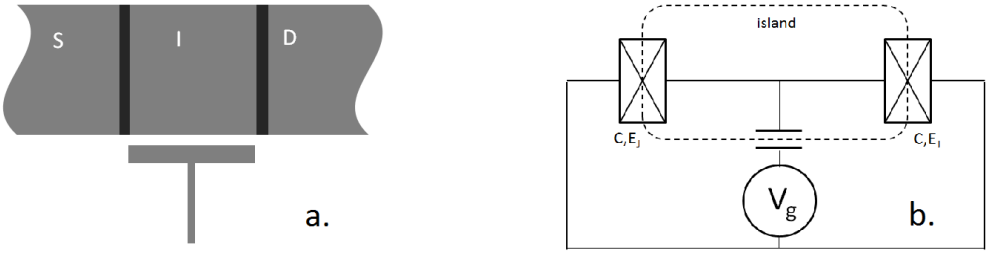

Figure 3.1: Illustration of CPT. It consists of two JJs and an island with the charge on the island tunned by the gate voltage

3.1 Josephson junction

A Josephson junction consists of two superconducting films separated by a thin insulating layer. The insulating layer is thin enough that the wave functions of the charge on

either side overlap and the Cooper pairs have a finite probability of tunneling through the barrier. Brian Josephson made the statement that the junction support a dissipationless supercurrent at zero voltage (19).

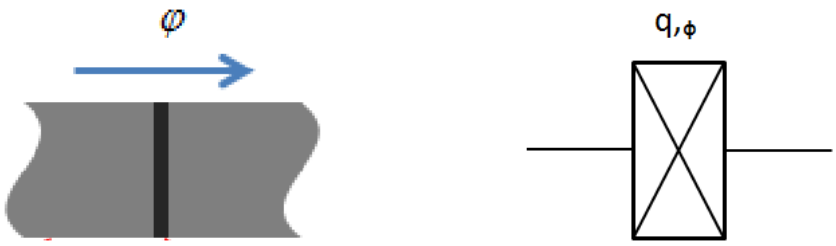

Figure 3.2: Sketch of a single Josephson junction (JJ)

The two fundamental equations governing the Cooper pair transport through a JJ is

$$I = I_o \sin\phi \tag{3.1}$$

$$V = \frac{\hbar}{2e}\dot{\phi} \tag{3.2}$$

where ϕ is the phase across the junction.

From above two equations we can see that the JJ has Josephson inductance L_J and Josephson energy E_J

$$L_J = \frac{L_{J_o}}{\cos(\phi)} \tag{3.3}$$

$$E_J = E_{J_o}\cos(\phi) \tag{3.4}$$

With $L_{J_o} = \hbar/2eI_o$ and $E_{J_o} = \hbar I_o/2e$. The critical current is given as (2)

$$I_o = \frac{2}{eR_N}\frac{\Delta_1\Delta_2}{\Delta_1+\Delta_2}K\left(\frac{|\Delta_1-\Delta_2|}{\Delta_1+\Delta_2}\right) \tag{3.5}$$

where Δ_1 and Δ_2 are the superconducting gap energy of the conductors on either side of the insulating barrier, R_N is the room temperature resistance of the junction, and K is the

complete elliptic integral of the first kind. With uniform superconductors on either side, $\Delta_1 \sim \Delta_2$, $K \to \pi/2$ and

$$I_o \approx \frac{\pi}{eR_N}\frac{\Delta_1}{2} \tag{3.6}$$

3.2 Band Structure of the CPT

Fig. 3.1(b) shows that the gate capacitor and the two junction capacitors forms a charge island with charging energy E_c or single-electron Coulomb blockade energy (13) that will tune the overall supercurrent and consequently the Josephson inductance in the transistor.

$$E_c = \frac{e^2}{2C_\Sigma} \tag{3.7}$$

where

$$C_\Sigma = C_{J_1} + C_{J_2} + C_g \tag{3.8}$$

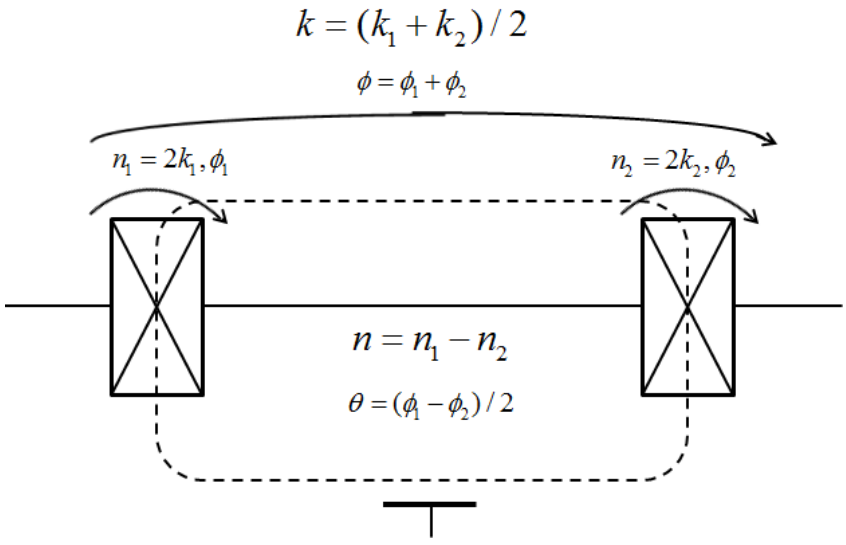

Figure 3.3: Pairs of conjugate variables in the transistors. $k's$ are Cooper pair numbers, $n's$ are electron numbers. $\phi's$ are the phases across the junctions

The transistor has two internal degree of freedom and we could chose the total number of Cooper pairs k and the total phase ϕ across the two junctions as the two internal degrees of freedom, or the excess number of electrons on the island n and the phase difference θ and they obey the following commutation relationship.

$$[\phi_1, k_1] = [\phi_2, k_2] = [\theta, n/2] = [\phi, k] = i \tag{3.9}$$

As the island charge n will be fixed by the gate bias its conjugate θ will consequently have large fluctuation. On the other hand, the overall phase is well defined as it is well controled by the environment or the flux bias in the SQUID loop for our case.

The Hamiltonian of the CPT has the form:

$$H = H_{J1} + H_{J2} + H_{CB} + H_{QP} \tag{3.10}$$

where $H_{CB} = E_c(n - n_g)^2$ is the electrostatic or kinetic Hamiltonian of the system and E_c is the charging energy of a single electron e on the island, and $n_g = C_g V_g / e$ is the number of charges induced by the gate bias. H_{J1} and H_{J2} are the Josephson coupling Hamiltonians or potential Hamiltonians of the two junctions. We assume the two junctions are identical so $H_{J1} = H_{J2}$; the Hamiltonians are defined as $H_{J1} = -E_{J1}\cos\phi_1$, $H_{J2} = -E_{J2}\cos\phi_2$. H_{QP} is the Hamiltonian due to the quasi particle poisioning in the system. It serves to break the Cooper pairs and make the system dissipative. We will ingnore it temperaryly and focus on retrieving the energy band structure of the CPT. Substituting everything for H_{CB}, H_{J1} and H_{J2} in and the total Hamiltonian becomes

$$H = E_c(n - n_g)^2 - 2E_J \cos\frac{\phi}{2}\cos\theta \tag{3.11}$$

Writing the Hamiltonian in the charge basis and applying $e^{i\theta}|n\rangle = |n+2\rangle$,$e^{-i\theta}|n\rangle = |n-2\rangle$ gives,

$$H = \begin{bmatrix} E_c(-n_g)^2 & -E_J\cos\frac{\phi}{2} \\ -E_J\cos\frac{\phi}{2} & E_c(2-n_g)^2 \end{bmatrix}$$

Comparing to perturbation theory (14), $W_{aa} = E_c(-n_g)^2$, $W_{bb} = E_c(2-n_g)^2$, $W_{ab} = -E_J\cos\frac{\phi}{2}$ and the eigen energy of the two states or bands are

$$E_\pm = \frac{1}{2}\left[W_{aa} + W_{bb} \pm \sqrt{(W_{aa}-W_{bb})^2 + 4|W_{ab}|^2}\right] \tag{3.12}$$

$$= E_c((n_g-1)^2+1) \pm \sqrt{4E_c^2(1-n_g)^2 + E_J^2\cos^2\frac{\phi}{2}} \tag{3.13}$$

The critical current I_o and Josephson inductance L_J is given as:(35)

$$I_o = \frac{1}{\Phi_o}\frac{\partial\varepsilon(n_g,\delta)}{\partial\delta} \tag{3.14}$$

$$L_J = \frac{1}{\Phi_o^2}\frac{\partial^2\varepsilon(n_g,\delta)}{\partial\delta^2} \tag{3.15}$$

I_o and L_o can be calculated numerically from the two band eigenenergy model. More bands need to be included for higher accuracy. A three band model has been solved analytically and given as: (20)

$$\varepsilon_m(\phi,n_g) = \left(\frac{8}{3}+n_g^2\right)E_c + \sqrt{4\lambda}\cos\left(\frac{\phi+2\pi(m+1)}{3}\right) \text{with} \quad m=0,1,2 \tag{3.16}$$

and

$$\lambda = \frac{2}{3}a + \frac{16}{3}E_c^2\left(\frac{1}{3} + n_g^2\right) \tag{3.17}$$

$$= \frac{2}{3}E_J^2\cos^2\left(\frac{\phi}{2}\right) + \frac{16}{3}E_c^2\left(\frac{1}{3} + n_g^2\right) \tag{3.18}$$

$$\mu = \frac{8}{3}aE_c + \frac{128}{3}E_c^3\left(\frac{1}{9} - n_g^2\right) \tag{3.19}$$

$$= \frac{8}{3}E_J^2E_c\cos^2\left(\frac{\phi}{2}\right) + \frac{128}{3}E_c^3\left(\frac{1}{9} - n_g^2\right) \tag{3.20}$$

$$\theta = \operatorname{acos}\left(\frac{-\mu}{2\lambda^{3/2}}\right) \tag{3.21}$$

$$= \operatorname{acos}\left(-\frac{\frac{8}{3}E_J^2E_c\cos^2\left(\frac{\phi}{2}\right) + \frac{128}{3}E_c^3\left(\frac{1}{9} - n_g^2\right)}{2\left(\frac{2}{3}E_J^2\cos^2\left(\frac{\phi}{2}\right) + \frac{16}{3}E_c^2\left(\frac{1}{3} + n_g^2\right)\right)^{3/2}}\right) \tag{3.22}$$

$$a = \frac{1}{2}\left(E_J^2 + E_J^2\cos(\phi)\right) \tag{3.23}$$

$$= E_J^2\cos^2\left(\frac{\phi}{2}\right) \tag{3.24}$$

The first two eigenenergy bands calculated from the three band model for various E_J/E_c ratio is displayed in Fig.3.4. Modulation of the eigenenergy by the phase of the CPT and the charge on the island varies with the E_J/E_c ratio. Fig.3.5 shows supercurrent I_o calculated from the three band model.

To better show the modulation of L_J by phase and charge. We simulated the frequency shift of our CPW resonator by L_J using our resonator parameters also and plotted L_J, f_o and supercurrent I for comparison in Fig.3.6. L_J is only plotted partially as the maximum is infinite. The left panels correspond to the Coulomb blockade regime and the right panels are at the charge degeneracy point. Frequency modulation by the phase is stronger near the degeneracy regime. The frequency shift matches very well with our experimental data as in Fig.8.10. More importantly it shows the L_J and supercurrent I values for a specific frequency shift. At zero frequency shift L_J switches from positive to negative infinity instantaneously while the supercurrent I gains its maximum value. These match with

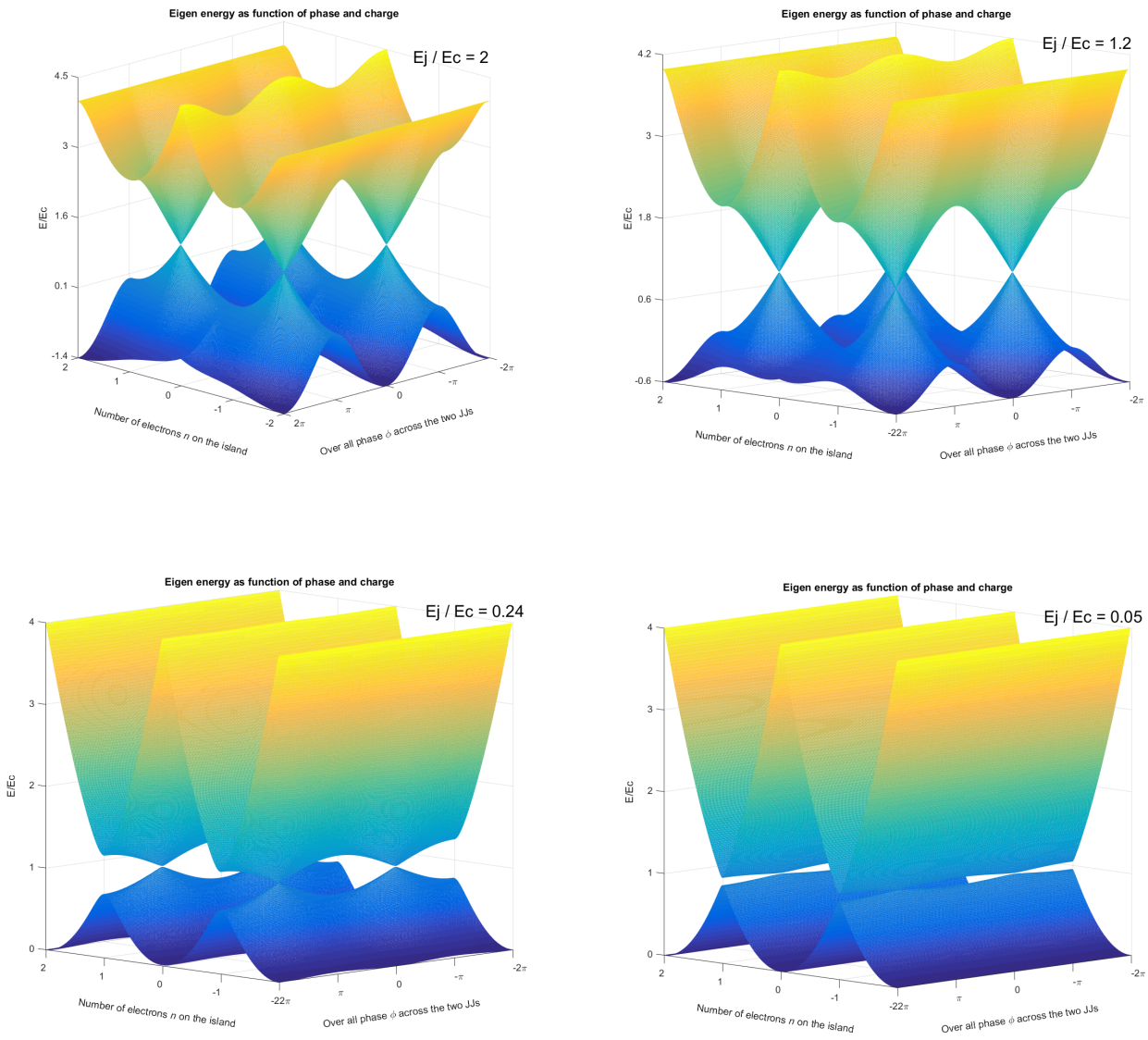

Figure 3.4: Band structure of CPT in the three state model. Only the ground and first excited state are shown for clarity.

our expectation for our system after gaining the frequency shift data.

Fig.3.7 are simulated frequency shift by charge variation at various flux biasing points where charge modulation switches sign at the two flux biasing points. L_J is only plotted partially. At the left flux bias state frequency shift by the charge is upward (shift to higher frequency). While at the right flux bias state the frequency shift by the charge is

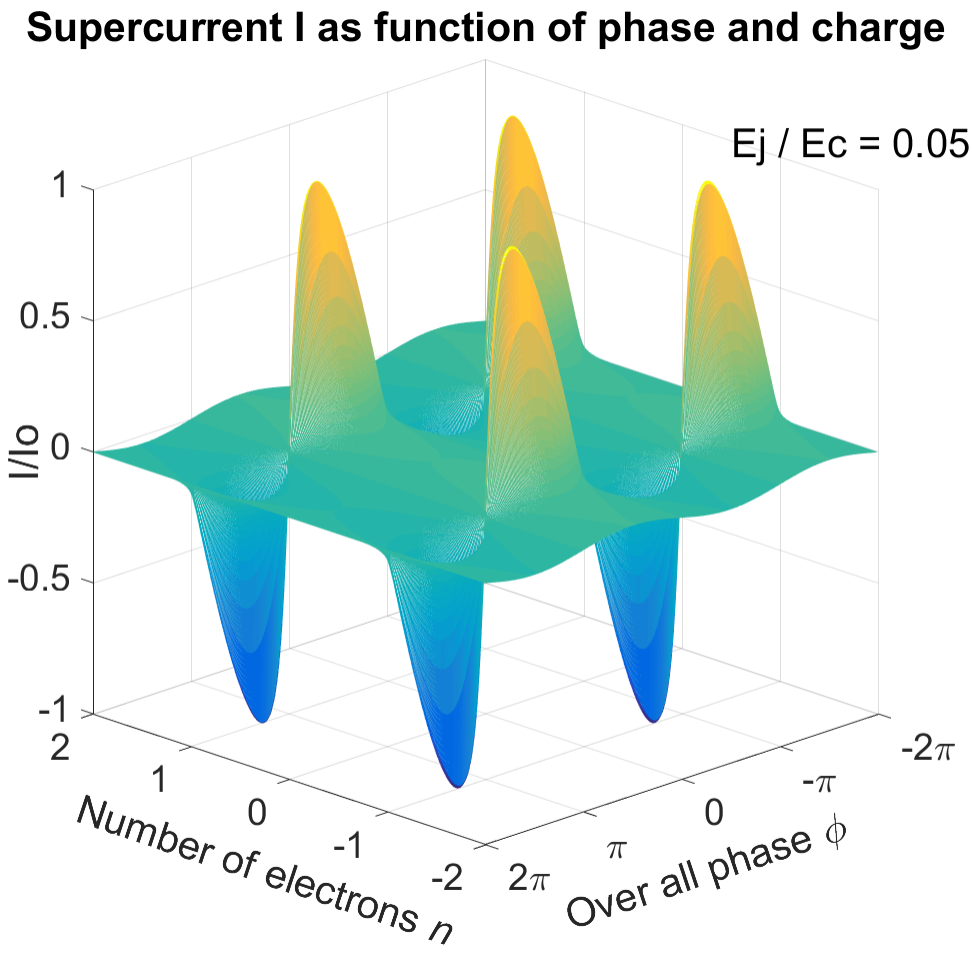

Figure 3.5: Super current calculated from three band model

downward.

Figure (3.8) is frequency shift charge modulation by another two flux biasing points where the charge modulation is at its minimum and maximum. At the left flux bias state frequency shift by the charge is minimum. While at the right flux bias state the frequency shift by the charge is maximum.

Comparing to experimental result of charge modulation on frequency shift as in Fig.8.11, the overall simulation of flux modulation is closer to experimental data than simulation from charge modulation. A model with more than three bands is needed to acquire higher simulation accuracy for charge modulation.

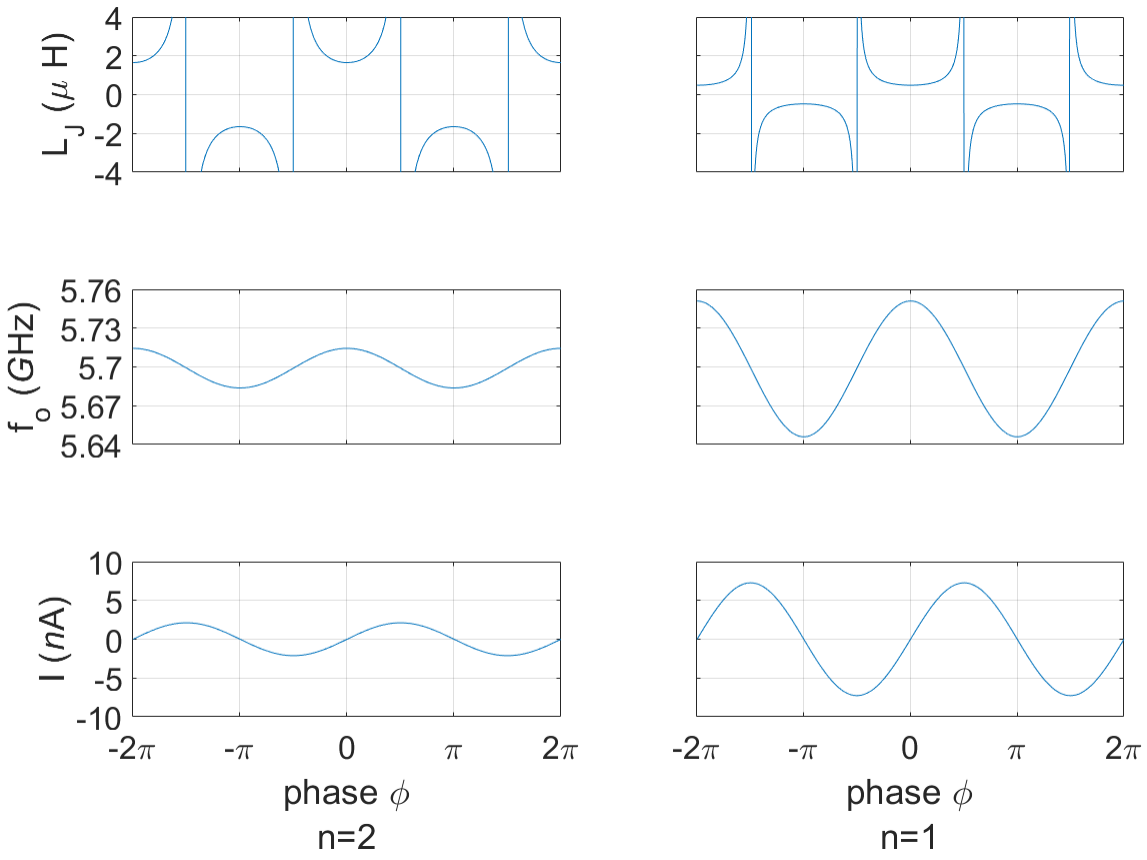

Figure 3.6: Modulation of Josephson inductance L_J, resonant frequency f_o, super current I by the flux bias at two charge states.

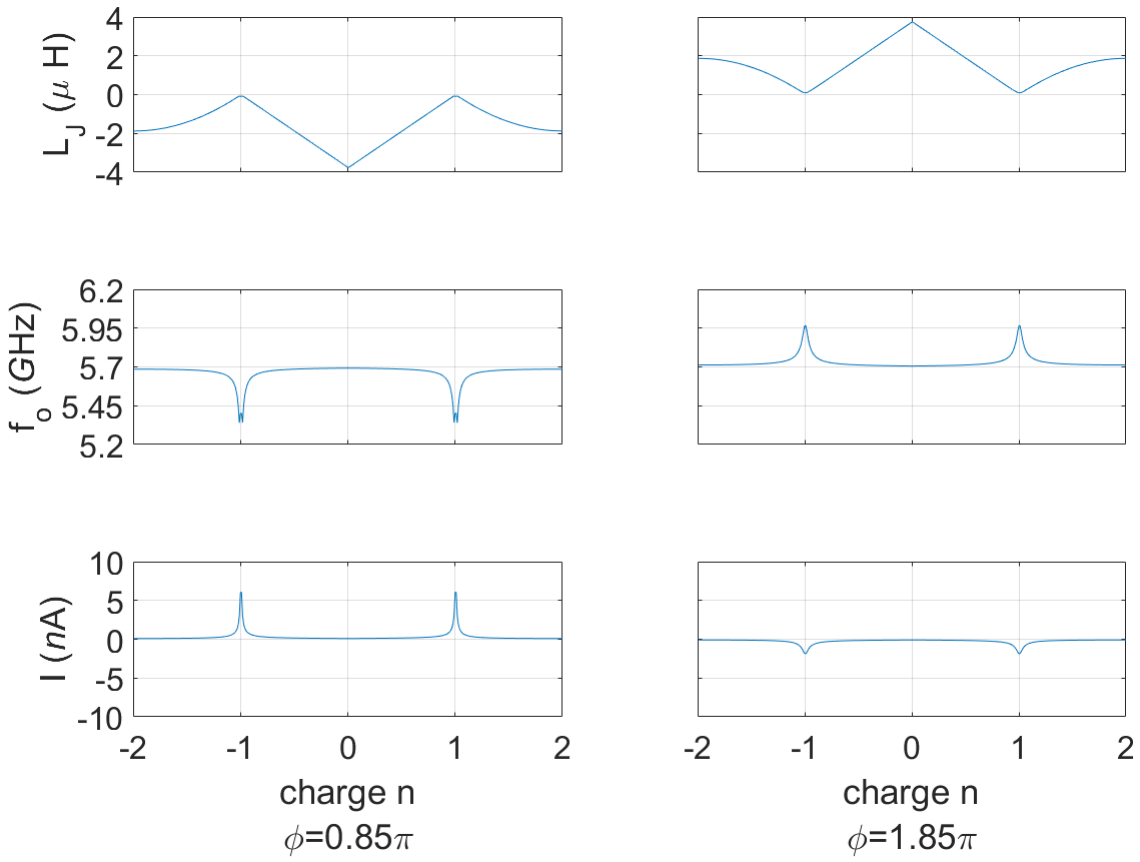

Figure 3.7: Modulation of Josephson inductance (L_J, resoant frequency f_o, super current I) by charge at two flux bias state.

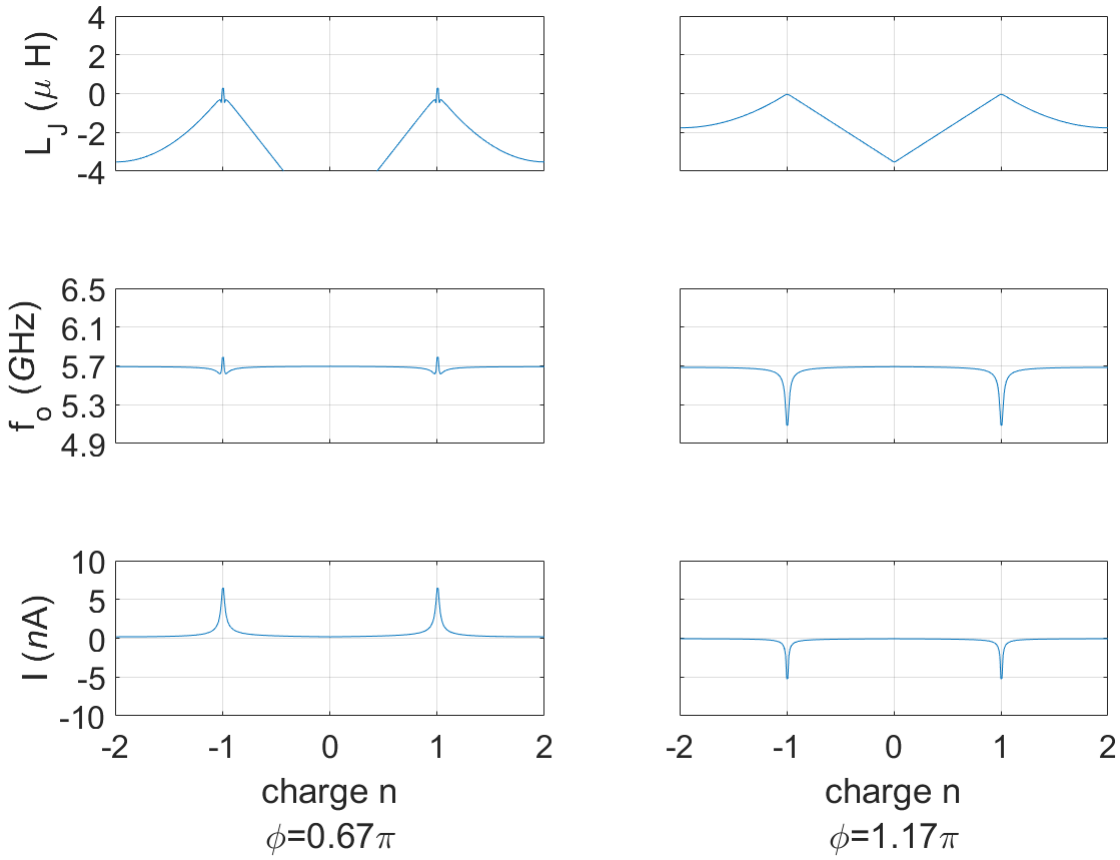

Figure 3.8: Modulation of Josephson inductance L_J, resonant frequency f_o, super current I by charge at two other flux bias states.

Chapter 4

PHOTOLITHOGRAPHY & ELECTRON BEAM LITHOGRAPHY

4.1 PhotoLithography

4.1.1 Design of CPW

Two major design parameters for CPW are the resonant frequency f_o and loaded Q. f_o is determined by the length of the CPW and the relative dielectric constant ϵ_{re} which was calculated with Equation 2.27. Our CPW was designed and simulated using Sonnet software. The simulated resonator gave only a shallow dip at the resonant frequency that is less than 3dB below the off-resonance signal. Due to the shallowness of the resonance the loaded Q factor was measured with an alternative method described in Appendix A.

The flux bias line was designed as a vertical slot to minimize the coupling between the resonator and the flux line as shown in Fig.4.1. If substential coupling is present, the microwave energy in the resonator will couple to the flux line and leaks out, essentially lowering the intrinsic Q of the resonator. The red trace in our design is the SQUID loop

that is used to tune the Josephson inductance E_J. Compared to the usual rectangular shape SQUID loop, the 'L' shaped SQUID loop minimizes the coupling between the resonator and the flux bias line.Also the flux bias line is introduced at the voltage antinode points of the resonator instead of the voltage node. The flux bias line slot has width of 10μm and will unavoidablely interrupt the groud plane of the resonator. At a voltage antinode the slot acts like a capacitor and has smaller perturbative effect. When the slot was moved to the votage node location the ground plane was significantly interrupted and the resonant frequency of the resonator was shifted. This was evaluated with SONNET in the design process.

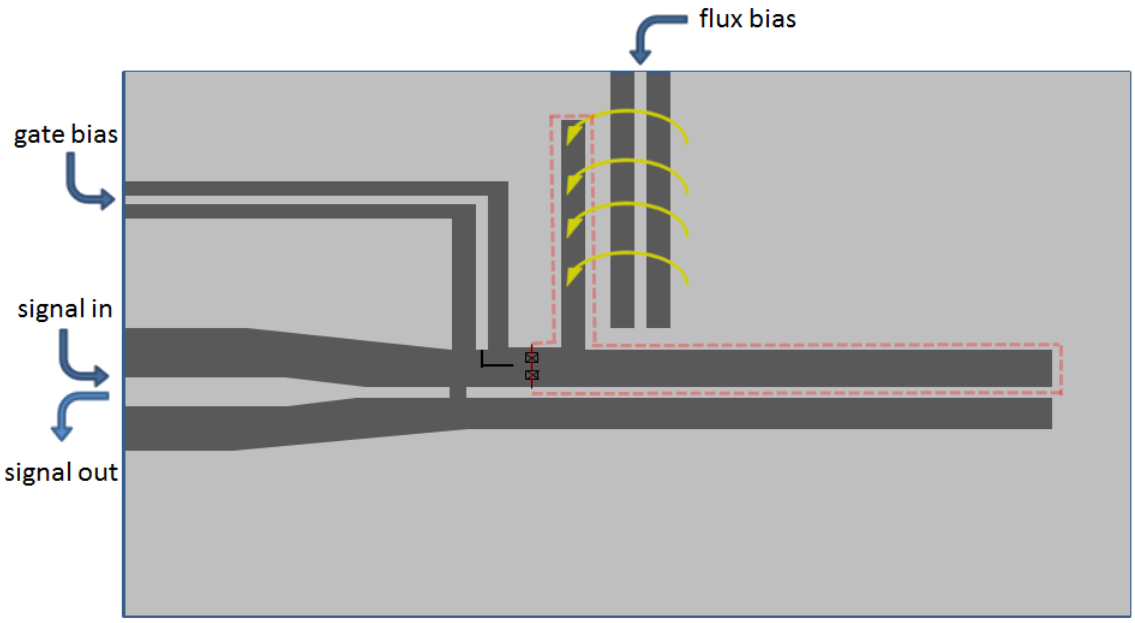

Figure 4.1: Design of the CPW quarter wave resonator with embedded CPT.

The CPW will be in superconducting regime in real measurements. However SONNET did not support simulations with superconducting conductors. We therefore used extremely high electrical conductivity constant for the simulations. The resonant frequency of samples was 300 MHz higher than the simulated value. One explanation was overetch of the silicon substrate during plasma etching of Nb film. It is impossible to stop the plasma etch right at the boundary of Nb film and silicon substrate. Our test procedure showed $\approx 20nm$

over etch on the silicon substrate as discussed in Appendix C.

Finger capacitors as in Fig.4.2 were used to couple the resonator to the measurement circuit for a loaded Q of 5,000 during the simulation, very close to the measured Q for resonators without CPT. However the quality factor degraded to $Q \approx 2000$ after the CPT was introduced. The CPT actually adds additional damping to the resonator which depends on the CPT biasing point. The capacitance could also be retrieved following steps in Appendix A.

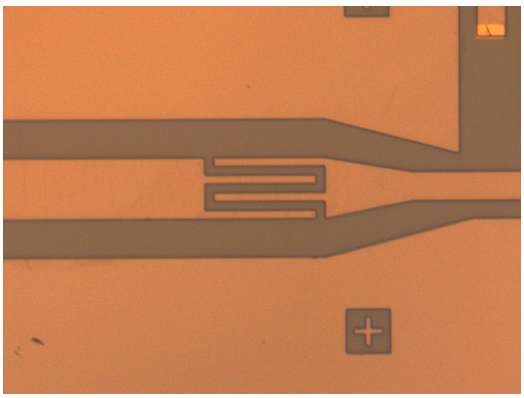

Figure 4.2: the coupling finger capacitor in our resonator which controls the couple coeffcient between the resonator and the external measurement circuit.

4.1.2 Substrate

We used intrinsic high resistivity silicon as the substrate for our sample fabrication, with intrinsic resistivity of $10^4\Omega$/m. For superconducting CPW resonators, the major source for loss of intrinsic Q of the resonator are two level systems (TLS) in the substrate (23).

After the CPW resonator is fabricated, the next step is to shunt the central conductor and the ground plane with the CPT which will be fabricated with Ebeam lithography. Before the CPT is evaporated ion milling could be used to remove the native oxide of the Nb to create a coherent contact. Instead, we opened three windows at the contact area, ion milled the oxidate layer, and deposited 10nm of Au to prevent oxidation on the Nb surface at the window area as shown in Fig.4.8 a.

4.1.3 Fabrication Steps

The silicon wafer was emersed in HF for 10 seconds to remove the surface oxide, then quickly transfered to the sputtering chamber. The ion mill in the sputter chambered was turned on for 15 seconds to remove the leftover surface oxide. Then a $\sim 100nm$ Nb film was deposited onto the whole wafer.

A negative image of the resonator was patterned onto the wafer using a wafer stepper. After development, the wafer was plasma etched to remove undesired parts of the Nb film. Fig.4.3 shows the stepper aligner and the RIE used in the fabrication process.

Figure 4.3: NIKON 8 I-liner Stepper (**a.**) and RIE Unaxis 790 (**b.**) in the clean room of the University of Wisconsin Madison used in the photo lithography process.

We also investigated generating a sloped side wall during the Nb etching to facilitate subsequent Ebeam lithography. The importance of sloped side walls is illustrated in Fig.4.4 a. The Nb film is $\approx 100nm$ thick and the following CPT Al film thickness is $\approx 65nm$. Without sloped side wall the Al film will be discontinuous across the Nb edge and the ground plane. As is shown in Fig.4.4b. With a sloped side wall the Al thin film lies on a solid surface continuously. Procedure for generating the sloped side wall is presented in Appendix C.

After the plasma etch, the wafer was patterned with the stepper aligner again to open

Figure 4.4: Illustration of the effect of having a sloped side wall during Nb etching.

up the windows for the Au contact pads. The Au contact pads were evaporated with an Ebeam evaporater with 15 seconds ion milling at the beginning to remove the oxide layer on the surface of the Nb film.

4.2 Ebeam Lithography

The JJs are characterized by their Josephson Energy E_J and charging energy E_c, For our experiment we are interested in a large resoant frequency shift per charge which is determined by both E_c and E_J as shown in Fig.3.7 and 3.8. For fixed E_J larger E_c or smaller junction area will produce higher frequency shift. E_J defines the Josephson inductance L_J and hence the overall freqeuncy shift by charge. Ebeam lithography is ideal for this purpose. I have successfully fabricated $30nm$ size JJs with our Ebeam facility here at Dartmouth. However, very small junction sizes are susceptible to oxidation at room temperature, which will change the Josephson Energy E_J. Past experience has shown that the junction will acquire an extra $1k\Omega$ resistance for every 15 hours at room temperature or pressure. Junction size of $50nm^2$ is a plausible solution as it balances the charge sensivity requirement and vulneriability to room temperature oxidation.

The technicque for making the small junctions is the Dolan bridge (10) method or shadow evaporation. It relies on two Ebeam resist layers to cast a shadow during film deposition. An alternative method for fabricating junctions is presented in Appendix D. Fig. 4.5 illustrations the principle of shadow evaporation. The design pattern is transfered to both

Copolymer and PMMA electron beam resist layers, Due to different sensitivity to electrons, the pattern in the copolymer layer will be 'fatter' than the one in the PMMA layer due to the difference in sensitivity to electrons. The pattern in the PMMA layer works as an aperture and will shift the location of the thin films when deposited at different angles. A junction will be generated as an overlap from the patterns of the two evaporations. The size of the junction can be controlled by the difference in the successive evaoration angles and the size of the top layer pattern. Larger difference will create smaller overlap and smaller junction area consequently

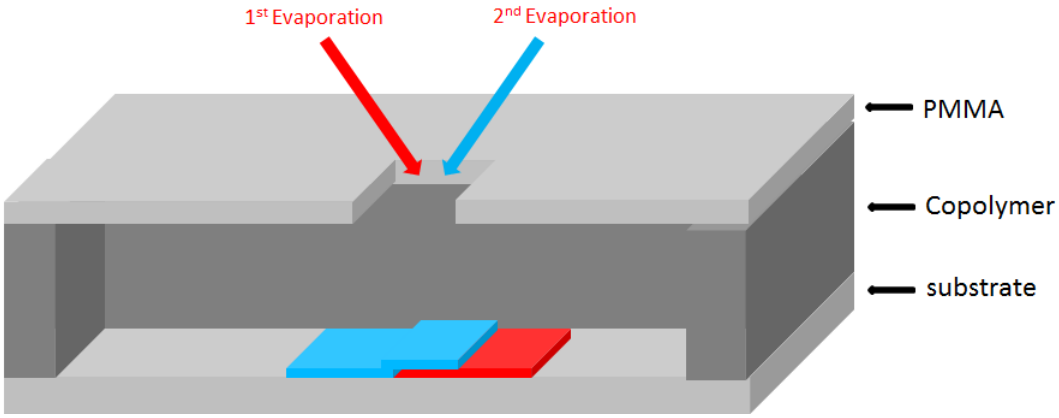

Figure 4.5: Illustration of the principle of shadown evaporation.

4.3 Plasma Cleaning

Before e-beam resist spinning the sample is plasma cleaned for 1 minutes to remove residual photoresist on the surface. A better idea would be to plasma clean the sample right after photolithography, and only shorter plasma time is needed. The leftover resist would harden as time goes on so longer plasma cleaning is required for older residual resist. Oxygen plasma only attacks resist and will leave metal untouched (41; 40).

After plasma cleaning a layer of copolymer is spin coated onto the substrate with thickness $\approx 350n$m. Then a layer of PMMA 950 A4 is spin coated with thickness $\approx 200n$m on top of

the copolymer. The substrate was placed in an SEM (scanning electron microscope). The NPGS (Nanometer Pattern Generetion System) (26) system was used to expose certain areas of the resist layers to electrons based on the pattern saved in the beam position control computer. After development the design pattern is tranfered to the e-beam resist layers. The pattern in the copolymer layer will be a 'fatter' version of the one in the PMMA layer.

A dose array is carried out as the first step to calibrate the electron exposure. The right amount of electron dose will yield a geometry with the desired size. JJs are the smallest structure and also the most critical ones during lithography. Due to their miniature size, we use the highest magnification (×8000 for our sample) that is applicable for consistent junction production. However, a lower magnification is used when drawing the leads that create contacts to the JJs. Switching magnification was also acompanied by a shift of the focus center of the electron beam. During dose array test we often calibrate the offset of that also and compensate it by moving the center of the pattern in the design file.

E-beam lithography fabrication of the sample for this project was generated at the CNS (Center for Nanoscale Systems) of Harvard University with a SEM JEOL JSM-7000F as shown in Fig. 4.6. After Ebeam pattern generation the substrate was plasma cleaned for 20 seconds to remove leftover Ebeam resist. Appendix **??** gives the procedures for plasma cleaning.

The island of the CPT has a thickness of only 9 *n*m. CPT with thinner island is less liable to trap quasi particles but more difficult to fabricate because Al tends to cluster together. (9) When the film is thin, the island will naturally be a layer of Al clusters instead of uniform film. But if the island is evaporated at a much lower temperature, the Al atoms will have much less kinetic energy to migrate on the substrate and a uniform thin film will be generated. Fig.4.7 (a) shows the thermal evaporator in our lab that has been used for JJ fabrication, and Fig. 4.7(b) shows the apparatus for deposition angle adjustment. Part

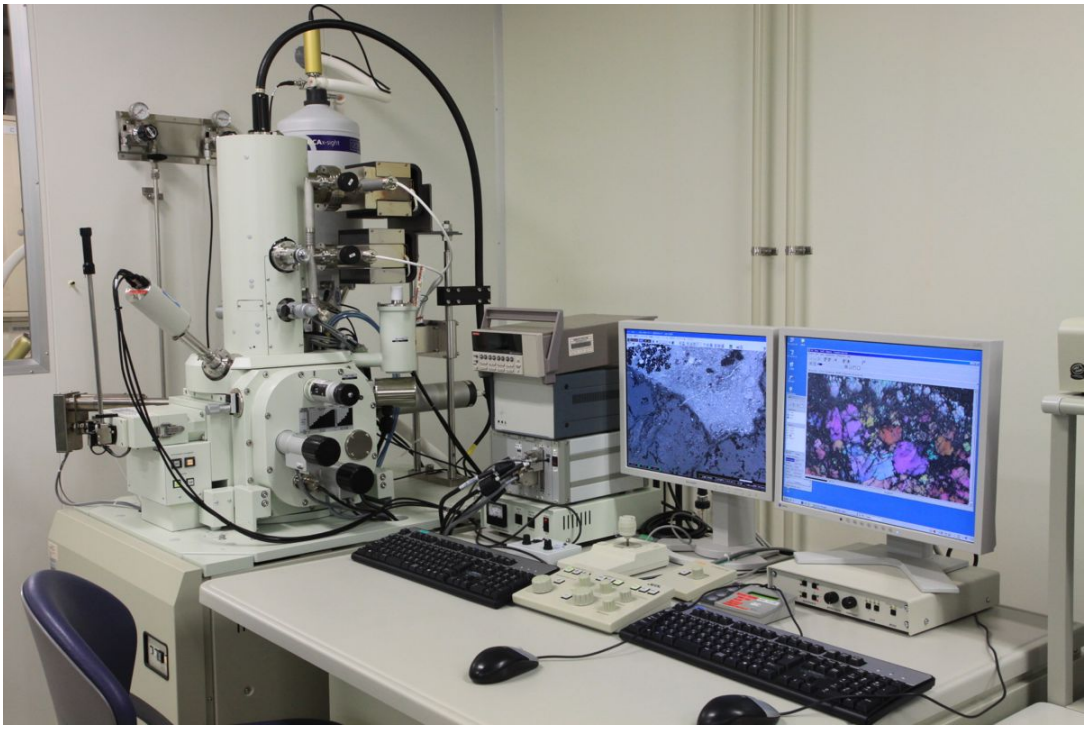

Figure 4.6: SEM JEOL JSM-7000F equiped with NPGS system for Ebeam lithography

(I) moves up and down by twisting the threaded rod changing the height of part (II), and hence adjusting the tilting angle of the sample. Fig.4.7(c) shows how the sample holder is chilled to LN_2 temperature.

Fig. 4.8 shows SEM images of our CPT embedded in a CPT resonator. Fig. 4.8(a) is an overall image of a CPT inside a CPW resonator. The three bright rectangles are gold contact pads, and the bright circle is a focus mark generated by bombarding the sample surface with the electron beam for 39 seconds. Fig. 4.8(b) is a zoom in of the red rectangle in (a). The left lead is the gate of the CPT, the upper and lower pieces the right are the source and drain of CPT. Fig. 4.8(c) is a zoom-in of the red rectangle in (b) and (d) is a zoom-in of the red rectangle in (c). The CPT has a junction size of $\approx 50\times50\,n\text{m}^2$ and island thickness of only 9 nm.

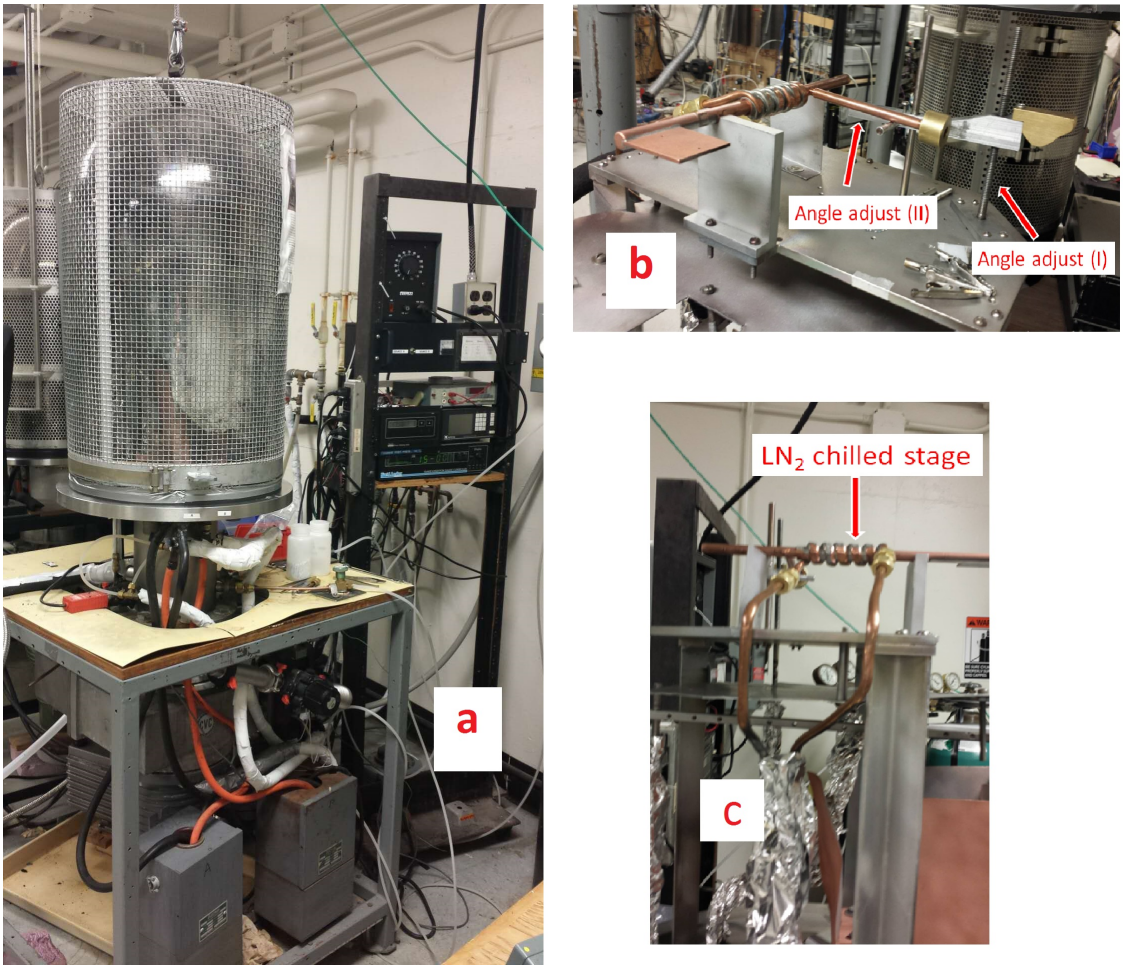

Figure 4.7: Thermal evaporator used to deposit thin Al films for JJ fabrication.

4.4 Printed Circuit Boards and Sample Holders

The printed circuit board (PCB) (see Fig.4.9(a)) holds the sample substrate and works as an adaptor between the sample and the measurement lines. The lines are designed to have 50Ω resistance for proper impedance matching. The ground planes of the top and bottom are connected through the vias (0.014" diameter 0.04" apart) to suppress parasitic modes. The sample ground plane was wire bonded with the PCB with as many bond wires as possible. The three parts of the chip ground planes are wire-bonded together also to ensure a uniform ground plane. The sample chip fits snugly into the PCB to minimize the bonding wire length.

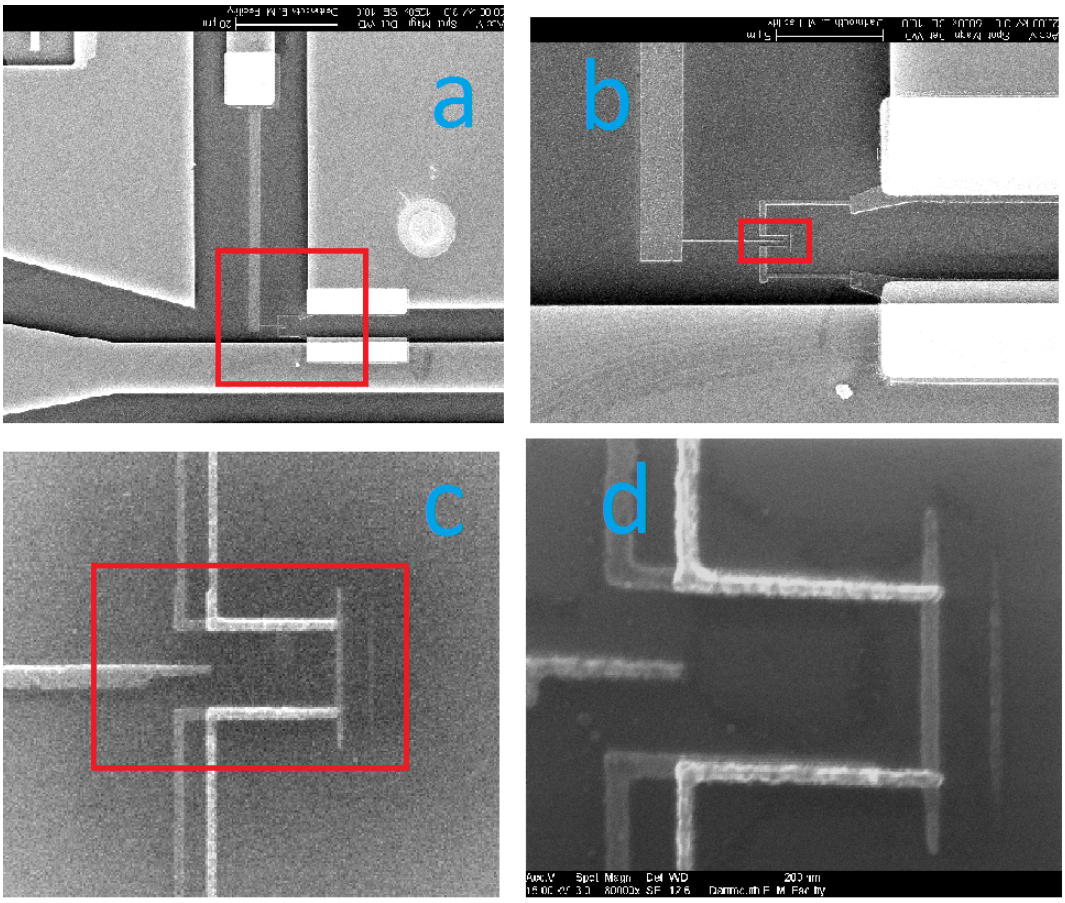

Figure 4.8: SEM images of the CPT imbedded in the CPW.

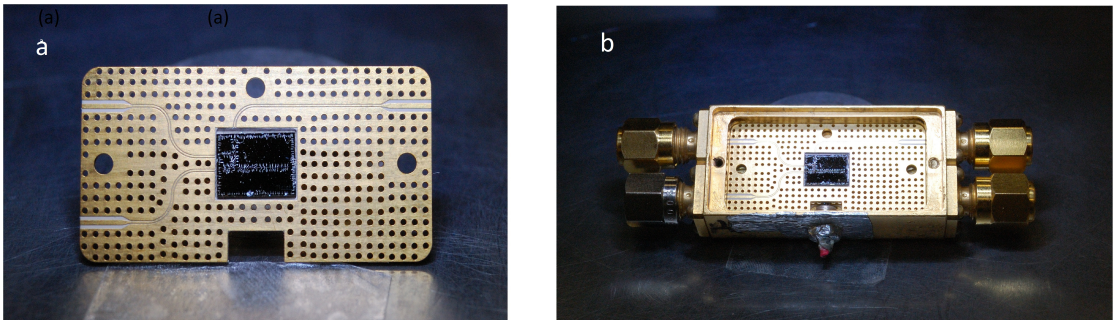

Figure 4.9: PCB and holders provide connection to the sample with minimum introduction of noise.

The PCB was placed in the sample holder that provides connection to the measurement lines as shown in the right figure of Fig. 4.9. It was gold-plated to protect against tarnishing and enable reliable thermal contacts and wire bonding. Nickel plating was omitted to avoid magnetic degradation of the superconducting films. The internal surface of the box was coated with microwave absorbent materials to minimize the number of microwave

and infrared photon present.

Chapter 5

JOSEPHSON PARAMETRIC AMPLIFIER

This chapter shows the theoretical calculations for the Josephson parametric pumping that exists intrinsically in our charge detector. All the calculation steps are carried out based on the measurement setup in our system. It gives a direct picture of the nonlinearity in our resonator and offers theoretical foundations for the principles governing the effects we have observed during our measurement. The major symbols used are:

γ (t): Josephson junction (JJ) phase,

Φ(x,t) : cavity phase density

C_c: coupling capacitor.

Fig.5.1 is a schematic of our CPW resonator embedded with a CPT. In the following the two junctions are treated as a single junction to simplify the calculations. The gate modulation will bring in at the end through the current relation in a SQUID loop as in Chapter 6.

Away from the junction and the resonator port the microwave field obeys standard wave

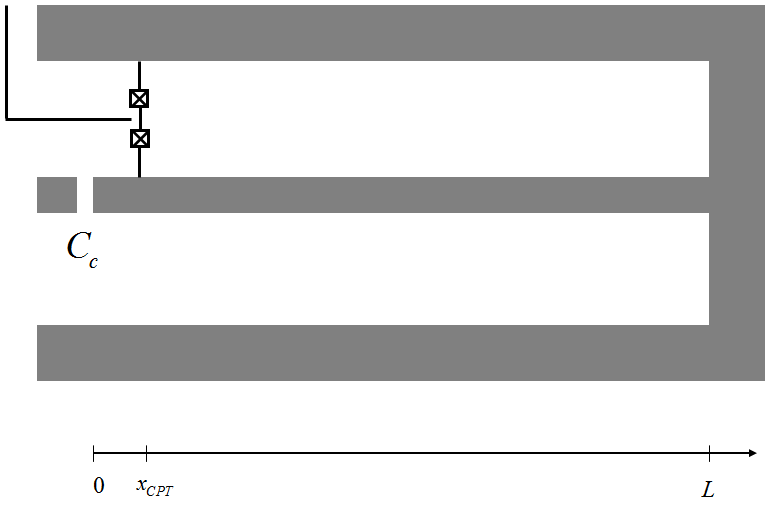

Figure 5.1: A JJ embedded in a quarter wavelength CPW

equation

$$\ddot{\Phi}(x,t) = v^2 \partial_{xx} \Phi(x,t) \tag{5.1}$$

with $v^2 = 1/L_o C_o$, and L_0, C_o the unit inductance and capacitance of the cavity. We use a multimode expansion

$$\Phi(x,t) = \sum_m \phi_m(t)\mu_m(x) \tag{5.2}$$

and applying the following boundary conditions: (ble)

$$\frac{\Phi_o}{2\pi}\left(\ddot{\Phi}(0,t) - \frac{1}{C_c L_o}\partial_x \Phi(x,t)|_{x=0}\right) = \dot{V}_i \tag{5.3}$$

$$\frac{\Phi_o}{2\pi}\dot{\Phi}(L,t) = 0 \text{ or } \mu_m(L) = 0 \tag{5.4}$$

$$\frac{\Phi_o}{2\pi}\left(\frac{1}{L_o}\partial_x \Phi(x,t)|_{x=x_j+} - \frac{1}{L_o}\partial_x \Phi(x,t)|_{x=x_j-}\right) = I_c \sin(\gamma) + \frac{\hbar C_J}{2e}\ddot{\gamma} \tag{5.5}$$

$$\int^t \frac{\hbar}{2e}\frac{d\gamma}{dt}dt = \frac{\Phi_o}{2\pi}\Phi(x_j,t) \tag{5.6}$$

The constraints can be satisfied by choosing

$$\mu_m(x) = A_m \begin{cases} \cos[k_m x + \psi_m^l] & \text{for} \quad 0 \le x \le x_{cpt} \\ B_m \sin[k_m(L - x_j) + \psi_m^r] & \text{for} \quad x_{cpt} \le x \le L \end{cases} \tag{5.7}$$

The normalization constants A_m, relative amplitudes B_m, phases ψ_m^l, ψ_m^r and wave vector k_m are to be specificed.

Substitute the wave equation 5.1 into BCs (5.3)

$$\frac{\Phi_o}{2\pi}\left(\frac{1}{L_o C_o}\partial_{xx}\Phi(x,t)|_{x=0} - \frac{1}{C_c L_o}\partial_x \Phi(x,t)|_{x=0}\right) = \dot{V}_i \tag{5.8}$$

For homogeneous BCs

$$\frac{1}{L_o C_o}\partial_{xx}\Phi(x,t)|_{x=0} - \frac{1}{C_c L_o}\partial_x \Phi(x,t)|_{x=0} = 0 \tag{5.9}$$

or

$$\partial_x \mu_m|_{x=0} - \frac{C_c}{C_o}\partial_{xx}\mu_m|_{x=0} = 0 \tag{5.10}$$

As $C_c/C_o L \ll 1, C_c/C_o \ll 1$

According to Taylor expansion

$$\partial_x \mu_m|_{x=0-\frac{C_c}{C_o}} = \partial_x \mu_m|_{x=0} - \frac{C_c}{C_o}\partial_{xx}\mu_m|_{x=0} + \cdots \tag{5.11}$$

Equation (5.10) change to a shifted BC

$$\partial_x \mu_m|_{x=0-\frac{C_c}{C_o}} = 0 \tag{5.12}$$

And equivalently

$$\psi_m^l = \frac{C_c}{C_o} \tag{5.13}$$

By BC (5.4)

$$\psi_m^r = 0 \tag{5.14}$$

Substitute equation (5.13), (5.14) into equation (5.7)

$$\mu_m(x) = A_m \begin{cases} \cos[k_m(x + \frac{C_c}{C_o})] & \text{for} \quad 0 \le x \le X_j \\ B_m \sin[k_m(L - x)] & \text{for} \quad X_j \le x \le L \end{cases} \tag{5.15}$$

The center conductor is connected at the JJ point so at $x = x_j$ the flux should be equal and this determines the B_m

$$B_m = \frac{\cos[k_m(x_j + \frac{C_c}{C_o})]}{\sin[k_m(L - x_j)]} \tag{5.16}$$

Substitute equation (5.16) into equation (5.15)

$$\mu_m(x) = A_m \begin{cases} \cos[k_m(x + \frac{C_c}{C_o})] & \text{for} \quad 0 \le x \le X_j \\ \frac{\cos[k(X_j + C_c/C_o)]}{\sin[k_m(L - X_j)]} \sin[k_m(L - x)] & \text{for} \quad X_j \le x \le L \end{cases} \tag{5.17}$$

Lagrangian flux density reads

$$\mathscr{L} = \frac{C_0(x)\dot{\psi}^2(x,t)}{2} - \frac{1}{2L_0(x)}\left(\frac{\partial\psi(x,t)}{\partial x}\right)^2 \tag{5.18}$$

with $\psi(x,t) = \int_{-\infty}^{t} dt' V(x,t')$ is the flux density, $C_0(x)$ the position dependent capacitance per unit length and $L_0(x)$ the position-dependent inductance per unit length.

Or expressing with cavity phase density

$$\mathscr{L} = \left(\frac{\Phi_o}{2\pi}\right)^2 \frac{C_0(x)\dot{\psi}^2(x,t)}{2} - \frac{1}{2L_0(x)}\left(\frac{\partial\psi(x,t)}{\partial x}\right)^2 \left(\frac{\Phi_o}{2\pi}\right)^2 \tag{5.19}$$

The corresponding Euler-Lagrange equation of motion

$$\frac{d}{dx}\left[\frac{1}{L_0(x)}\frac{\partial\Phi(x,t)}{\partial x}\right] = C_0(x)\ddot{\Phi}(x,t) \tag{5.20}$$

Substitute Eq.5.2 in and we arrive at a Sturm-Liouville differential equation of the form

$$\frac{d}{dx}\left[\frac{1}{L_0(x)}\frac{\partial\mu(x)}{\partial x}\right] = \omega^2 C_0(x)\mu(x) \tag{5.21}$$

and the eigen modes are defined as

$$\int_0^L C_0(x)\mu_n(x)\mu_m(x)dx = \tilde{C}_T\delta_{nm} \tag{5.22}$$

and $\tilde{C}_T = C_{TL} + \mu_m(x_j)C_J$ as C_J is in parallel connection with C_o

The capacitive participation ratio defined as $\eta_{c,m} = \mu_m(x_j)C_J/\tilde{C}_T$

Taking the partial derivative of Eq. (5.21) with respect to x

$$\frac{d^2}{dx^2}\left[\frac{1}{L_0(x)}\frac{\partial\mu(x)}{\partial x}\right] = \omega^2 C_0(x)\frac{d\mu(x)}{dx} \tag{5.23}$$

$$= \frac{1}{L_0}\frac{d\mu(x)}{dx} \tag{5.24}$$

Here C_o has been taken as constant since C_J is in parallel with C_{TL} and $C_J \ll C_{TL}$.

Eq. (5.24) defines a second Sturm-Liouville type problem with eigen value 1 and weight function $1/L_o$. The eigen modes obey

$$\int_0^L \frac{1}{L_0}(x)\frac{d\mu_n(x)}{dx}\frac{d\mu_m(x)}{dx}dx = \frac{\delta_{nm}}{\tilde{L}_T} \tag{5.25}$$

And

$$\frac{1}{\tilde{L}_{T,m}} = \int_0^{x_J} \frac{1}{L_o}\left(\frac{d\mu_m(x)}{dx}\right)^2 dx + \int_{x_J}^{L} \frac{1}{L_o}\left(\frac{d\mu_m(x)}{dx}\right)^2 dx + \frac{1}{L_J}\left(\mu_m(x_J)\right)^2 \quad (5.26)$$

$$= \int_0^{L} \frac{1}{L_o}\left(\frac{d\mu_m(x)}{dx}\right)^2 dx + \frac{1}{L_J}\left(\mu_m(x_J)\right)^2 \quad (5.27)$$

The flux difference across L_o is $d\mu_m(x)$, but it is $\mu_m(x)$ for L_J since the JJ is connected to the ground directly. The flux across it is just $\mu_m(x)$. The inductive participation ratio defined as $\eta_{l,m} = (\mu_m^2(x_j)\tilde{L}_T)/L_J$

By Eq. (5.22), the normalization constant A_m is set by the equation

$$\langle \mu_m \cdot \mu_m \rangle \equiv A_m^2 \int_0^{X_j} C_0 dx \cos^2[k_m(x + \frac{C_c}{C_o})] \quad (5.28)$$

$$+ A_m^2 \frac{\cos^2[k(X_j + C_c/C_o)]}{\sin^2[k_m(L - X_j)]} \int_{X_j}^{L} C_0 dx \sin^2[k_m(L-x)] + A_m^2 C_J \cos^2[k_m(X_j + \frac{C_c}{C_o})] \quad (5.29)$$

$$= C_T \delta_{mn} \quad (5.30)$$

and calculated as

$$A_m^2 C_0 \left\{\frac{1}{2}x_j + \frac{1}{4k_m}[\sin(2k_m(x_j + \frac{C_c}{C_o})) - \sin(2k_m\frac{C_c}{C_o})]\right\} + \quad (5.31)$$

$$A_m^2 C_0 \frac{\cos^2[k_m(x_j + \frac{C_c}{C_o})]}{\sin^2[k_m(L - x_j)]} \left\{[\frac{1}{2}(L - x_j) - \frac{1}{4k_m}\sin(2k_m(L - x_j))]\right\} + \quad (5.32)$$

$$A_m^2 C_J \frac{\cos^2[k_m(x_j + \frac{C_c}{C_o})]}{\sin^2[k_m(L - x_j)]} \cos^2[k_m(X_j + \frac{C_c}{C_o})] = C_T \quad (5.33)$$

with $C_T = C_{TL} + C_J$

The eigen modes λ_n and eigen frequency ω_n of the cavity are:

$$\lambda_n = \frac{4Ł}{2n-1} \tag{5.34}$$

$$\omega_n = 2\pi\frac{\nu}{\lambda_n} \tag{5.35}$$

$$= 2\pi\nu\frac{2n-1}{4Ł} \tag{5.36}$$

$$= (n-\frac{1}{2})\pi\nu \tag{5.37}$$

with n=1, 2, 3, $\cdots$

Check the orthogonality of the fundamental mode with higher order modes of the cavity.

$$\omega_1 = \frac{\pi\nu}{2\mathrm{L}} \tag{5.38}$$

$$\omega_m = (m-\frac{1}{2})\frac{\pi\nu}{\mathrm{L}} \tag{5.39}$$

For $m = 2,3,4,\cdots$

$$\int_0^{\frac{4L}{\nu}} \sin(\omega_1 t)\sin(\omega_m t)dt = \frac{1}{2}\left(\int_0^{\frac{4L}{\nu}} \cos[(\omega_1-\omega_m)t]dt - \int_0^{\frac{4L}{\nu}} \cos[(\omega_1+\omega_m)t]dt\right) \tag{5.40}$$

$$= \frac{1}{2(\omega_1-\omega_m)}\sin[(\omega_1-\omega_m)t]|_0^{\frac{4L}{\nu}} - \frac{1}{2(\omega_1+\omega_m)}\sin[(\omega_1+\omega_m)t]|_0^{\frac{4L}{\nu}} \tag{5.41}$$

$$= \frac{1}{2(\omega_1-\omega_m)}\sin[(\frac{3}{2}-m)4\pi] - \frac{1}{2(\omega_1+\omega_m)}\sin[(\frac{1}{2}+m)4\pi] \tag{5.42}$$

$$= 0 \tag{5.43}$$

The fundamental mode ω_1 is orthogonal with all the higher order mode ω_m. The normal-

ization constant for the fundamental mode is

$$N_1 = \int_0^{\frac{4L}{v}} \sin(\omega_1 t)\sin(\omega_1 t)\,dt = \frac{1}{2}\int_0^{\frac{4L}{v}} [1-\cos(2\omega_1 t)]\,dt \tag{5.44}$$

$$= \frac{2L}{v} - \frac{1}{2}\int_0^{\frac{4L}{v}} \cos(2\omega_1 t)\,dt \tag{5.45}$$

$$= \frac{2L}{v} - \frac{1}{4\omega_1}\sin(2\omega_1 t)|_0^{\frac{4L}{v}} \tag{5.46}$$

$$= \frac{2L}{v} \tag{5.47}$$

By wave equation (5.1) the time dependent part of the wave satisfies

$$\phi_m(t) = \sin(k_m v t) \tag{5.48}$$

Substitute equation (5.17) into BC (5.5)

$$\frac{A_m \sin(k_m v t)\Phi_o}{2\pi L_o}\left\{k_m \frac{\cos[k_m(X_j + C_c/C_o)]}{\sin[k_m(L-X_j)]}\cos[k_m(L-X_j)] - k_m \sin[k_m(X_j + \frac{C_c}{C_o})]\right\}$$

$$= I_c \sin(\gamma) + \frac{\hbar C_J}{2e}\ddot{\gamma} \tag{5.49}$$

$$\frac{A_m \sin(k_m v t)\Phi_o}{2\pi L_o \sin[k_m(L-X_j)]}$$

$$\left\{k_m \cos[k_m(X_j + C_c/C_o)]\cos[k_m(L-X_j)] - k_m \sin[k_m(X_j + \frac{C_c}{C_o})]\sin[k_m(L-X_j)]\right\} \tag{5.50}$$

$$= I_c \sin(\gamma) + \frac{\hbar C_J}{2e}\ddot{\gamma} \tag{5.51}$$

$$\frac{A_m \sin(k_m v t)\Phi_o}{2\pi L_o \sin[k_m(L-X_j)]}\left\{k_m \cos[k_m(X_j + C_c/C_o) + k_m(L-X_j)]\right\} = I_c \sin(\gamma) + \frac{\hbar C_J}{2e}\ddot{\gamma} \tag{5.52}$$

$$\frac{A_m \sin(k_m v t)\Phi_o k_m}{2\pi L_o \sin[k_m(L-X_j)]}\{\cos[k_m(L + C_c/C_o)]\} = I_c \sin(\gamma) + \frac{\hbar C_J}{2e}\ddot{\gamma} \tag{5.53}$$

By BC (5.6)

$$\frac{\hbar}{2e}\gamma = \frac{\Phi_o}{2\pi}\Phi(x_j,t) \tag{5.54}$$

$$\gamma = \Phi(x_j,t) \tag{5.55}$$

Substitute into equation (5.53)

$$\frac{A_m \sin(k_m v t)\Phi_o k_m}{2\pi L_o \sin[k_m(L-X_j)]}\{\cos[k_m(L+C_c/C_o)]\} = I_c \sin\left(A_m \sin(k_m v t)\cos[k_m(x_j+\frac{C_c}{C_o})]\right) - \frac{\hbar C_J (k_m v)^2}{2e} A_m \sin(k_m v t)\cos[k_m(x_j+\frac{C_c}{C_o})] \tag{5.56}$$

Using the Bessel function relations

$$\sin(X\sin\theta) = \sum_{n=-\infty}^{\infty} J_n(X)\sin(n\theta) \tag{5.57}$$

where J_n is an nth order Bessel function of the first kind.

$\sin\left(A_m \sin(k_m v t)\cos[k_m(x_j+\frac{C_c}{C_o})]\right)$ can be written into $\sum_{n=-\infty}^{\infty} J_n\left(A_m\cos[k_m(x_j+\frac{C_c}{C_o})]\right)\sin(nk_m v t)$

equation (5.56) change to

$$\frac{A_m \sin(k_m v t)\Phi_o k_m}{2\pi L_o \sin[k_m(L-X_j)]}\{\cos[k_m(L+C_c/C_o)]\} = I_c \sum_{n=-\infty}^{\infty} \sin(nk_m v t) J_n\left(A_m\cos[k_m(x_j+\frac{C_c}{C_o})]\right) - \frac{\hbar C_J (k_m v)^2}{2e} A_m \sin(k_m v t)\cos[k_m(x_j+\frac{C_c}{C_o})] \tag{5.58}$$

To calculate the fundamental mode k_1, multiply by $\sin(k_1 v t)$ on both sides of equation

(5.58) and integrate t over one period

$$\begin{aligned}
&\frac{A_1\int_0^{\frac{4L}{v}}\sin(k_1vt)\sin(k_1vt)dt\Phi_o k_1}{2\pi L_o\sin[k_1(L-X_j)]}\{\cos[k_1(L+C_c/C_o)]\}= \\
&I_c\sum_{n=-\infty}^{\infty}\int_0^{\frac{4L}{v}}\sin(k_1vt)\sin(nk_1vt)dtJ_n\left(A_1\cos[k_1(x_j+\frac{C_c}{C_o})]\right)- \\
&\frac{\hbar C_J(k_1v)^2}{2e}A_1\int_0^{\frac{4L}{v}}\sin(k_1vt)\sin(k_1vt)dt\cos[k_1(x_j+\frac{C_c}{C_o})]
\end{aligned} \tag{5.59}$$

Using the orthogonal and normal condition of (5.43) and (5.47), above equation simplifies to

$$\begin{aligned}
&\frac{A_1\Phi_o k_1}{2\pi L_o\sin[k_1(L-X_j)]}\{\cos[k_1(L+C_c/C_o)]\}= \\
&I_c\left(J_1(A_1\cos[k_1(x_j+\frac{C_c}{C_o})])-J_{-1}(A_1\cos[k_1(x_j+\frac{C_c}{C_o})])\right)- \\
&\frac{\hbar C_J(k_1v)^2}{2e}A_1\cos[k_1(x_j+\frac{C_c}{C_o})]
\end{aligned} \tag{5.60}$$

With the relationship $E_J=\Phi_o I_c/2\pi$, equation (5.58) changes to

$$\begin{aligned}
&\frac{A_1\Phi_o k_1}{2\pi L_o\sin[k_1(L-X_j)]}\{\cos[k_1(L+C_c/C_o)]\}= \\
&\frac{2\pi E_J}{\Phi_o}\left(J_1(A_1\cos[k_1(x_j+\frac{C_c}{C_o})])-J_{-1}(A_1\cos[k_1(x_j+\frac{C_c}{C_o})])\right)- \\
&\frac{\hbar C_J(k_1v)^2}{2e}A_1\cos[k_1(x_j+\frac{C_c}{C_o})]
\end{aligned} \tag{5.61}$$

C_c is calculated with equation in reference (12) based on the Q_i and Q_L from our measurement result.

k_1 as a function of the JJ location in the cavity x_j can be solved numerically by finding the intersection point of the LHS and RHS of above equation. Figure (5.2) shows the wave vector k_1 and the wave amplitude with JJ at two locations for $E_J/E_C=0.15$. The upper figure is the JJ on the voltage antinode of the resonator. It has minimum interruption on the wave vector and wave energy in the resonator. The lower figure is the JJ 1/10 to the

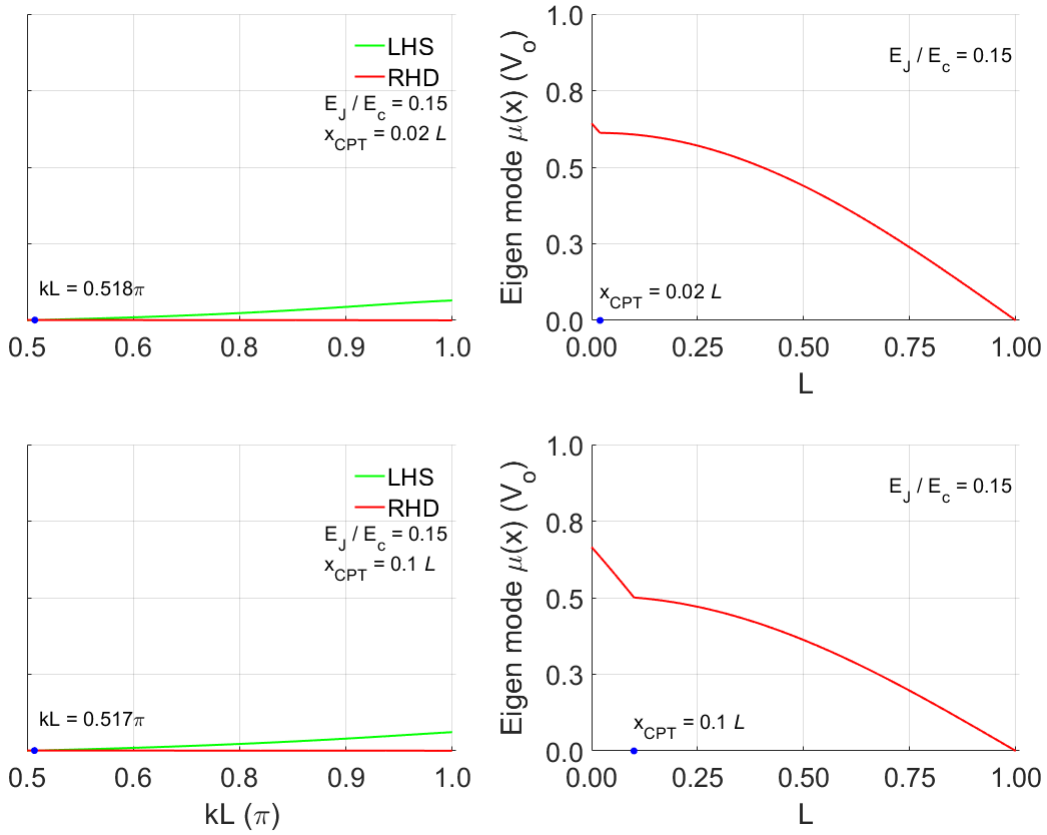

Figure 5.2: wave vector k_1 and amplitude at two JJ locations for $E_J/E_C = 0.15$

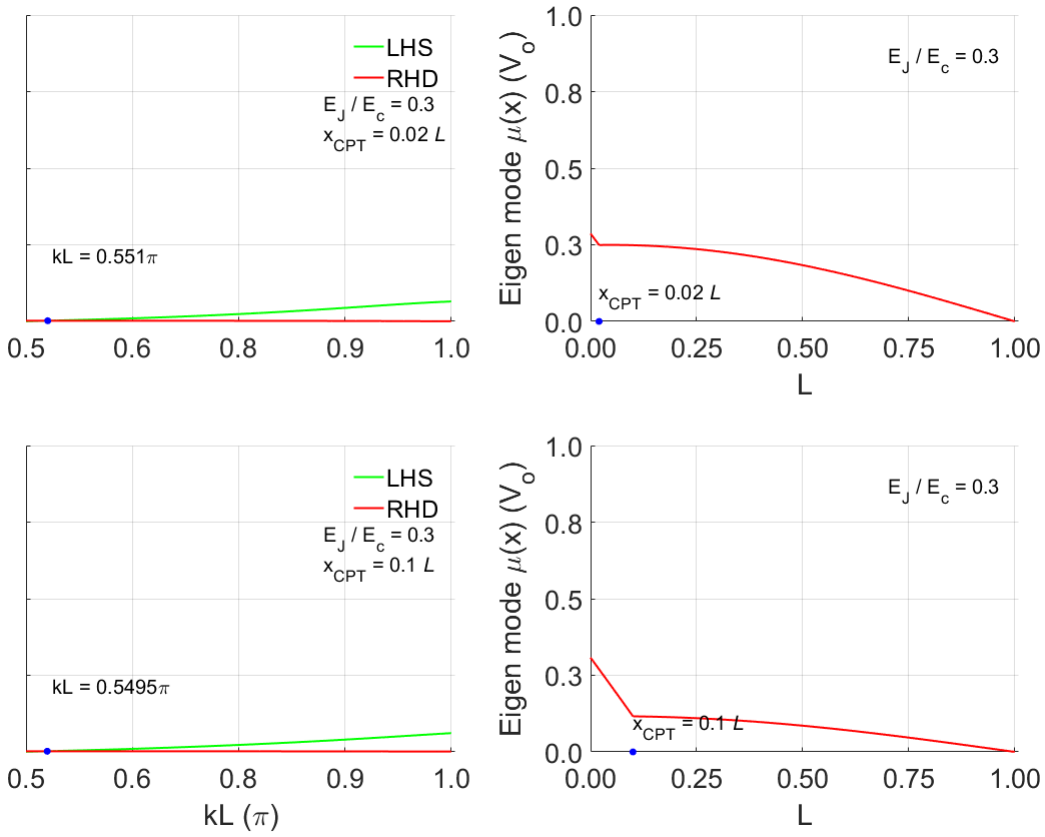

Figure 5.3: wave vector k_1 and amplitude at two JJ locations for $E_J/E_C = 0.30$

right of the voltage antinode, it has a larger perturbation on the wave vector and energy of the resonator.

When the E_J/E_C ratio is higher, Josephson inductance L_J is smaller and the nonlinearity of the resonator will be stronger. Figure (5.3) is similar plot of Figure (5.2) with $E_J/E_C = 0.30$. The difference on the wave vector k_1 and amplitude for the two locations are larger. Comparing these two figures we can see that the nonlinearity of the resonator will increase the JJ further away from the voltage antinode and larger E_J/E_C ratio, which is a result of stronger participation of L_J in the total system. Fig.5.4 shows the calculated wavevector as function of Josephson energy E_j and location of x_{cpt}.

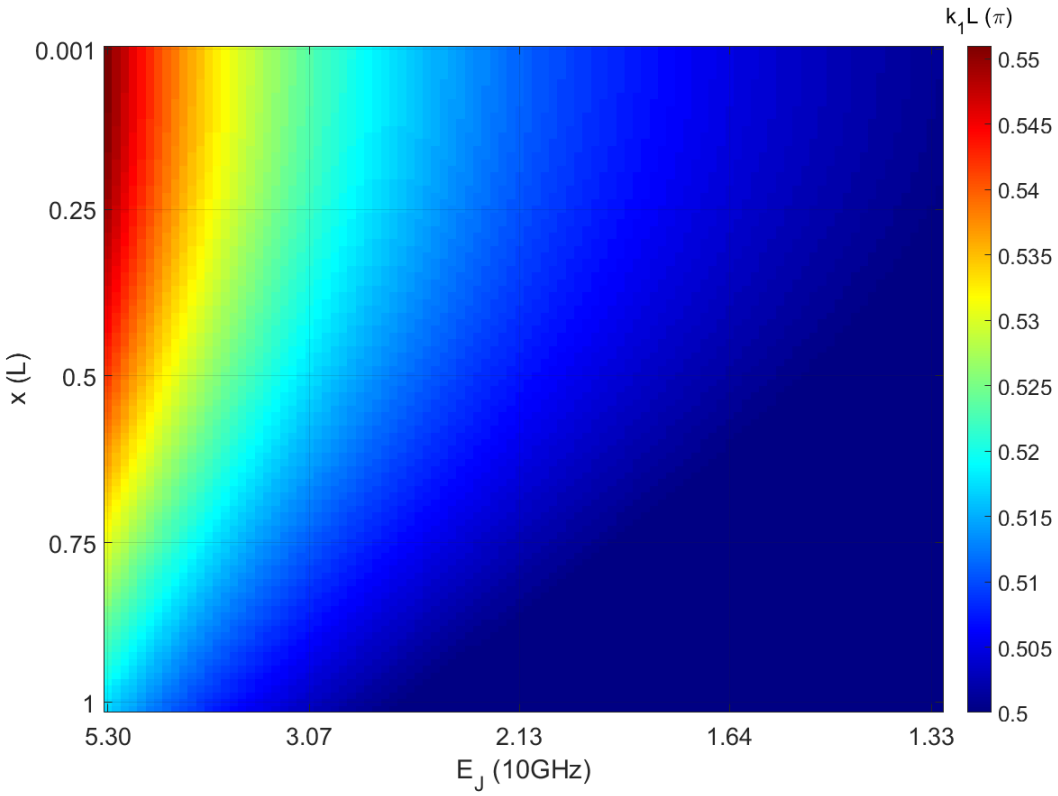

Figure 5.4: wave vector k_1 as function of E_J and insertion location x_{cpt}

The system Hamiltonian is calculated as:

$$H = (\frac{\Phi_o}{2\pi})^2 \left\{ \frac{1}{2}\tilde{C}_T\dot{\gamma}^2 + \frac{\gamma^2}{2\tilde{L}_T} \right\} \tag{5.62}$$

$$= (\frac{\Phi_o}{2\pi})^2 \left\{ \frac{1}{2}(C_{TL} + \mu_m(x_j)C_J)\dot{\gamma}^2 + \frac{1}{2}\left(\frac{1}{L_o}\int_0^L \left(\frac{d\mu_m(x)}{dx} \right)^2 dx + \frac{1}{L_J}\left(\mu_m(x_J)\right)^2 \right)\gamma^2 \right\} \tag{5.63}$$

$$= (\frac{\Phi_o}{2\pi})^2 \left\{ \frac{1}{2}(C_{TL} + \mu_m(x_j)C_J)\dot{\gamma}^2 + \frac{\gamma^2}{2L_o}\int_0^L \left(\frac{d\mu_m(x)}{dx} \right)^2 dx + \frac{\gamma^2}{2L_J}\left(\mu_m(x_J)\right)^2 \right\} \tag{5.64}$$

The nonlinear JJ inductance L_J is a function of the phase as given as

$$L_J = \frac{L_{J_o}}{\cos\phi} \tag{5.65}$$

and for our experimental setup

$$L_J = \frac{L_{J_o}}{\cos[\phi_{dc} + a_{ac}\sin(\omega_{ac}t) + \gamma]} \tag{5.66}$$

ϕ_{dc} is the phase from the DC flux bias. a_{ac} is the amplitude of the pumping tone and ω_{ac} is the frequency of the pumping which is set at twice the resonant frequency. γ is the phase from the flux in the resonant cavity or the flux from the input signal to be amplified. and

$$\cos[\phi_{dc} + a_{ac}\sin(\omega_{ac}t) + \gamma] \tag{5.67}$$

$$= \cos[\phi_{dc} + a_{ac}\sin(\omega_{ac}t)]\cos\gamma - \sin[\phi_{dc} + a_{ac}\sin(\omega_{ac}t)]\sin\gamma \tag{5.68}$$

Taylor expand $\sin\gamma$ gives 1^{st} and 3^{rd} of γ which will not contribute to the parametric pumping so we neglect these terms and the phase is further approximated as:

$$\cos[\phi_{dc} + a_{ac}\sin(\omega_{ac}t) + \gamma] \approx \cos[\phi_{dc} + a_{ac}\sin(\omega_{ac}t)]\cos\gamma \tag{5.69}$$

and Taylor expand around ϕ_{dc}

$$\cos[\phi_{dc} + a_{ac}\sin(\omega_{ac}t)] = \cos\phi_{dc} - a_{ac}\sin\phi_{dc}\sin(\omega_{ac}t) \tag{5.70}$$

Substitute Equations 5.67,5.69,5.70 into equation 5.66

$$L_J = \frac{L_{J_o}}{(\cos\phi_{dc} - a_{ac}\sin\phi_{dc}\sin(\omega_{ac}t))\cos\gamma} \tag{5.71}$$

and the system Hamiltonian after substitute Equation 5.64 in is:

$$
\begin{aligned}
H &= \left(\frac{\Phi_o}{2\pi}\right)^2 \left\{\frac{1}{2}(C_{TL}+\mu_m(x_j)C_J)\dot{\gamma}^2 + \frac{\gamma^2}{2L_o}\int_0^L \left(\frac{d\mu_m(x)}{dx}\right)^2 dx\right\} && (5.72)\\
&\quad + \left(\frac{\Phi_o}{2\pi}\right)^2 \left\{\frac{(\cos\phi_{dc} - a_{ac}\sin\phi_{dc}\sin(\omega_{ac}t))\gamma^2\cos\gamma}{2L_{J_o}}\mu_m^2(x_J)\right\} && (5.73)\\
&= H_{linear} + H_{nonlinear} && (5.74)
\end{aligned}
$$

with

$$
H_{linear} = \left(\frac{\Phi_o}{2\pi}\right)^2 \left\{\frac{1}{2}(C_{TL}+\mu_m(x_j)C_J)\dot{\gamma}^2 + \frac{\gamma^2}{2L_o}\int_0^L \left(\frac{d\mu_m(x)}{dx}\right)^2 dx\right\} \quad (5.75)
$$

and

$$
H_{nonlinear} = \left(\frac{\Phi_o}{2\pi}\right)^2 \left\{\frac{(\cos\phi_{dc} - a_{ac}\sin\phi_{dc}\sin(\omega_{ac}t))\gamma^2\cos\gamma}{2L_{J_o}}\mu_m^2(x_J)\right\} \quad (5.76)
$$

Taylor expand $\cos\gamma$ around $\gamma = 0$ as

$$
\cos\gamma = 1 - \frac{1}{2}\gamma^2 + \frac{1}{24}\gamma^4 + \cdots \quad (5.77)
$$

and substitute into the nonlinear Hamiltonian:

$$
\begin{aligned}
H_{nonlinear} &= \left(\frac{\Phi_o}{2\pi}\right)^2 \left\{\frac{(\cos\phi_{dc} - a_{ac}\sin\phi_{dc}\sin(\omega_{ac}t))\gamma^2\cos\gamma}{2L_{J_o}}\mu_m^2(x_J)\right\} && (5.78)\\
&= \left(\frac{\Phi_o}{2\pi}\right)^2 \frac{(\cos\phi_{dc} - a_{ac}\sin\phi_{dc}\sin(\omega_{ac}t))\gamma^2}{2L_{J_o}}\mu_m^2(x_J) && (5.79)\\
&\quad - \left(\frac{\Phi_o}{2\pi}\right)^2 \frac{(\cos\phi_{dc} - a_{ac}\sin\phi_{dc}\sin(\omega_{ac}t))\gamma^4}{2L_{J_o}}\frac{1}{2}\mu_m^2(x_J) && (5.80)\\
&= \left(\frac{\Phi_o}{2\pi}\right)^2 \frac{\mu_m^2(x_J)\gamma^2}{2L'_J} - \left(\frac{\Phi_o}{2\pi}\right)^2 \frac{\mu_m^2(x_J)\gamma^4}{2L'_J}\frac{1}{2} && (5.81)
\end{aligned}
$$

with $L'_J = L_{J_o}/[\cos\phi_{dc} - a_{ac}\sin\phi_{dc}\sin(\omega_{ac}t)]$. The total Hamiltonian is

$$
\begin{aligned}
H &= \left(\frac{\Phi_o}{2\pi}\right)^2 \left\{\frac{1}{2}(C_{TL}+\mu_m(x_j)C_J)\dot{\gamma}^2 + \frac{\gamma^2}{2L_o}\int_0^L \left(\frac{d\mu_m(x)}{dx}\right)^2 dx\right\} && (5.82)\\
&\quad + \left(\frac{\Phi_o}{2\pi}\right)^2 \frac{\mu_m^2(x_J)\gamma^2}{2L'_J} - \left(\frac{\Phi_o}{2\pi}\right)^2 \frac{\mu_m^2(x_J)\gamma^4}{2L'_J}\frac{1}{2} && (5.83)\\
&= (\frac{\Phi_o}{2\pi})^2 \left\{\frac{1}{2}\tilde{C}_T\dot{\gamma}^2 + \frac{\gamma^2}{2\tilde{L}_T}\right\} - (\frac{\Phi_o}{2\pi})^2 \frac{\gamma^4}{4L'_J}\mu_m^2(x_J) && (5.84)
\end{aligned}
$$

with

$$
\begin{aligned}
\tilde{C}_T &= C_{TL} + \mu_m(x_j)C_J && (5.85)\\
\frac{1}{\tilde{L_T}} &= \frac{1}{L_o}\int_0^L \left(\frac{d\mu_m(x)}{dx}\right)^2 dx + \frac{1}{L'_J}\mu_m^2(x_J) && (5.86)
\end{aligned}
$$

In the quantized mode

$$
\begin{aligned}
\hat{H} &= (\frac{\Phi_o}{2\pi})^2 \sum_m \left(\frac{1}{2}\tilde{C}_T\dot{\gamma}_m^2 + \frac{\gamma_m^2}{2\tilde{L}_T}\right) - \frac{1}{2}(\frac{\Phi_o}{2\pi})^2 \frac{\mu_m^2(x_j)}{2L'_J}\left(\sum_m \gamma_m\right)^4 && (5.87)\\
&= (\frac{\Phi_o}{2\pi})^2 \sum_m \left(i\sqrt{\frac{\tilde{C}_T}{2}}\dot{\gamma}_m + \frac{\gamma_m}{\sqrt{2\tilde{L}_T}}\right)\left(-i\sqrt{\frac{\tilde{C}_T}{2}}\dot{\gamma}_m + \frac{\gamma_m}{\sqrt{2\tilde{L}_T}}\right) && (5.88)\\
&\quad -\frac{1}{2}(\frac{\Phi_o}{2\pi})^2 \frac{\mu_m^2(x_j)}{2L'_J}\left(\sum_m \gamma_m\right)^4 && (5.89)\\
& && (5.90)
\end{aligned}
$$

writing

$$
\begin{aligned}
a^\dagger &= (\frac{\Phi_o}{2\pi})\frac{1}{\sqrt{\hbar\omega_m}}\left(i\sqrt{\frac{\tilde{C}_T}{2}}\dot{\gamma}_m + \frac{\gamma_m}{\sqrt{2\tilde{L}_T}}\right) && (5.91)\\
a &= (\frac{\Phi_o}{2\pi})\frac{1}{\sqrt{\hbar\omega_m}}\left(-i\sqrt{\frac{\tilde{C}_T}{2}}\dot{\gamma}_m + \frac{\gamma_m}{\sqrt{2\tilde{L}_T}}\right) && (5.92)
\end{aligned}
$$

and

$$\hat{\gamma}_m = \frac{2\pi}{\Phi_o}\sqrt{\frac{2\hbar}{\omega_m \tilde{C}_{T,m}}}(a_m^\dagger + a_m) \tag{5.93}$$

$$\hat{\hat{\gamma}}_m = i\frac{2\pi}{\Phi_o}\sqrt{\frac{\hbar\omega_m}{2\tilde{C}_{T,m}}}(a_m^\dagger - a_m) \tag{5.94}$$

$$\tag{5.95}$$

$$\hat{H} = \sum_m \hbar\omega_m a_m^\dagger a_m - \frac{1}{2}(\frac{\Phi_o}{2\pi})^2 \frac{\mu_m^2(x_j)}{2L_J'}\left(\sum_m \gamma_m\right)^4 \tag{5.96}$$

with $\omega_m = 1/\sqrt{\tilde{L}_{T,m}\tilde{C}_{T,m}}$

The above Hamiltonian now takes the form

$$\hat{H} = \hat{H}_L - \hat{H}_{NL} \tag{5.97}$$

with

$$\hat{H}_L = \sum_m \hbar\omega_m a_m^\dagger a_m \tag{5.98}$$

and

$$\hat{H}_{NL} = \frac{1}{2}(\frac{2\pi}{\Phi_o})^2 \frac{\mu_m^2(x_j)}{2L_J'}\left(\sum_m \sqrt{\frac{\hbar}{2\tilde{C}_{T,m}\omega_m}}(a_m^\dagger + a_m)\right)^4 \tag{5.99}$$

To see mode coupling and keeping only the fundamental mode. Appendix B shows the details of the 4^{th} order terms with all the modes. The $a^\dagger - a$ term will be useful if there is

nonlinear capacitance in the system Hamiltonian.

$$\begin{aligned} & \left(\sqrt{\frac{\hbar}{2\tilde{C}_{T,m}\omega_m}}(a_m^\dagger + a_m)\right)^4 \\ = & \left(\frac{\hbar}{2\tilde{C}_{T,m}\omega_m}\right)^2 6a_j^\dagger a_j \\ & + \left(\frac{\hbar}{2\tilde{C}_{T,m}\omega_m}\right)^2 2(a_j^{\dagger 2} - a_j^2) \\ & + \left(\frac{\hbar}{2\tilde{C}_{T,m}\omega_m}\right)^2 \left[6\left(a_j^\dagger a_j\right)^2 + a_j^{\dagger 2}a_j^{\dagger 2} + 2a_j^{\dagger 2}a_j^\dagger a_j\right] \\ & + \left(\frac{\hbar}{2\tilde{C}_{T,m}\omega_m}\right)^2 (a_j^2 a_j^2 + 2a_j^2 a_j^\dagger a_j + 2a_j^{\dagger 2}(a_j^\dagger a_j + 2) + 2a_j^2 a^\dagger a_j + 3) \end{aligned} \tag{5.100}$$

The 1^{st} term adds to the linear term of the Hamiltonian and is responsible for the shift of the resonant frequency.

$$\hbar\Delta\omega = -\frac{1}{2}(\frac{2\pi}{\Phi_o})^2 \frac{\mu_m^2(x_j)}{2L_{J'}} \left(\frac{\hbar}{2\tilde{C}_{T,m}\omega_m}\right)^2 6a_j^\dagger a_j \tag{5.101}$$

$$= -\frac{1}{2}(\frac{2\pi}{\Phi_o})^2 \frac{\mu_m^2(x_j)}{2L'_J} \left(\frac{\hbar}{2\tilde{C}_{T,m}\omega_m}\right)^2 6a_j^\dagger a_j \tag{5.102}$$

$$= -\frac{1}{2}(\frac{2\pi}{\Phi_o})^2 \frac{\mu_m^2(x_j)}{2L'_{J_1}} \left(\frac{\hbar}{2\tilde{C}_{T,m}\omega_m}\right)^2 6a_j^\dagger a_j \tag{5.103}$$

$$= -\frac{1}{2}(\frac{2\pi}{\Phi_o})^2 \eta_l \frac{\hbar^2}{8\tilde{C}_{T,m}} 6a_j^\dagger a_j \tag{5.104}$$

$$= -\hbar K a_j^\dagger a_j \tag{5.105}$$

With $L'_{J_1} = L_{J_o}/\cos\phi_{dc}$ by dropping the AC pumping effect. and the Josephson inductance participation ratio $\eta_l = \frac{\mu_m^2(x_j)}{L'_{J_1}} / \frac{1}{\tilde{L}_T}$, and the self kerr term

$$K = (\frac{2\pi}{\Phi_o})^2 \eta_l \frac{3\hbar}{8\tilde{C}_{T,m}} \tag{5.106}$$

The 2^{nd} term is the Hamiltonian for degenerate parametric amplification when the Joseph-

son inductance is modulated or pumped at twice the resonant frequency. (7)

Chapter 6

CHARGE SENSITIVITY

The fundamental picture of dispersive charge detection using a nonlinear resonator is illustrated in Fig.6.1. A person standing on a swing oscillates at resonant frequency $f_o = \sqrt{\frac{l_{n=0}}{g}}$ as shown in Fig.6.1(a). When he sits on a chair made of one electron charge as in Fig.6.1(b) the effective length of the swing is longer and the swing will oscillate at a new frequency $f_o = \sqrt{\frac{l_{n=1}}{g}}$. This way a charge change of Δne will be detected by looking at the change of the resonant frequency Δf_o and larger Δf_o with same value of Δne indicates higher charge sensitivity.

In our setup, a superconducting CPW resonator was inductively shunted by a Josephson inductance L_J which is regulated by the charge state on the gate of the CPT. When the gate with capacitance C_g of the CPT is modulated with $V = V_g \sin(\omega_m t)$ and the corresponding charge variation is $\delta q_g = C_g V = C_g V_g \sin(\omega_m t)$ the frequency shift induced by charge variation is:

$$\delta f = \frac{\partial f}{\partial q} \delta q \tag{6.1}$$

$$= \frac{\partial f}{\partial q} C_g V_g \sin(\omega_m t) \tag{6.2}$$

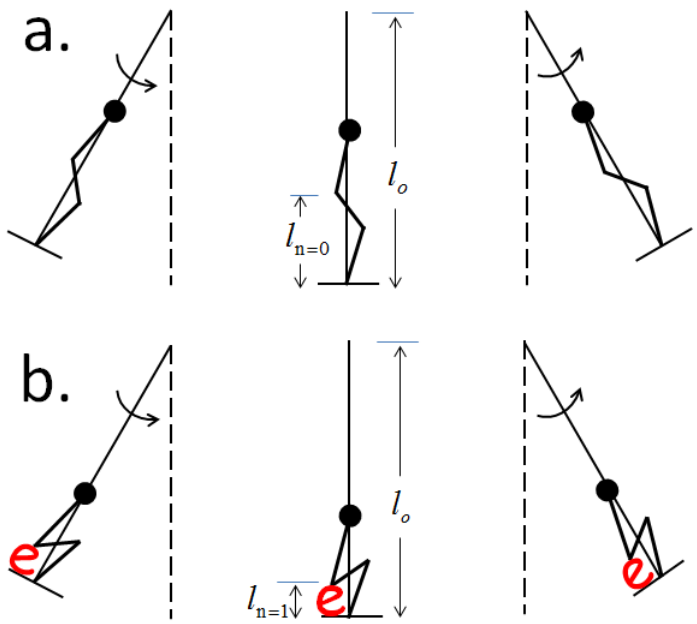

Figure 6.1: Illustration of dispersive charge detection using a nonlinear resonator

integrating δf over time t gives

$$\int \delta f dt = \int \frac{\partial f}{\partial q} C_g V_g \sin(\omega_m t) dt \tag{6.3}$$

$$\delta f t = \frac{1}{\omega_m} \frac{\partial f}{\partial q} C_g V_g \cos(\omega_m t) \tag{6.4}$$

The new charge modulated amplitude of the resonator is

$$V_{fm}(t) = A_c \cos\left(f_o t + \delta f t + \phi\right) \tag{6.5}$$

$$= A_c \cos\left(2\pi f_o t + \frac{1}{\omega_g} \frac{\partial f}{\partial q} C_g V_o \cos(\omega_g t)\right) \tag{6.6}$$

$$= A_c \sum_{n=-\infty}^{\infty} J_n\left(\frac{1}{\omega_g} \frac{d\omega}{dq} C_g V_o\right) \cos[(\omega_o + n\omega_m) t] \tag{6.7}$$

So side bands will be generated when the gate of the CPT is modulated and the side bands heights are proportional to the resonant frequency shift per charge when other parameters

are fixed. The output microwave signal is :

$$s = v_o \Gamma_n \sum_{n=-\infty}^{\infty} J_n \left(\frac{1}{\omega_g} \frac{d\omega}{dn_g} \frac{C_g V_o}{e} \right) \cos[(\omega_o + n\omega_m)t + \phi] \tag{6.8}$$

change in the reflection due to the charge δq modulation is:

$$\begin{aligned} \Delta s &= v_o \Gamma_n \sum_{n=-\infty}^{\infty} J_n \left(\frac{1}{\omega_g} \frac{d\omega}{dn_g} \frac{C_g V_o}{e} \right) \cos[(\omega_o + n\omega_m)t + \phi] \qquad (6.9) \\ &\quad - v_o \Gamma_o J_o \left(\frac{1}{\omega_g} \frac{d\omega}{dn_g} \frac{C_g V_o}{e} \right) \cos[(\omega_o + n\omega_m)t + \phi] \\ &= v_o \Gamma_n \sum_{n=-\infty}^{\infty} J_n \left(\frac{1}{\omega_g} \frac{d\omega}{dn_g} \frac{C_g V_o}{e} \right) \cos[(\omega_o + n\omega_m)t + \phi] \qquad (6.10) \\ &\quad - v_o \Gamma_o \cos(\omega_o t + \phi) \end{aligned}$$

For charge sensitivity characterization the reflected microwave signal change by charge variation is given as: (**?**)

$$|\delta S_{11}| = \left| \frac{\partial S_{ss}}{\partial f} \right| \frac{\partial f}{\partial n_g} \frac{\delta q}{C_g V_o} \tag{6.11}$$

Finally the fundamental charge sensitivity of our charge detector is:

$$\begin{aligned} \delta q &= \frac{\delta S_{11}}{|\partial S_{11}/\partial f|} \frac{C_g V_o}{\partial f / \partial n_g} \qquad (6.12) \\ &= \frac{\sqrt{P_n / BW}}{|\partial S_{11}/\partial f|} \frac{C_g V_o}{\partial f / \partial n_g} \qquad (6.13) \end{aligned}$$

P_n is the power of each side band and BW is the band width of the spectrum analyzer. For high charge sensitivity or smaller δq, large $|\partial S_{11}/\partial f|$ and $\partial f/\partial n_g$ is preferred. $\partial f/\partial n_g$ can be determined from frequency shift plot of Fig 8.13. $\partial f/\partial n_g$ is larger at the resonant

frequency as proved in reference (?). The optimal point would be the critical couple case where the resonance has the deepest depth. This has been proved by our experiment data of Fig. 8.16.

However, the sensitivity is also determined by the amplifier chain gain and noise level. In our measurement, The best charge sensitivity point is a balance between all the parameters.

6.1 current biasing regime

In the middle of our effort to maximize our charge sensitivity by varing all the related parameters we found much higher charge sensitivity location at $f_o = 5.756GHz$. At this spot $\partial\omega/\partial n_g$ is zero as can be seen from figure (8.13). Above charge sensitivity theory lose its validation at this point. Below alternative theory base on the SQUID loop current relationship is carried out for interpretating the charge senstivity.

Figure(4.1) shows that our CPT and the central conductor of the CPW form a superconducting current loop that is usually quoted as SQUID (Superconducting quantum interference device) (37). It has a continuous superconducting current circulating in the loop that could be adjust by the flux threading the loop. When an alternating voltage is applied on the gate of the CPT, an alternating current is going into the SQUID loop at the same time through the gate capacitor. Figure (6.2) shows the two currents in a SQUID. I_{loop} is the current in the loop that could be tuned by the threading flux. $I_{external}$ is equivalent to the current coming in through the gate port. The two Josephson junctions are identified as I_1 and I_2.

Assuming equal junctions ($I_{o,1} = I_{o,1}$) equations for the current dynamics of a SQUID loop are:

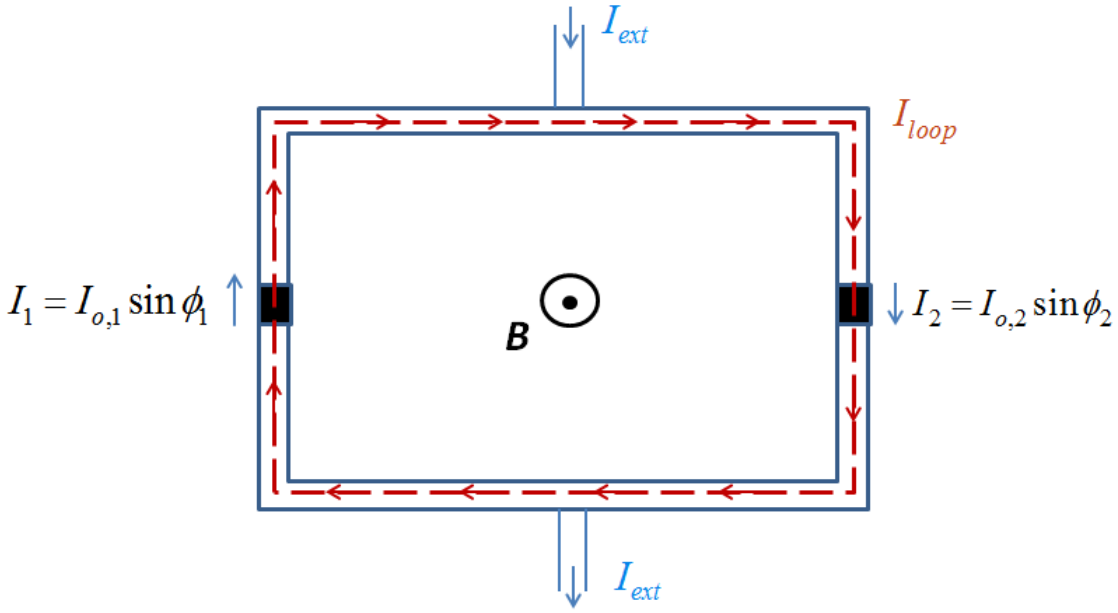

Figure 6.2: A SQUID loop formed with two JJs. There is an internal current I_{loop} going on all the time and it determines the external current I_{ext} that could pass through the loop without biasing the JJs out of superconducting regime, or the other way around.

$$I_{loop} = \frac{I_1 + I_2}{2} = I_o \frac{\sin\phi_1 + \sin\phi_2}{2} = I_o \sin\left(\frac{\phi_1 + \phi_2}{2}\right)\cos\left(\frac{\phi_1 - \phi_2}{2}\right) \tag{6.14}$$

$$I_{ext} = I_1 - I_2 = I_o(\sin\phi_1 - \sin\phi_2) = 2I_o \cos\left(\frac{\phi_1 + \phi_2}{2}\right)\sin\left(\frac{\phi_1 - \phi_2}{2}\right) \tag{6.15}$$

Equation (6.14) shows that from the loop current point of view the two JJs can be treated as a single junction with new current equation:

$$I_{loop} = I_{o,loop}\sin\phi_{loop} \tag{6.16}$$

with $I_{o,loop} = I_o \cos\left(\frac{\phi_1 - \phi_2}{2}\right) = I_o \cos\phi_{ext}$ and $\phi_{ext} = \frac{\phi_1 - \phi_2}{2}$

The new Josephson inductance

$$L_{J_{o,loop}} = \frac{\Phi_o}{2\pi I_{o,loop}} \tag{6.17}$$

$$= \frac{\Phi_o}{2\pi I_o \cos\phi_{ext}} \tag{6.18}$$

And the flux tunable inductance is:

$$L_{J,loop} = L_{J_{o,loop}} / \cos\phi_{loop} \tag{6.19}$$

$$= \frac{\Phi_o \sin\phi_{ext}}{2\pi I_{ext} \cos\phi_{ext}} \tag{6.20}$$

or

$$I_{ext} = \frac{\Phi_o \tan\phi_{ext}}{2\pi L_{J,loop}} \tag{6.21}$$

I_{ext} is the current introduced into the SQUID loop by the voltage modulation on the gate and $L_{J,loop}$ is the Josephson inductance across the two JJs. The CPW resonator is shunted by this inductance and the resonant frequency will be tuned by this inductance or the gate current I_{ext}. ϕ_{ext} is the phase across the two JJs that could be adjusted by the flux threading the loop.

At $f_o = 5.756GHz$ $\phi_{ext} \approx 0$ and the supercurrent in the loop is near its maximum value I_o. Fig. (6.3) shows the change of Josephson inductance $L_{J,loop}$ by external current I_{ext}. When external current I_{ext} is small it will induce an infinite change on the inductance L_J, and significant shift on the resonant frequency consequently. To quantitatively evaluate the resonant frequency shift.

When the gate is modulated with voltage $V = V_g \sin\omega_g t$ the induced current is:

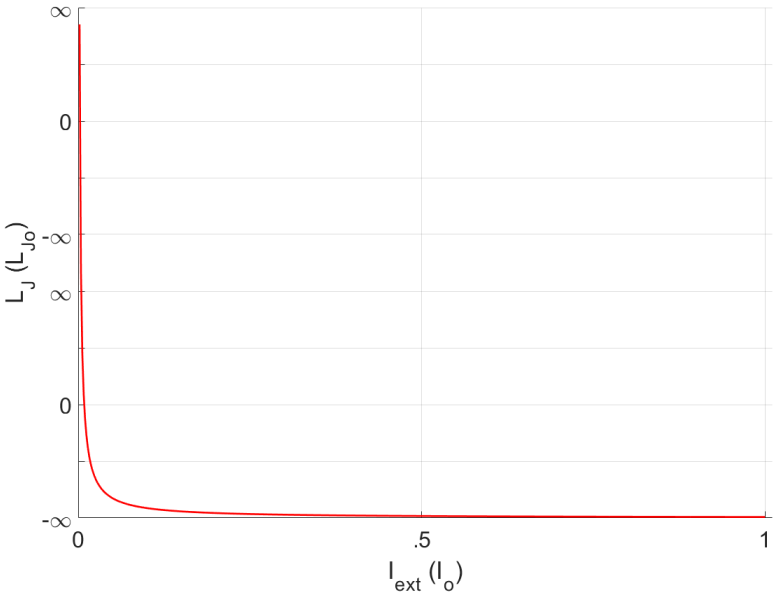

Figure 6.3: I_{ext} and loop inductance $L_{J,loop}$. Phase in the loop $\approx \pi$

$$\dot{q} = C_g \dot{V} \tag{6.22}$$

$$I_g = \omega_g C_g V_o \cos(\omega_g t) \tag{6.23}$$

$$= I_{g_o} \cos(\omega_g t) \tag{6.24}$$

With $I_{g_o} = \omega_g C_g V_o$ and

New resonant frequency of the resonator is:

$$
\begin{aligned}
f_o' &= \frac{1}{\sqrt{L_T C_T}} && (6.25)\\
&= \frac{1}{\sqrt{C_T}}\sqrt{\frac{1}{L_o}+\frac{1}{L_{J,loop}}} && (6.26)\\
&= f_o + f_o\frac{L_o \cot\phi_{ext} I_{ext}}{2\hbar/e} && (6.27)\\
&= f_o + f_o\frac{L_o \cot\phi_{ext}\omega_g C_g V_o \sin\omega_g t}{2\hbar/e} && (6.28)
\end{aligned}
$$

So the equivalent frequency shift per charge is:

$$
\frac{df}{dn_g} = f_o\frac{L_o \cot(\phi_{ext})\omega_g e}{2\hbar/e} \quad (6.29)
$$

At $f_o = 5.756GHz$, $\cot\phi_{ext} \approx \infty$ and $df/dn_g \approx \infty$. This explains the much large charge sensitivity at this spot. In empirical measurement $df/dn_g \approx \infty$ will be limited to a certain value. With our current measurement scheme, $df/dn_g \approx \infty$ couldn't be evaluated as it is always zero in our frequency shift plot. An alternative method for retrieving $df/dn_g \approx \infty$ is explained in Chapter 8 using Bessel function simulation.

$$
\begin{aligned}
\int_o^t f_o' dt &= \int\left(f_o + f_o\frac{L_o \cot\phi_{ext} I_{g_o}\sin(\omega_g t)}{2\hbar/e}\right)dt && (6.30)\\
f_o' t &= f_o t + f_o\frac{L_o \cot\phi_{ext} I_{g_o}\cos(\omega_g t)}{2\omega_g\hbar/e} && (6.31)
\end{aligned}
$$

Modulated output:

$$
s' = v_o\Gamma_n\sum_{n=-\infty}^{\infty} J_n\left(\frac{1}{\omega_g}\frac{d\omega}{dn_g}\frac{C_g V_o}{e}\right)\cos[(\omega_o + n\omega_m)t + \phi] \quad (6.32)
$$

which is same form as Equation (6.8) except that $d\omega/dn_g$ will be significantly larger.

To maximize δs $\Gamma_n(n \neq 0)$ need to be large and Γ_o needs to be as small as possible. Γ_o is smaller at resonance and acquires minimum at critical coupling $Q_i = Q_e$ which is also verified in Fig. (CouplingtransitionAmp).

6.2 linear sensitivity limited by noise and the amplification chain

Due to a collection of two level systems there is noise with the spectral density of $1/f^{\alpha}$. This give two issues to the charge detector:

1) With presence of the charge noise the sensitivity will degrade at low frequency up to a frequency called the $1/f$ corner. Above this the noise is dominated by the system noise $k_B T_N$. To overcome this noise problem, the charge detector is operated at MHz frequency, the $1/f$ noise will not be significant. Also the JPA intrinsic with the charge detector could be applied to squeeze the charge signal and consequently suppress the $1/f$ noise. (6)

2) Quasiparticle poisoning: even at mK temperature, unpaired quasiparticles will always be observed. When quasiparticles tunnel through the CPT island the symmetry of the energy diagram will be shifted from 'even' state to mix of 'even' and 'odd' state. The measured resonant frequency can suddenly shift from one value to another as shown in Figure (8.13) of our measured frequency shift. Quasiparticle trapping can be surpressed with thin film island and we fabricated our island with $9n$m thickness island only. All the DC and micrwave lines are heavily attentuation to surpress the noise power that could potentially excite quasiparticles. The maximum charge sensitivity point in the charge detector is at the center of the Coulomb blockade. It is the spot with minimum quasiparticle poisoning as can be evaluated by Figure (8.13). The resonant frequency shift is least sensitive to DC

charge in the island but most sensitive to the current following into the island from the gate. At the center of Coulomb blockade $\partial f/\partial n_g = 0$, so the CPT is immune to $1/f$ noise. Fig. 8.4 shows the noise floor at the center and edge of the Coulomb blockade respectively. Fig. 8.4(a) shows the noise floor at the center of the Coulomb blockade and Fig. 8.4(b) is the noise floor at the edge of the Coulomb blockade. The fact that he noise floor at the center of the Coulomb blockade is significantly lower than the one at the edge of the blockage verifies that the $1/f$ noise will not degrade the charge detector performance.

Chapter 7

EXPERIMENTAL SETUP

Our measurement was carried out in a standard dilution refrigerator. Due to the relatively low cooling power and multiple semi rigid microwave coaxial cables going through temperature gradient in the dilution unit, the base temperature was raised up to 30 mK instead about 20 mK.

Figure (7.1) is schematic of our measurement setup. A microwave circulator separates the input and output signals and convert S_{11} measurement to S_{12} measurement. This offers the freedom of attenuating the signal input line to minimize injected noise. The output signal is first amplified by a SLUG (Superconducting Low-Inductance Undulatory Galvanometer) amplifier(17) and then a HEMT (High-electron-mobility transistor) amplifier. Niobium coaxial cable from sample to the HEMT amplifier are used to minimize the noise floor in the output signal. DC and microwave signals on the gate and flux ports are combined using a bias-tee. Superconducting wires are used on the DC lines including the microwave switche power supply lines to minimize resistive heating. The DC line for the gate goes through a copper powder filter and a RC filter at base temperature. A 10 $k\Omega$ resistor is added to the flux line at the 4K stage to convert the applied voltage to a current as the flux line needs to be current biased instead of voltage biased as on the

gate. A 20 μF capacitor is added at the 4K stage before the resistor for noise filtering. Two 50Ω microwave SMA caps are anchored at 4K and base temperature stage separately for Y-factor noise measurement and gain calibration. The sample sits deep in a magnetic shield to minimize the static magnetic field.

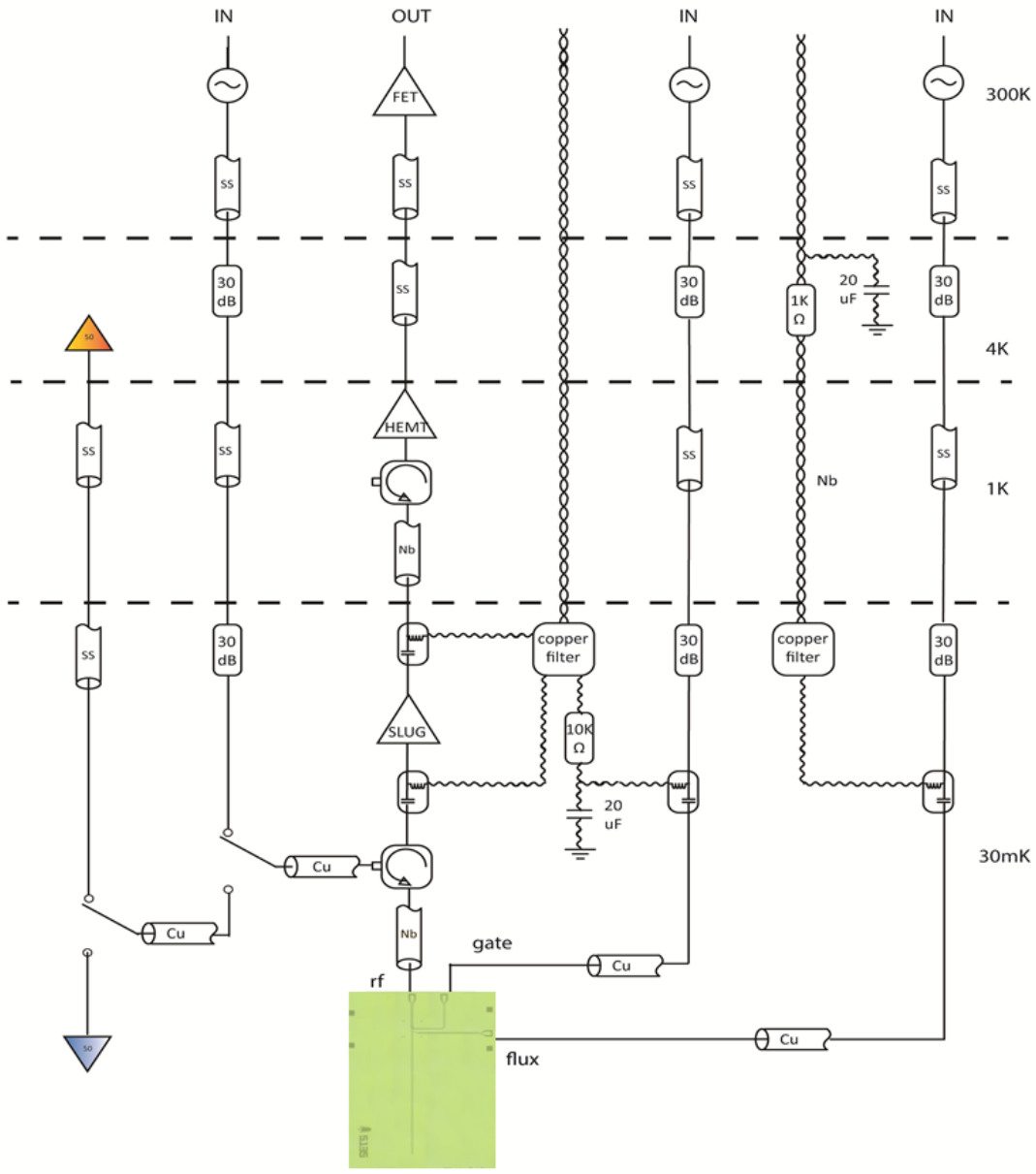

Figure 7.1: measurement setup in our dilution refrigerator. The lines to the right of the drawing are for a Y factor measurement of noise and gain calibration of the amplifier chain.

Figure (7.2) is physical layout of our measurment inside the dilution refrigerator and room

temperature measurement apparatus.

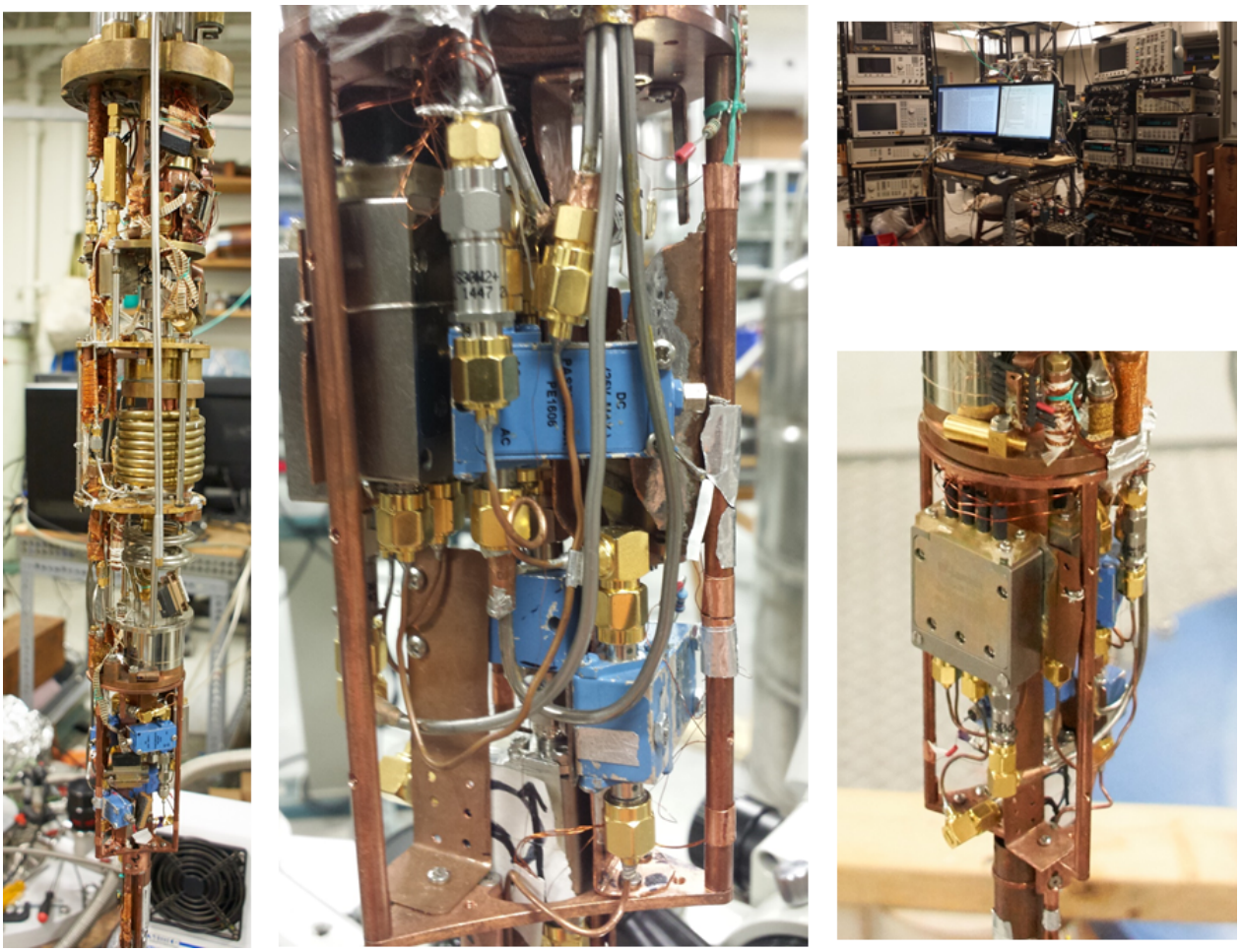

Figure 7.2: Dilution refrigerator setup.

7.1 filtering of gate and flux line

Three different types of filters are effective for certain frequency ranges. (25): RC filters cover the low frequency range 10Hz-10MHz, Pi-filters are effective in the frequency range of 10MHz-1GHz, and metal powder filters (MPF), invented by Martinis in 1987 (24) absorb microwaves in the range of 100MHz-100GHz.

The procedures we followed for fabricating our CPF are as follows. Two high conductivity 38 gauge wires of length one meter were hand braided together as a twisted pair. Some

researchers used a drill to braid wires but the wires by themself will be twisted at the same time which will effectively make them brittle and vulnerable to tension from temperature change during thermal cycling. All the three pairs were hand braided together as a single wire and wound around a metal rod to form a retractable coil. The coil was feed into a cooper tube and filled up with metal powder mixed with epoxy. The cooper powder mix was prepumped with a mechanical pump for about ten minutes to remove the trapped air bubbles. The mixed powder has a jello like property with high viscosity which makes it flows very slow. We choose a rod with diameter of 5mm smaller than the inner diameter of the tube. This leaves enough space for the powder mix to flow all the way to the bottom of the tube without much resistance. The tube was shaken gently during the filling by attaching it to an sonnicating tooth brush to release the air bubbles in the tube intercepted by the mix. At the end the tube was left overnight for the epoxy to harden.

The MPF is mounted at the base temperature of the dilution refrigerator. The wires will need to carry up to 1 mA current. Heating from the resistance of the wires could be large enough to increase the base temperature of our dilution refrigerator unless the resistance of the wires is sufficiently small. Initially we tried with superconducting wire to eliminate heating. However the wires did not survive thermal cycling. High conductivity 38 Gauge Cu wires was used the 2nd time and heat generated by the 1mA current was neglegible.

The attenuation and roll off frequency of RC filters are mainly determined by capacitance of the capacitor. For our purposes high attenuation and low roll off frequency are desired which requires capacitance as high as possible. Capacitor with capacitance of 270μF was used in our RC filter. Change of the capacitance at He temperature was calibrated by measuring the change of the roll off frequency of an RC filter with the same capacitor at room temperature and He temperature. The effective capacitance reduced to 27μF after dunking the RC filter to liquid He.

7.2 SLUG amplifier

Our SLUG amplifier are fabricated by the group of Prof. Robert Mcdermott at the University of Wisconsin, Madison. It is a near quantum limited amplifier, and detailed working principles are explained in reference (29) and (17). In simple terms a resistively shunted SQUID loop was current biased at the critical current point and the flux in the loop is biased at the critical point that external microwave signal will shift the junctions to the voltage state and consequently providing the gain of the amplifier.

Two typical gain profile we have been using are shown in Fig.7.3a. the blue curve has the gain peak at 5.756GHz and the one we used the most. The red curve has its peak at a lower frequency side, but the overall gain in the whole frequency span is reasonably large so we have used it for scans of the frequency shift. Higher gain on both the low and high frequency is critical because the Q of our resonator degrades away from the center frequency and the resonance becomes hard to detect. As a result the frequency shift plot becomes noisy on either the low frequency or high frequency side.

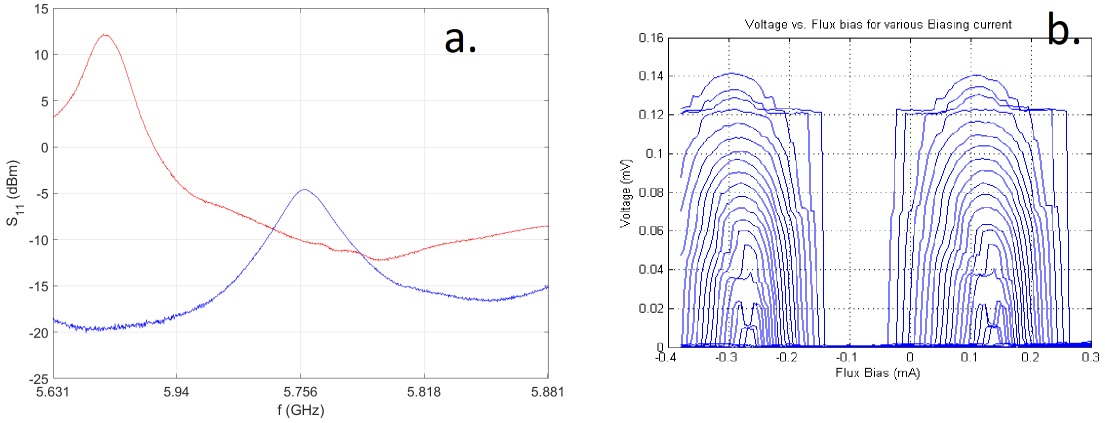

Figure 7.3: The SLUG amplifier gain profiles and flux modulation of output voltage

Fig. 7.3b. is the voltage of SLUG amplifer modulated by the flux bias. At the critical biasing point the output voltage increases rapidly with applied flux, which provides the amplifi-

cation. The clean voltage data indicates that the noise in the flux and voltage biasing lines of the amplifier is low.

Chapter 8

EXPERIMENT RESULT

8.1 JPA Characterization

8.1.1 Phase Modulation

The JPA is a phase sensitive amplifier and the gain of the amplification depends on the phase between the signal the pump tones. Signal in phase with the pump tone will be amplified whereas a signal that is ninety degrees out of phase will be attenuated. Fig. 8.1 shows the measured signal power as a function of the phase between the signal and the pump. Clearly the output power is modulated by the phase, indicating the cCPT can indeed act as a JPA.

8.1.2 Gain of flux and gate pump

The gain of our JPA comes from either pumping on the flux port or the gate port. Both ports give about equal gain at the same pumping power. Figure (8.2) shows the gain at various pumping powers at frequency $f_o = 5.756$ GHz. $f_o = 5.756$ GHz is the point where

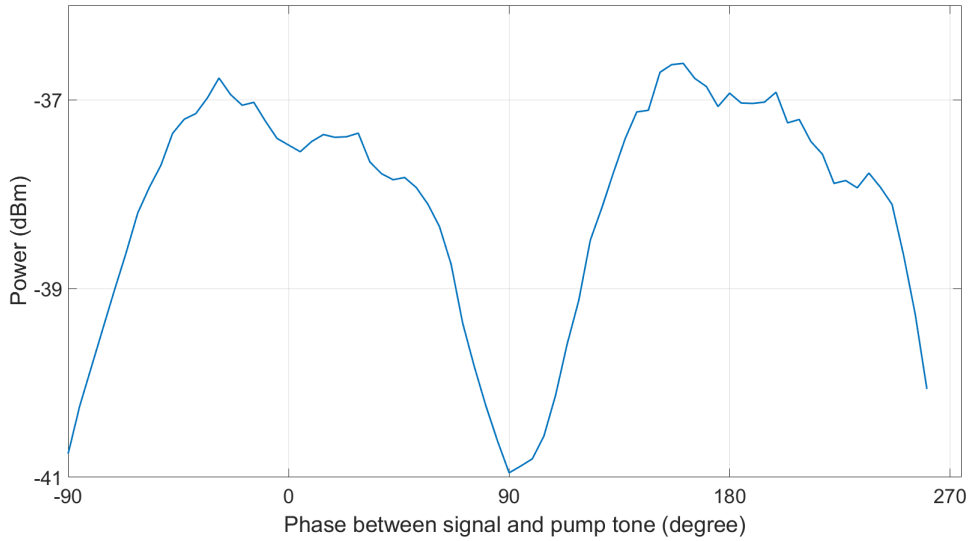

Figure 8.1: Phase modulation of the gain of the JPA. It is a general proof that JPA is phase sensitive amplifier.

the Josephson inductance goes from positive infinite to negative infinite depends on which side of the frequency. The gain increases with larger pumping power. At the same time the frequency of maximum gain was shifted to the lower frequency due to the Kerr constant. If the pumping frequency sits to the left side of this fundamental frequency the maximum gain frequency will shift to the right side. This is also proved by Equation (5.105). The presence of this frequency shift limits the gain of JPA. The frequency shift is a minimum at this frequency point compared to other frequency biasing points so the gain is also a maximum. The beneficial side of the frequency shift is that JPA gains its bandwidth from this frequency shift. As shown by the figure at higher pumping power the JPA has a higher gain and at the same time a wider bandwidth. The shift of the resonant frequency by the pumping tone at various resonant frequency points is further investigated in section 8.2

Fig. 8.3 is the gain with pumping on the gate port. It has similar pattern as pumping on the flux port. The gate port typically provides the same gain as the flux port; however for this data set, the microwave feed through on the fridge was damaged, leading to high attenuation. Effectively the pumping power on the gate line is smaller, and as a result the

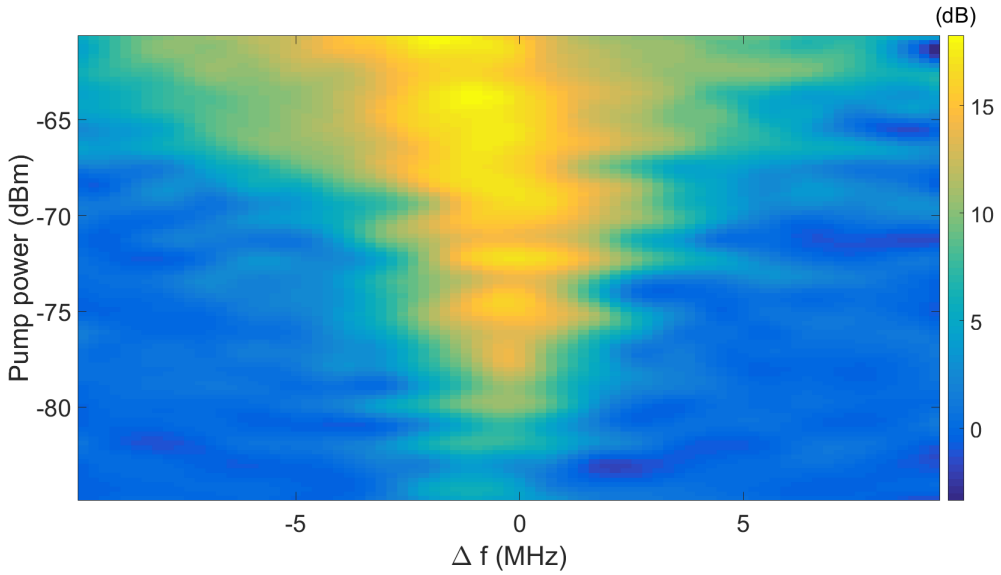

Figure 8.2: Gain of JPA by flux pump as function of pumping amplitude

gain is lower than it should be.

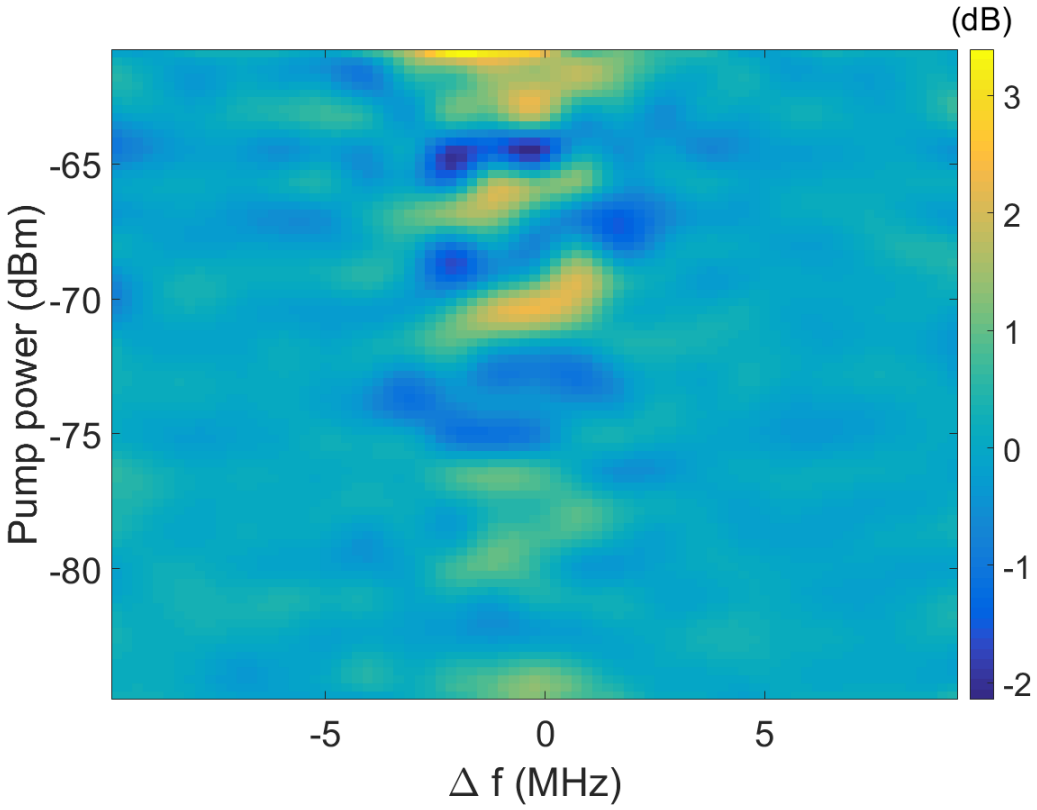

Figure 8.3: Gain of JPA by gate pump as function of pumping amplitude

8.1.3 Noise floor lowering

At $f_o = 5.756$ GHz, the CPT was in its maximum Coulomb blockade regime. The number of Cooper pairs are better defined than their phases. By the quantum uncertainty principle the phase will be less sensitive to noise. Even though the frequency shift by flux is maximum at this point the noise floor is still lower as comparing the two figures in Fig. 8.4. At $f_o = 5.766$ GHz, the CPT was closer to the charge degeneracy point. The number of Cooper pairs is less well defined and the phases are better defined consequently more susceptible to noise. This increased noise on the phase will shift the resonator phases randomly and increase the noise floor. Fig. 8.4 is the power of stimulated emission by pumping at twice the resonant frequency on the flux port. The overall noise floor on the right side is ≈ 5 dB higher. Also the left figure shows that when the pumping power is high enough, the stimulated emission will lower the noise floor as could be observed from the green line. This effect has been also observed in research work on dynamic Casimir effect.(42)

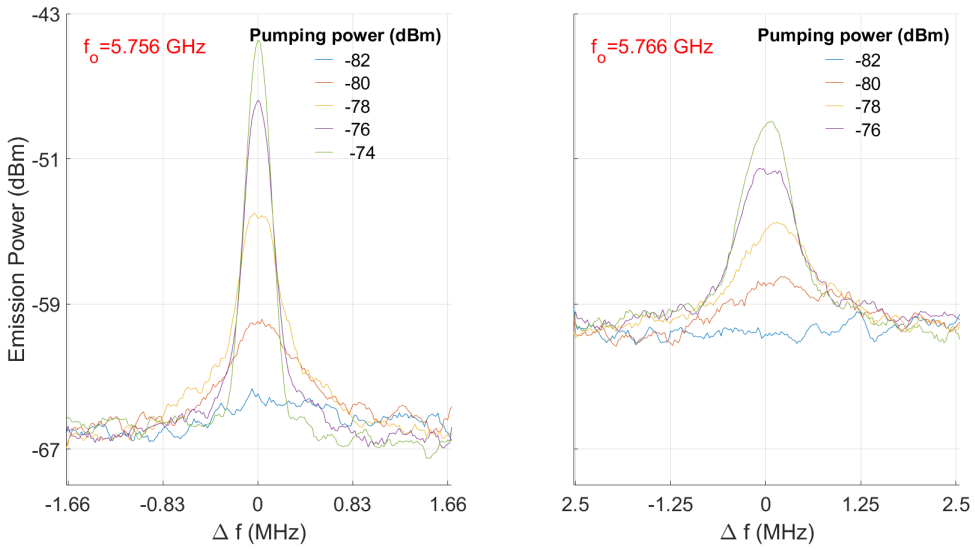

Figure 8.4: the stimulated emission from flux pumping

8.1.4 Stimulated Emission and resonant frequency shift

We observed strong stimulated emission by pumping at twice the resonant frequency from both the flux and gate port. This emission could be explained by the dynamic Casimir effect. (42) (citation here) But solid theoretical analysis is required to fully explain the emission. Characterizing the state of the emission using quantum tomography technique would be a good start. While measuring the power of the stimulated emission we recorded the resonant frequency with a network analyzer. The stimulated emission is always accompanied by resonant frequency shift, by an amount that varies depending on the resonant frequency point as well as the pumping power.

The right panel of Fig. 8.5 shows stimulated emission at a resonant frequency $f_o = 5.756$ GHz for various pumping power. The flux pump tone was at twice of resonant frequency. The stimulated emission power initially increases higher with increasing pumping power, but eventually decreases for pumping power > -70 dBm. The resonant frequency shifted to higher frequency by up to 11 MHz. This frequency bias point gives minimum frequency shift because the participation ratio of the Josephson induction (L_J) is minimum, and variation of L_J has minimum influence on the resonant frequency of the resonator. Frequency shift to a higher value indicates that the L_J is positive and started to become negative.

The stimulated emission power and the frequency shift amplitude and direction depends on the resonant frequency. Fig. 8.6 shows the emission power and frequency shift at $f_o = 5.566$ GHz. At this point L_J is negative and the frequency shifts to the lower frequency side with higher pumping power. The emission power is lower with the same pumping power compared to Fig. 8.5, and the frequency shift amplitude was larger. This larger resonant frequency shift responsible for the lower emission power because the resonance was further detuned from the pump tone.

When the resonant frequency was set at $f_o = 5.776$ GHz, further away from the neutral point of 5.756 GHz, as shown in Fig. 8.7, the resonant frequency shift acquired an even

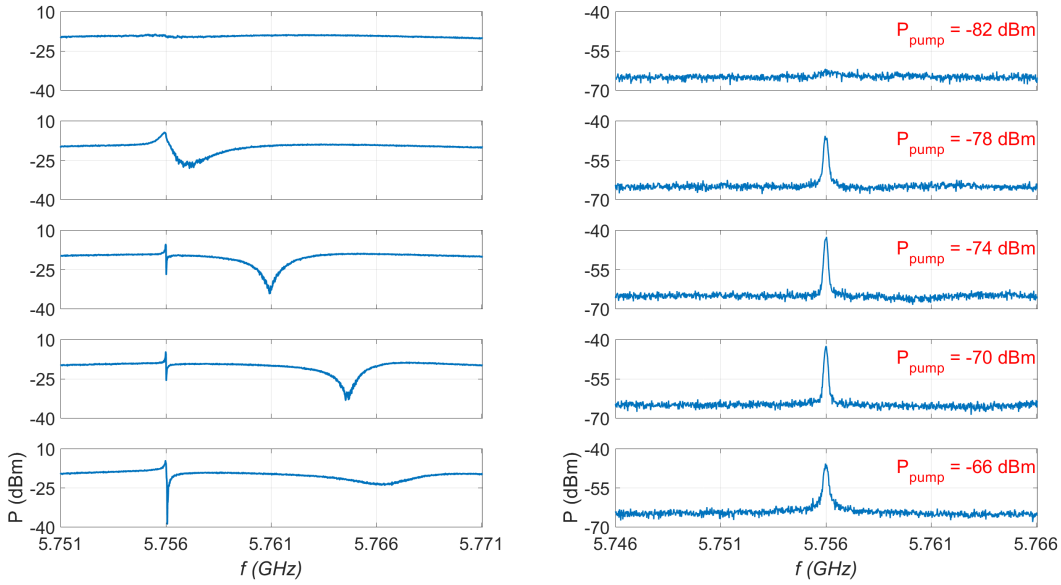

Figure 8.5: the stimulated emission power and frequency shift with various pump power at f_o = 5.756 GHz

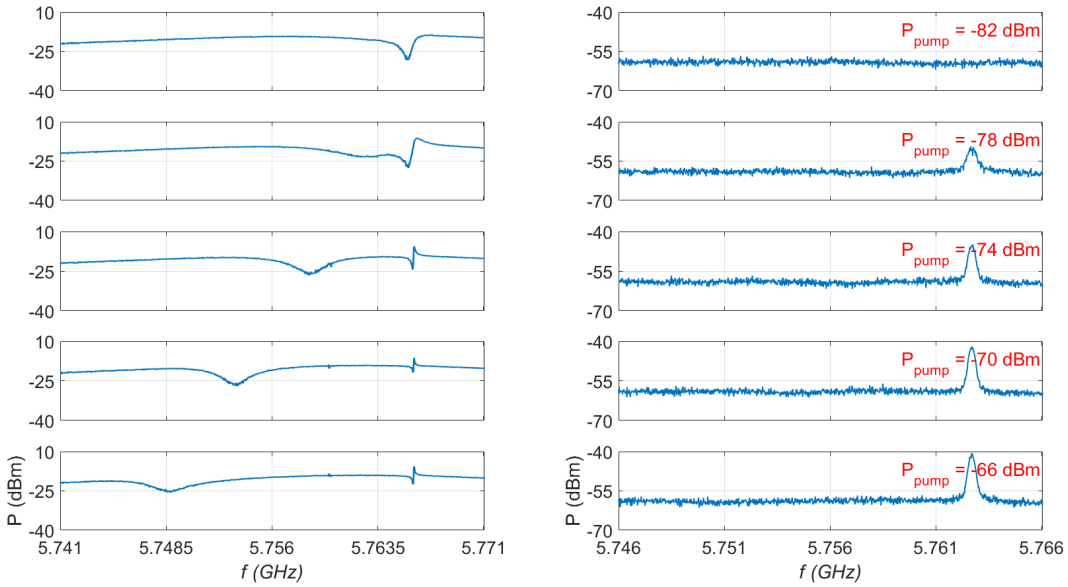

Figure 8.6: Stimulated emission power and frequency shift for various pump power at f_o = 5.766 GHz

larger amplitude and the emission began at a higher pumping power. Again at this point the participating ratio of L_J is bigger and the Kerr effect response for the frequency shift was stronger. The resonance point was further detuned from the pump tone and it required a higher pumping power to initiate the emission because the parametric pumping

gain is smaller.

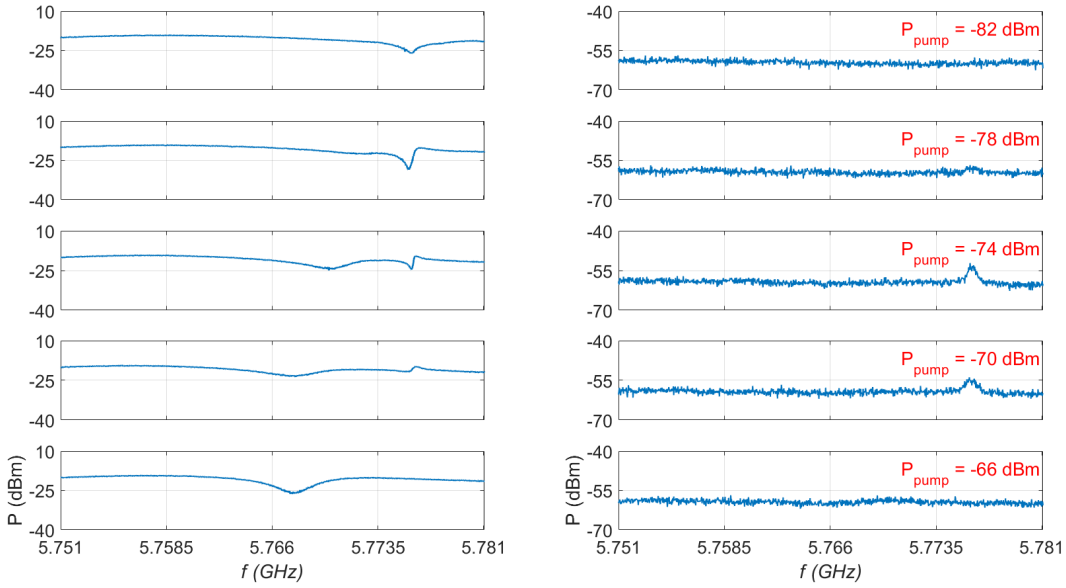

Figure 8.7: Stimulated emission power and frequency shift for various pump power at $f_o = 5.776$ GHz

For now the resonance frequency has been set higher than 5.756 GHz and the resonant frequency was shifted down when the pump tone started. At frequency lower than 5.756 GHz, the participation ratio of L_J becomes positive and the resonance frequency should be shifted to higher frequency when pump tone was on. Figure (8.8) is the emission and frequency shift at frequency $f_o = 5.746$GHz. Because this frequency point is symmetric to frequency 5.766 GHz around 5.756 so It has similar pattern as at frequency 5.766 GHz except that the frequency was shifted up.

8.1.5 Frequency shift by input signal

Because the Josephson inductance L_J is a nonlinear function of the power across the junction, its inductance will change depending on the power in the resonator or the probing power of the network analyzer. The resonant frequency will be shifted consequently. When probing the resonator with the network analyzer, higher input power will give a better S/N ratio; however high input power will bias the resonator away from its intrin-

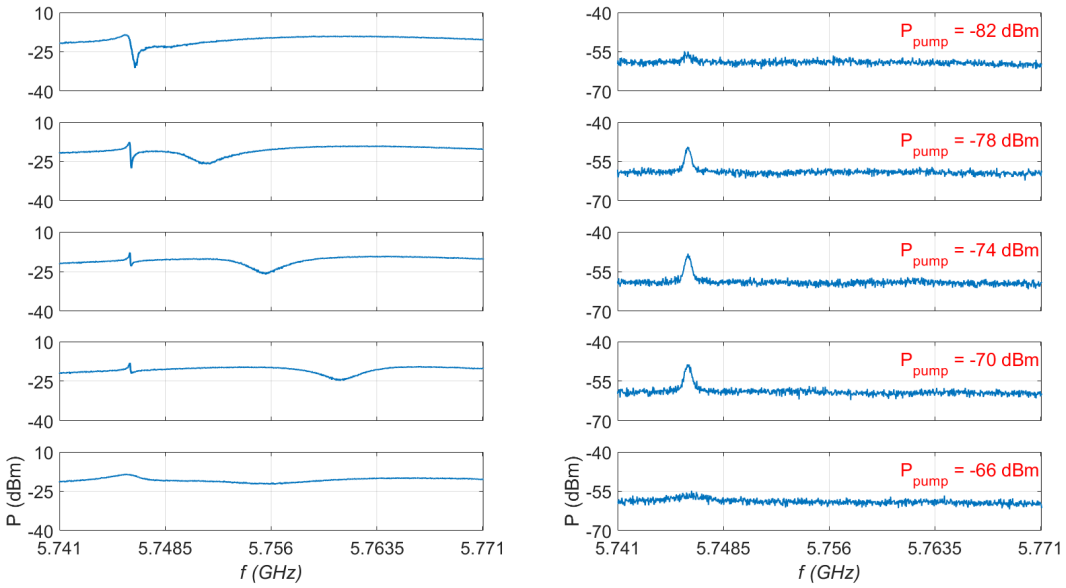

Figure 8.8: Stimulated emission power and frequency shift for various pump powers at $f_o = 5.746$ GHz

sic state and hence the information retrieved will be biased. During all measurements of the resonator the probing power from the NA (network analyzer) has been kept low enough to give about half photon in the resonator. Our amplifier chain has enough gain and low enough noise floor to enable us to still detect the resonance with a good S/N ratio. Fig. 8.9 shows the resonance shift as function of probing power of the NA at different resonant frequency point; -130 dBm power is equivalent to half photon in the resonator. At $f_o = 5.756$ GHz, the Kerr constant is minimum and the frequency shift is relatively small. At $f_o = 5.776$ GHz the Kerr constant is large and the frequency shift is large. $f_o = 5.766$ GHz and $f_o = 5.746$ GHz are symmetric around $f_o = 5.756$ GHz and both have a resonant frequency shift toward $f_o = 5.756$ GHz with medium shifting amplitude.

8.2 Frequency shift by gate and flux

The Josephson inductance L_J is function of phase and charge or flux bias across the loop and the voltage bias on the gate port. Fig. 8.10 shows the resonant frequency modulation

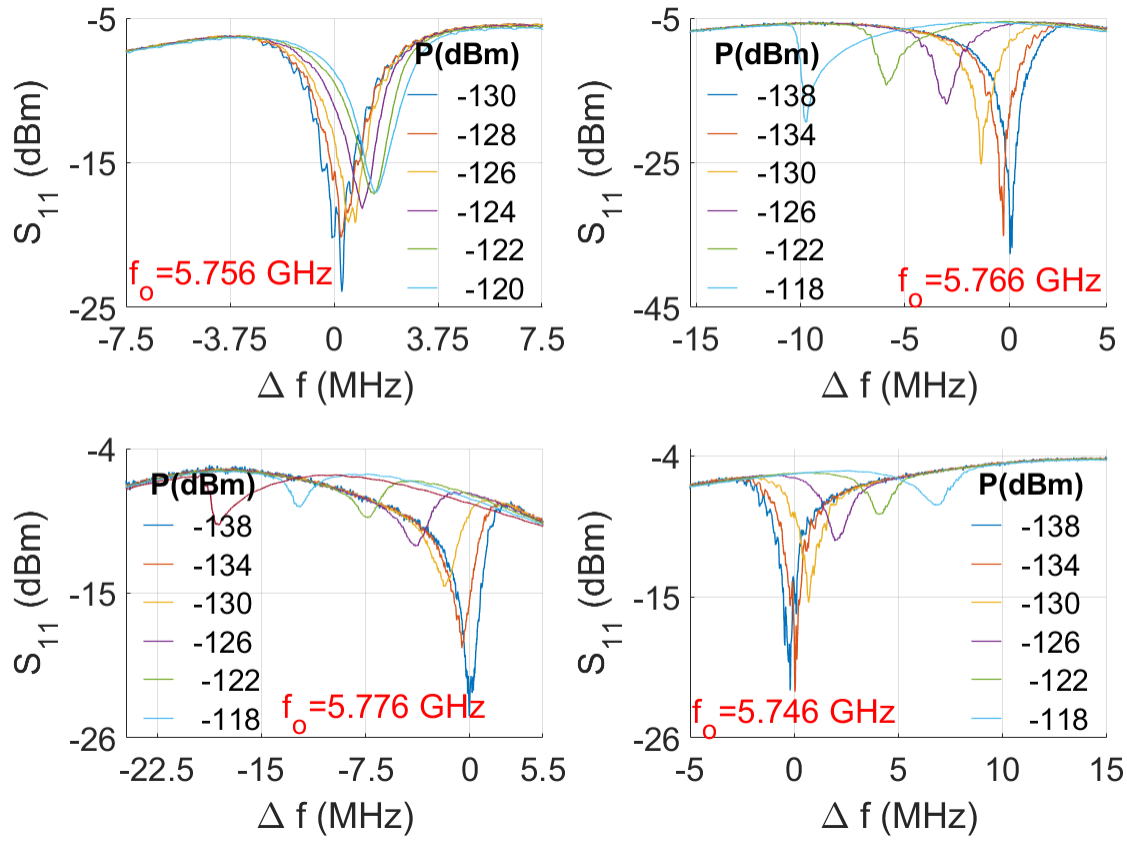

Figure 8.9: frequency shift by the NA probing power at various resonant frequency point

as function of the flux bias at three different charge states. Fig. 8.10(a) shows the middle of the Coulomb blockade regime and has a frequency shift about 50 MHz amplitude with flux. Fig. 8.10(b) is in the regime where the charge is close to the charge degeneracy point and the frequency shift has a larger amplitude of 150 MHz with flux. Fig. 8.10(c) is the resonant frequency shift right at the charge degeneracy point.The higher amplitude curve is from the Cooper pairs, while the smaller amplitude curve comes from the presence of quasiparticles. The resonant frequency shifts match very well with our theoretical prediction from the three band model of the CPT in Fig. 3.6 of Chapter (3). The amplifier peak was centered at f_o = 5.756 GHz during data collection. The lower frequency part is sharper than the higher frequency side because the SLUG amplifier has slightly higher gain on the lower frequency side than on the higher side.

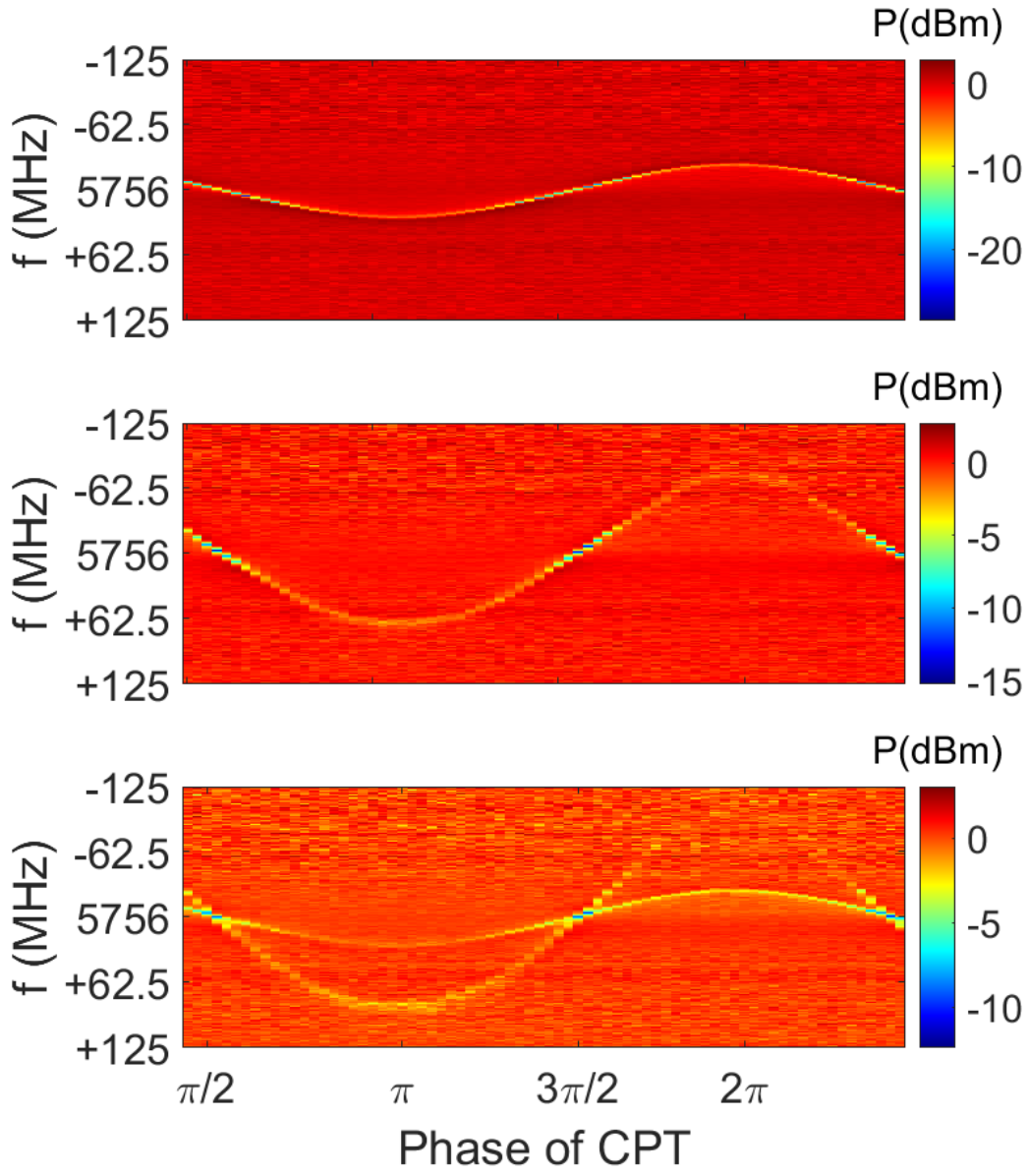

Figure 8.10: frequency shift by flux bias at three charge states

Fig. 8.11 shows the resonant frequency shift by varying the gate biasing voltage at three different phase states of the CPT. Fig. 8.11(a) corresponds to a phase $\phi \approx \pi/2$. The modulation has an overall $2e$ period plus a small amount of e-periodic modulation as indicated by short blue curves at the charge degeneracy points. Our charge detector is operated at the coulomb blockade regime which is far from the quasiparticle poisson. Fig. 8.11(b) shows the modulation at $\phi \approx 0$. Gate charge has minimum modulation of the resonant frequency

until it closely approaches the charge degeneracy point. Surprisingly, this is the regime where our charge detector has the highest charge sensitivity, when it is operated right in the middle of the coulomb blockade regime where modulation of the resonant frequency by charge is zero. Fig. 8.11(c) corresponds to phase $\phi \approx -\pi/2$ where the modulation of the resonant frequency by charge becomes maximum again. Because the inductance switched sign, the modulation by charge switches to the lower frequency side. The resonant frequency is sharper at this frequency region because the SLUG amplifier gain peak was on the lower frequency side. The resonant frequency shift pattern in the Coulomb blockade regime matches well with our theoretical simulation as in Fig. 3.8. It was less accurate near the charge degeneracy point because it was only three band model. To achieve a closer match between theoretical simulation and experimental data more charge states need to be included in the simulation.

Fig. 8.12 is a 3D plot of the resonant frequency modulation as a function of gate and flux bias. Quasiparticle poisoning occurs at the charge degeneratcy point as the frequency shift switches suddenly from a maximum to a minimum.

To facilitate interpretation of the resonant frequency shift by charge Fig. 8.13 is plot of frequency shift in the Coulomb blockade regime. The black dashed lines form the coulomb blockade region centered at $\phi = -\pi/2$ and charge equals zeros. In this region, charge gives minimum modulation of the resonant frequency shift. It gains its maximum near the charge degeneracy points, for which charge equals to -1/2 or 1/2. The big gap near charge equals to 1/2 is due to the quasiparticles.

If a cross cut is taken on the z axis at a specific frequency shift value it will trace out a 'saddle' shape as shown in Fig. 8.14(b). It is similar to the 'football' shape that occurs when a Cooper pair box is coupled to a linear superconducting resonator(33). By the slope of the sides of this saddle, relative values of E_J and E_c can be determined.

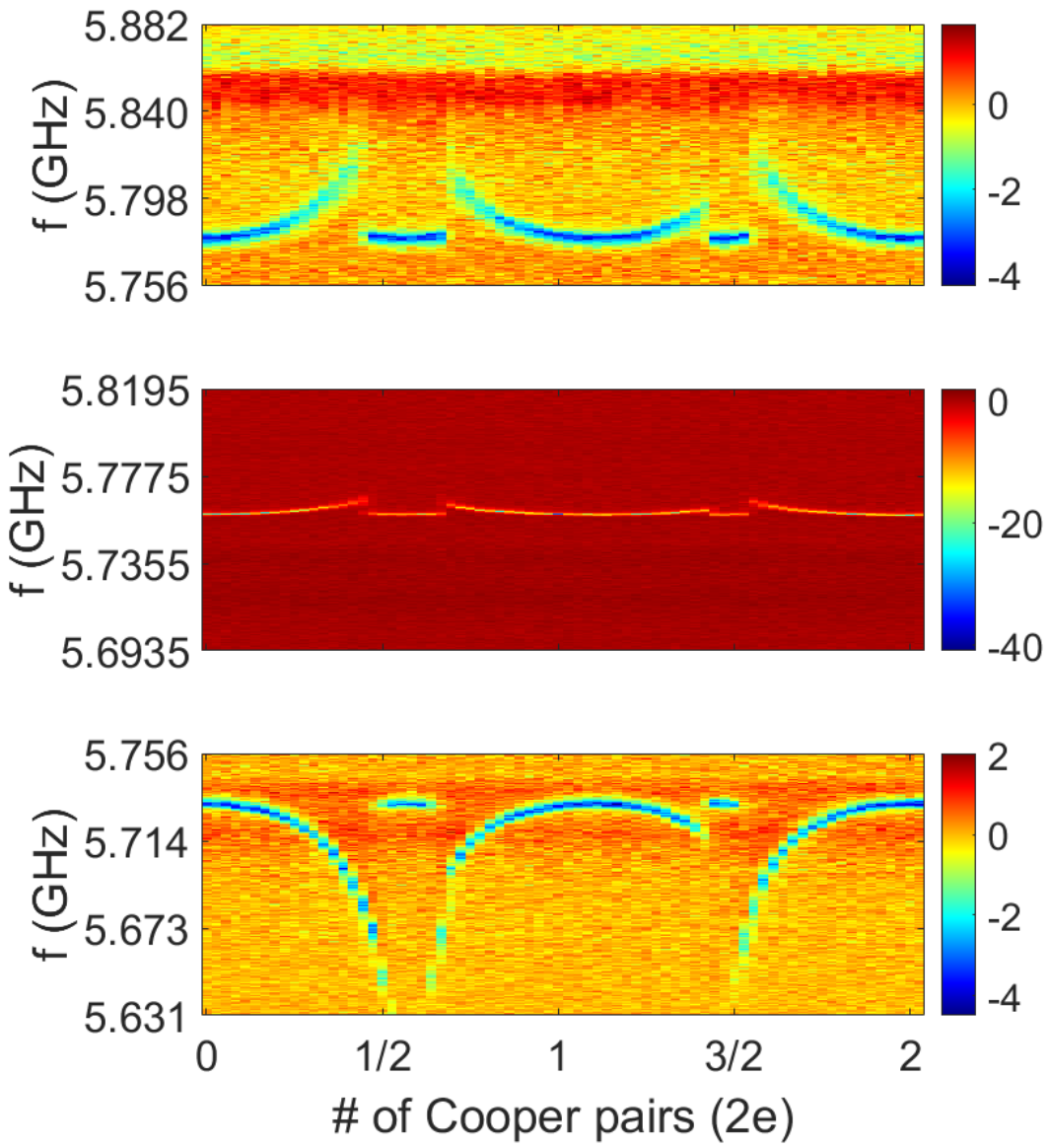

Figure 8.11: frequency shift by gate biasing at three charge states of the CPT

8.3 phase response

Fig. 8.15 shows the phase response of the charge detector at various flux and gate charges shown in the Coulomb blockade regime. Around $f_o = 5.756$ GHz, the resonator acquires negative 2π phase shift when the frequency sweep through the resonance frequency as indicated by the red zones. Away from $f_o = 5.756$ GHz, the resonator acquires positive

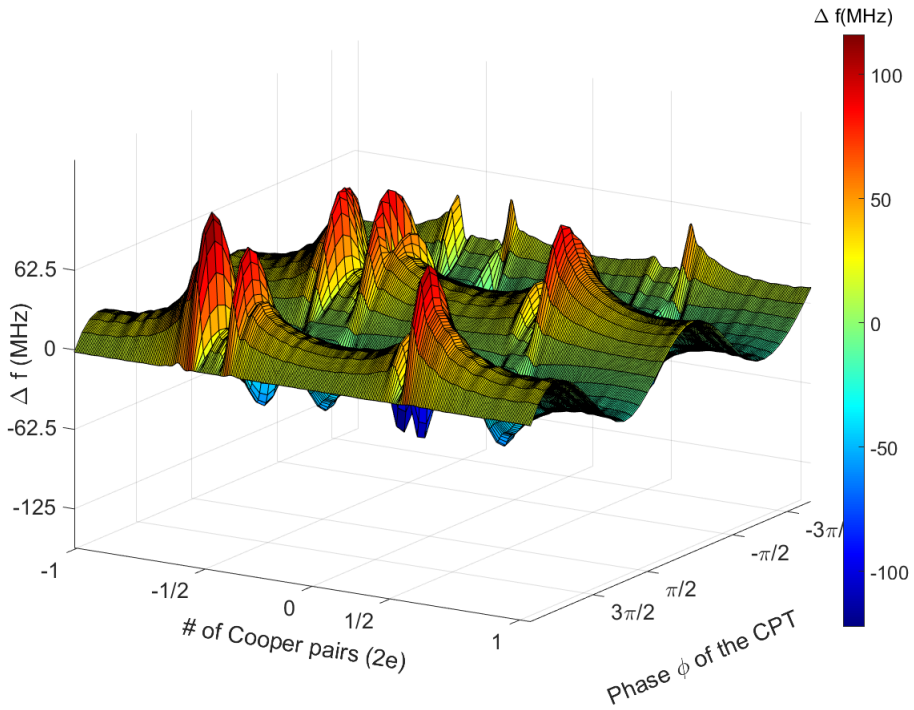

Figure 8.12: 3D plot of frequency shift by flux and gate bias

phase shift as indicated by the blue colored zone. The circle red dots are from the quasi-particle poissoning.Fig. 8.15(1) and Fig. 8.15(2) are the phase shifts of the profiles of line 1 and 2 respectively. The negative phase shift is more visible in the profile plots. At the transition point where the phase shift switches from positive to negative the resonator switches from under-coupled to over-coupled to the external environment(18). At this point the resonator could be operated as a microwave fractional differentiator (18).

Fig. 8.16 shows the phase and amplitude transition of the resonator as function of the CPT phase in the Coulomb blockade regime. From left to right the resonator went from over coupled to under coupled and back to over coupled again. At the two points where the phase shift switched from positive to negative the resonator was in critical coupling condition and the quality factor of the resonator was highest. Unintentionally we engineered a resonator with variable coupling coefficient to the environment. The sharp phase flip at the critical coupling condition could be employed to fabricate certain detectors such as microwave photon counter except for the fractional differentiator.

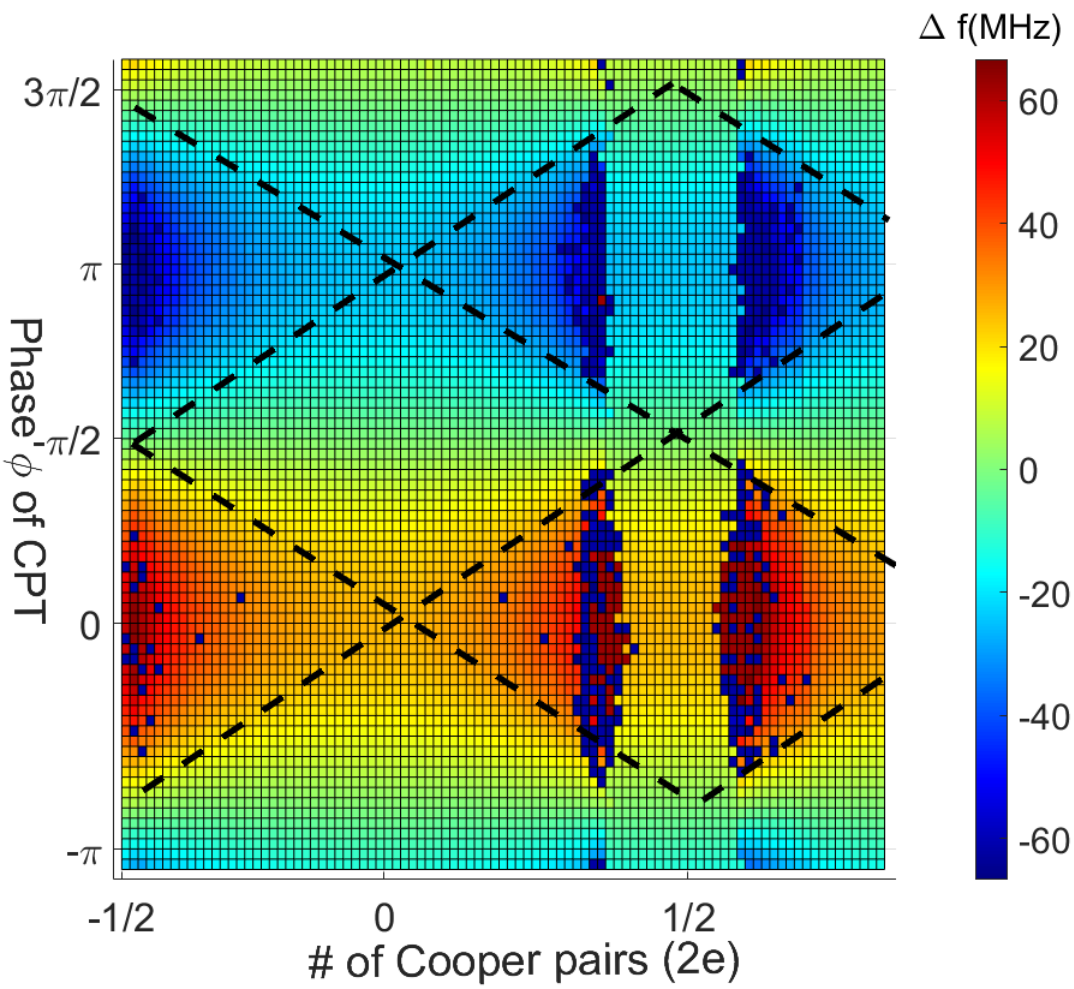

Figure 8.13: frequency shift shown in the coulomb blockade and charge degeneracy regime

For further evaluation the resonance response in amplitude, phase was simulated using our resonator parameters. The simulation result as in Fig. 8.17 are in excellent agreement with experimental result.

8.4 Emission suppression

One phenomenon we observed from our resonator is suppression of the stimulated emission from the parametric pumping by a classical signal; at the same time a new resonance was generated. Quantum tomography will be carried out to evaluate the state of the new

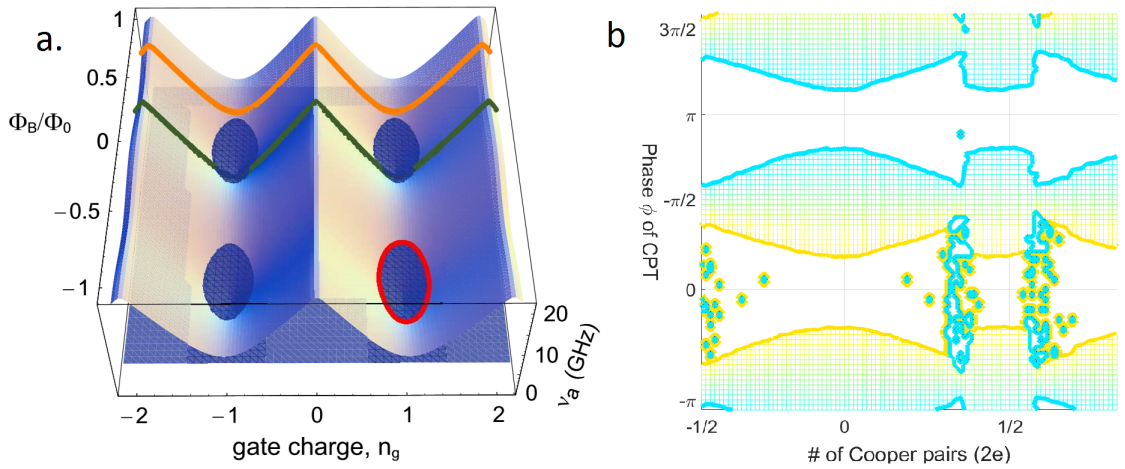

Figure 8.14: **a.)** The foot ball traced out for specific frequency shift for a CPB capacitively coupled to a linear resonator through quantum capacitance. **b.)** The saddle traced out for specific frequency shift for a CPT inductively coupled to a linear resonator. The saddle marked out with yellow color is +20 MHz resonant frequency shift and the saddle with cyan color is −20 MHz resonant frequency shift.

resonance. Stimulated emission was generated by pumping at twice the resonant frequency of $f_o = 5.756$ GHz from the flux port as shown in Fig. 8.20(a). The emission picks up intensity with increased pumping power. A single tone microwave signal 1 MHz red detuned to the emission was sent to the resonator at the input port. The resulting emission is shown in Fig. 8.20(b). When the pumping power was low the emission from this parametric pumping was totally suppressed and a new resonance was generated 1 MHz above the emission as indicated by the yellow strip. When the pumping power was high enough, the emission was not suppressed anymore and the activated resonance vanished. The suppressed stimulated emission traced out a diamond shape as outlined by the black dashed line. Due to the non-linearity of our resonator the activated resonance was unlikely to be classical microwave photon. Fig. 8.19(b) is cross cut of the emission peaks in Fig. 8.20 for six typical pumping powers or spontaneous emission power. The central peaks are spontaneous emission and peaks 1 MHz lower are the activating signal. The peaks 1 MHz to the right are the activated peaks that appear only for low emission.

When the drive signal was applied 1 MHz higher than the spontaneous emission, the addi-

tional resonance appeared 1 MHz lower than the spontaneous emission when its intensity was low. Similarly the activated emission disappear when the pumping power was high enough. Fig. 8.19(a) shows emission peaks at six different pumping powers. It is almost a mirror image of Fig. 8.19(b) since the activating signal was on the opposite side of the main resonance.

8.5 'Normal mode splitting'

When the flux port was pumped with MHz signal, we observed an effect similar to the normal mode splitting that researchers have observed when a mechanical resonator is parametrically coupled to a microwave resonator (36) (31). Separation of the side bands increased up to 15 MHz with higher modulation power instead of remaining as constant. Multiple side bands emerged when the modulating frequency switched to 10 MHz suggesting that it is not amplitude modulation. For simply frequency modulation as in the case of charge detection the frequency separation for the side bands was same as the modulation frequency. Further evaluation will be carried out to quantify this phenomena.

8.6 Charge Sensitivity Characterization

8.6.1 Carrier plus Stimulated emission

One way we perform charge detection is to combine a carrier wave from external source with internal stimulated emission from parametric pumping. Fig. 8.21 shows the charge modulation of such a combined signal. The gate and flux biasing are $n_g \approx 0.9$, $\phi_{dc} \approx 0.68\pi$. The charge on the gate is modulated with amplitude of $\delta n_g = 7 \times 10^{-3}$ and frequency $f_m =$ 1.5 MHz. The external carrier signal provides cavity photons $n_c \approx 15$ and the pumping power for the stimulated emission peak is $P_{pump} \approx -66$ dBm. The calculated charge

sensitivity $\delta q = 2.1 \times 10^{-7} e/\sqrt{Hz}$. The total number of photons in the cavity is $n_{tot} \approx 300$, which is 1000 times fewer than RF-SET (32).

8.6.2 Maximum sensitivity spot

Fig. 8.22 shows the charge modulation of carrier signal at $f_o = 5.756$ GHz. The carrier was generated externally and no stimulated emission applied. The gate and flux biasing are $n_g \approx 0$, the center of the Coulomb blockade and $\phi_{dc} \approx \pi$. The charge on the gate is modulated with amplitude of $\delta n_g = 3.5 \times 10^{-2}$ and frequency $f_m = 2.7$ MHz. This result is surprising since the frequency shift $\partial f/\partial n_g$ is zero based on Fig. 8.13. Clearly some other (as yet to be understood) phenomena is causing the response to the modulation. To retrieve this critical parameter we borrow the $\partial f/\partial n_g$ from Fig. 8.21. As has shown by Equation (6.10 and 6.32), the reflected signal for the two cases differ mainly by $\partial f/\partial n_g$ value. The $\partial s/\partial f$ term difference are small since the frequency variation between the two points are small.

Fig. 8.23 shows simulated side bands with Bessel function and the input parameter is $\frac{1}{\omega_g}\frac{d\omega}{dn_g}\frac{C_g V_o}{e}$ as in Eq. (6.10) and (6.32) Fig. 8.23(a) corresponds to the maximum sensitivity spot and the input parameter is 0.03, while (b) corresponds to side bands of Figure (8.21) and the input parameter is 0.0001. Discrepancy in carrier power level and noise floor for the two scenarios as indicated by Figure (8.4) has been taken into consideration. So $\partial f/\partial n_g$ for Figure (8.22) are 0.03/0.00001 = 3000 the corresponding charge sensitivity $\delta q \approx 2.1 \times 10^{-7}/3000 = 7 \times 10^{-11} e/\sqrt{Hz}$.

8.7 Noise Measurement

The sensitivity of our charge detector could potentially be limited by the gain and noise level of our amplifier chain, predominately by the noise level of our 1^{st} stage SLUG ampli-

fier which has typical noise temperature of 1 Kelvin and gain of 15dB.(17) The HEMT and room temperature amplifiers have 46 dB and 43 dB gain respectively so the total gain in our system is 94 dB, mincing about 10 dB loss in the coax cable. To characterize the gain and noise we carried out a Y factor measurement by measuring the power spectra coming from two 50 Ω resistors anchored at 4 K and 35 mK temperature stage separately.(4) Left part in Fig. 7.1 illustrates our setup for Y-factor measurement in our dilution refrigerator. There was 7 dBm loss in the coax cable connecting the 4K temperature resistor to the sample which has been corrected for in the calculation. The noise power at the output of the amplifier chain is given as

$$P_{out} = Gk_B(T_R + T_{amp})BW \tag{8.1}$$

where G is the gain of the amplifier chain. T_R is the temperature of the two resistors, T_{amp} is the noise temperature of the amplifier chain and BW is the resolution band width of the spectrum analyzer. The slope after linear fit to the two data points is the gain and the x intercept is the negative value of the amplifier noise temperature. At 35 mK the quantum effects are significant and can be correct for using the equation(27): (27)

$$\eta(f) = \frac{hf/k_BT}{e^{hf/k_BT} - 1} \tag{8.2}$$

Fig. 8.24 is linear fit to the two temperature data points. The measured gain is 95.8 dB noise temperature of 95 mK. The measured noise temperature is significantly lower than we expected. One major reason is that the SLUG gain is very sensitive to its flux and current bias values. During normal measurements we could see the SLUG gain profile from our network analyzer. However during the Y-factor measurement the input port to the sample has to be switched to the noise sources and we lose direct observation of the SLUG gain profile. By sending the network analyzer output to the flux port of our sample we could regain partial view of the SLUG gain profile since the flux modulation line has a

much narrower band width than the SLUG. There could also be errors with 35 mK noise measurement part because the noise power was much lower and the S/N ratio was smaller. Finally due to a relatively low He level in He bath, it is possible that the nominally 4 K measurement was actually at a higher temperature, which could also surpass the apparent noise temperature. These preliminary results do indicate that the Y-factor measurements should eventually be effective for characterizing our amplifier chain.

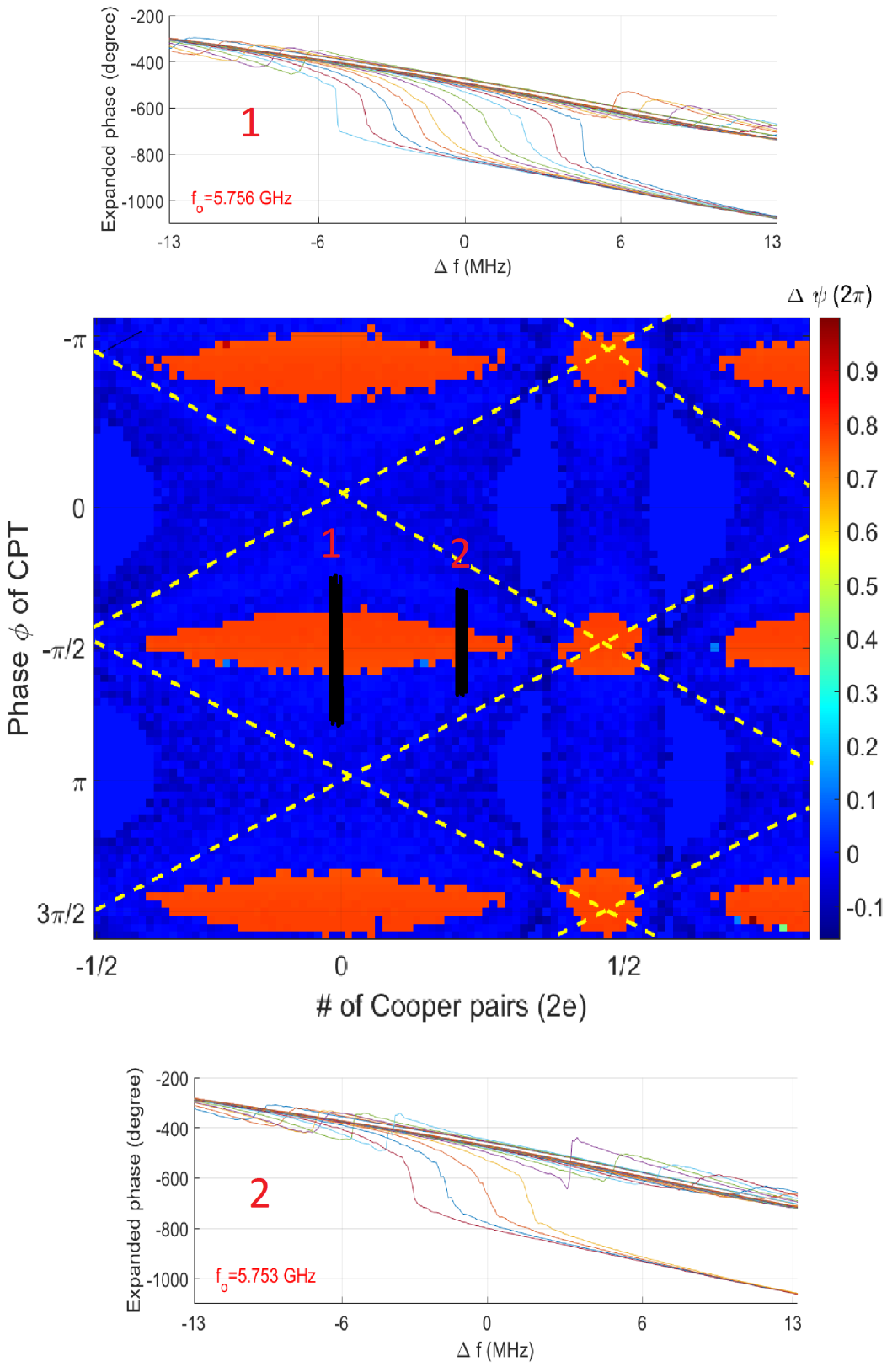

Figure 8.15: Phase shift of the resonator for various flux and charge biasing. The phase data was recorded as expanded phase.

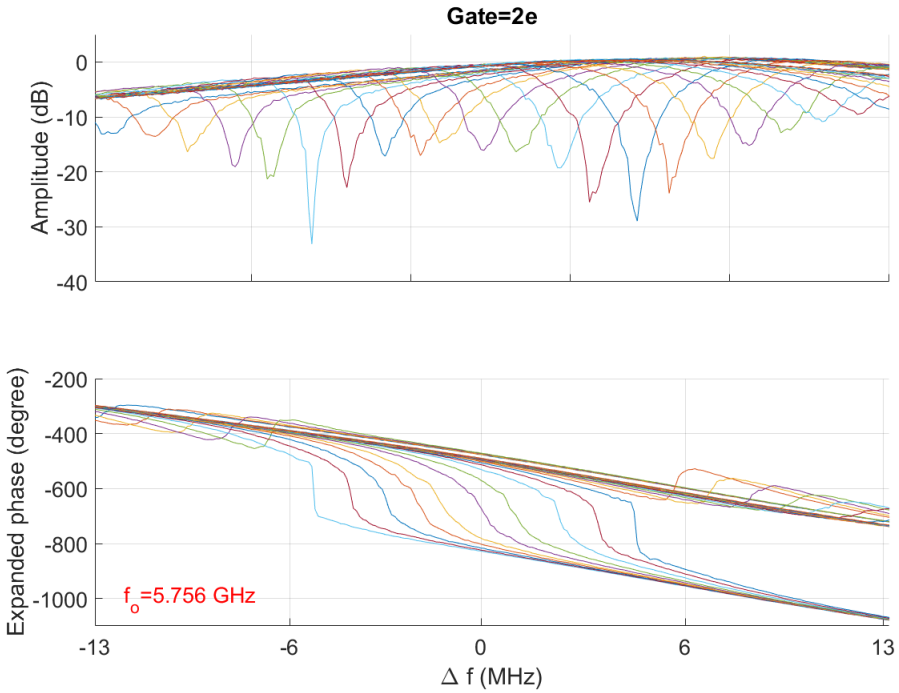

Figure 8.16: Phase shift and amplitude at various phase of CPT.

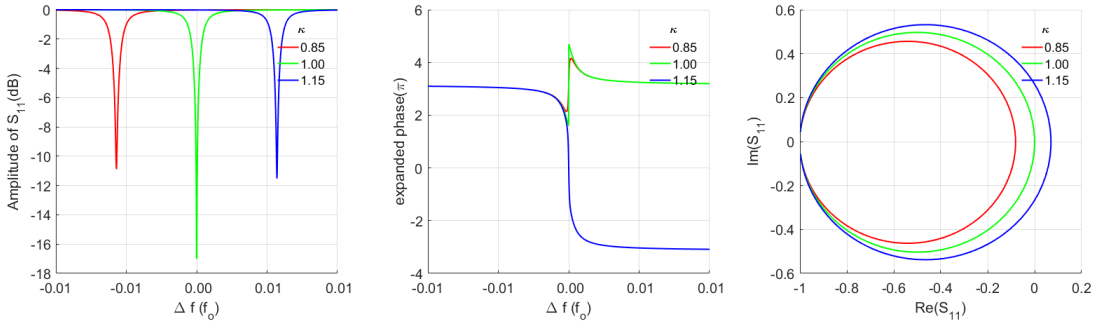

Figure 8.17: Reflection amplitude, phase change when the resonator went through critical coupling transition. The 3^{rd} polar plot shows that the circumference of the resonance circle will cross over the origin and sits right on the origin at critical coupling condition. The amplitudes of the three different coupling regime have been shifted to show the change in the resonance amplitude.

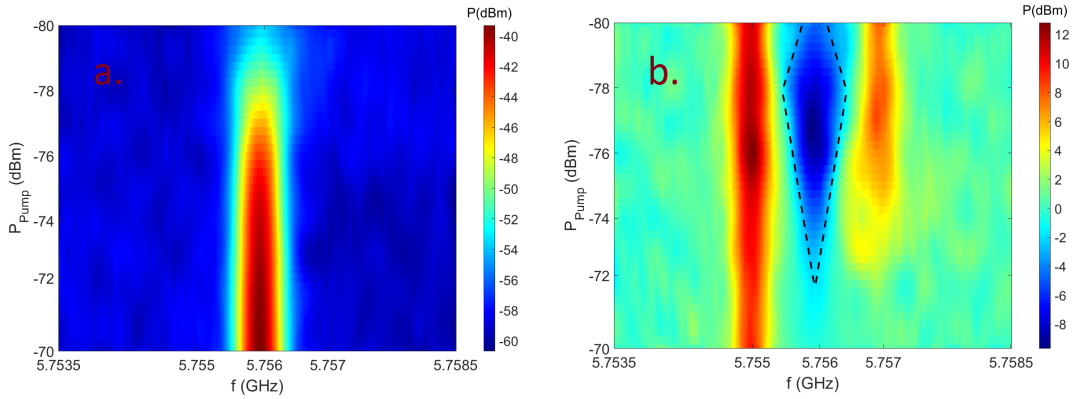

Figure 8.18: The amplitudes of the three different coupling regime have been shifted to show the change in the resonance amplitude.

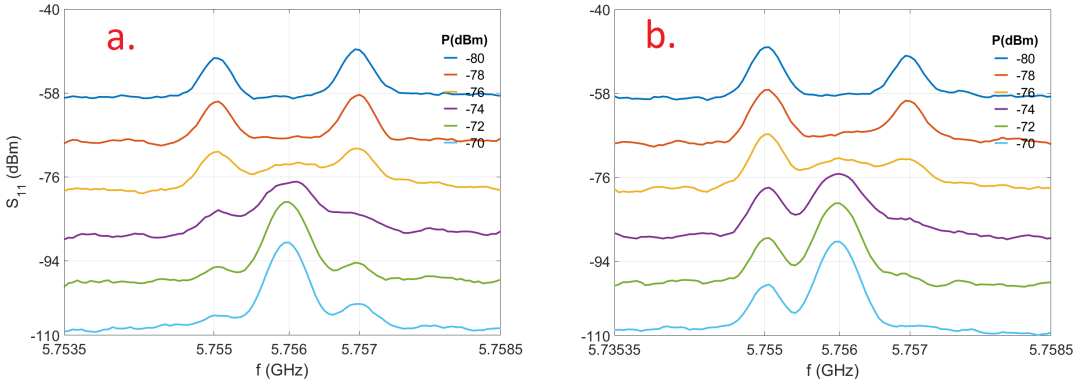

Figure 8.19: Activated emission by activating signal and stimulated emission.

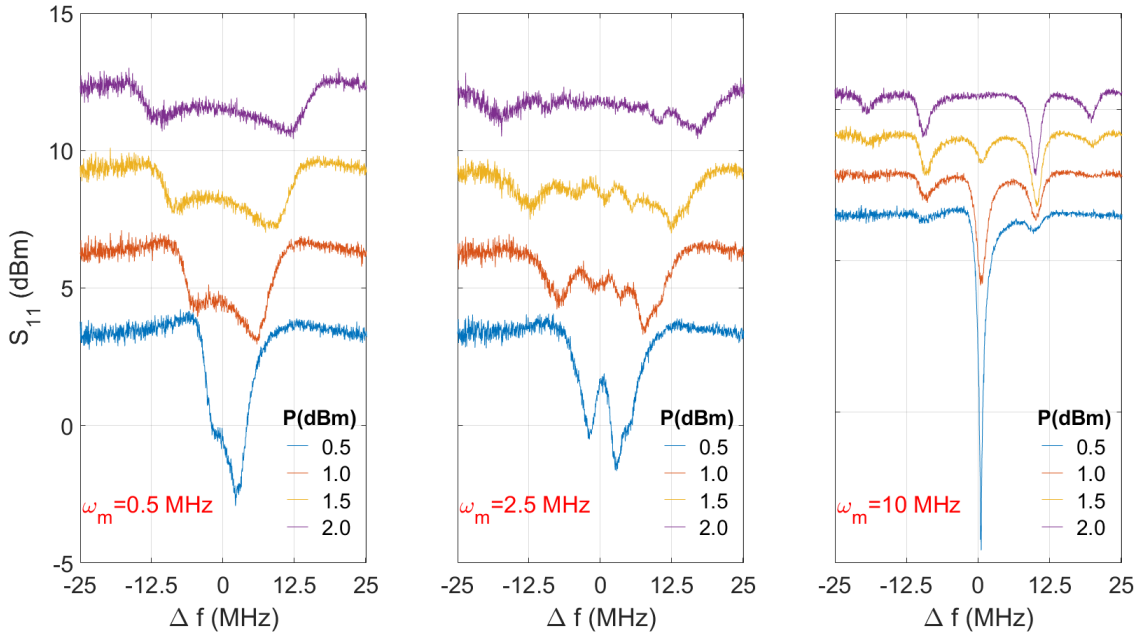

Figure 8.20: The amplitudes of the three different coupling regime have been shifted to show the change in the resonance amplitude.

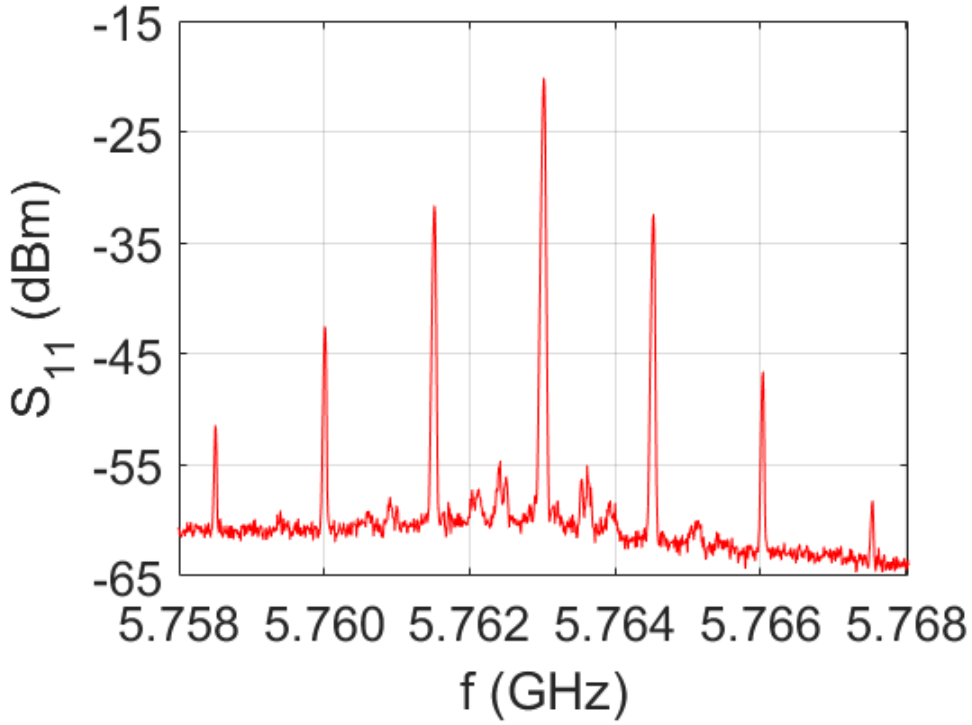

Figure 8.21: Side bands by charge modulation on the gate

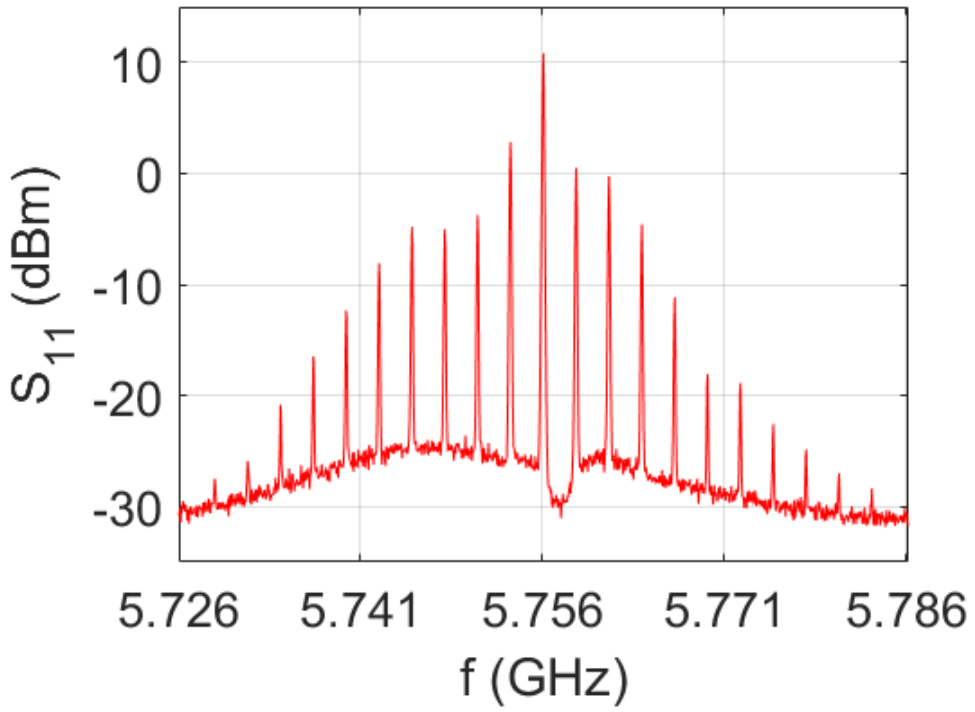

Figure 8.22: Side bands by charge modulation on the gate at maximum charge sensitivity

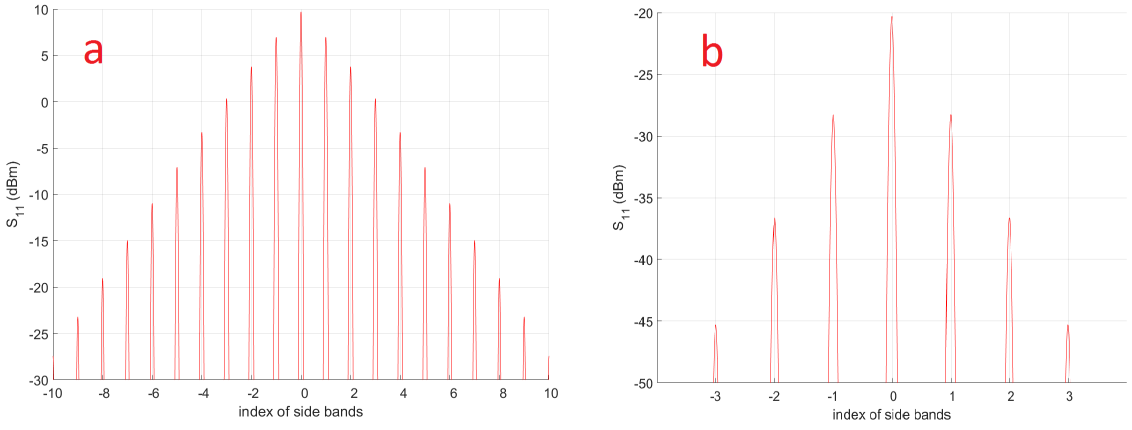

Figure 8.23: Simulated side bands by charge modulation on the gate

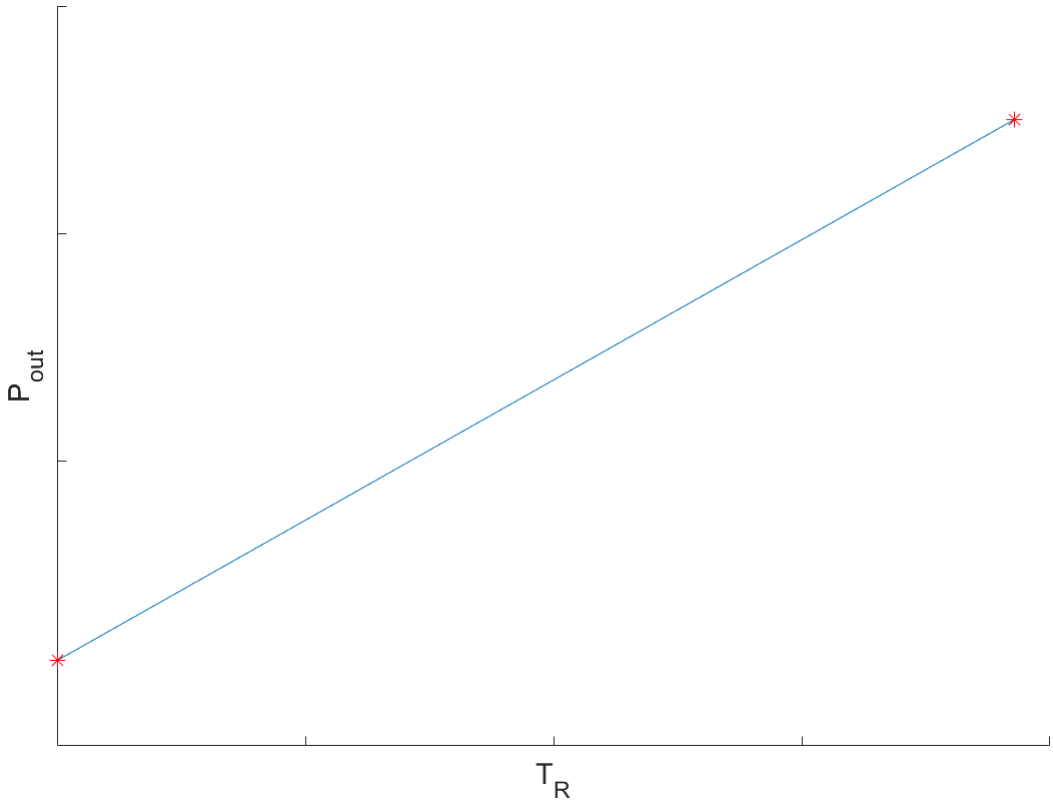

Figure 8.24: Illustration of Y-factor measurement

Chapter 9

CONCLUSION AND FUTURE WORK

We have discovered a new ultra high sensitivity scheme for dispersive measurement. With this high charge sensitivity it can be used for single shot qubit state readout. It also has high photon phonon coupling coefficient that can be applied for ultra-strong photon phonon coupling at single photon level; it can also be operated as a JPA with 20 dB gain and 10 MHz bandwidth.

9.1 frequency shift quantification

Frequency shift per charge $\partial f/\partial n_g$ could be characterized at the rotating frame. when the gate modulating signal and the output signal is displayed as XY display on a oscilloscope, the equivalent x is proportional to the gate modulation signal and the frequency of the oscillating signal is proportional to $\partial f/\partial n_g$.

9.2 quantum state tomography

State of the stimulated emission from parametric pumping on the flux and gate port as well as the accompanied emission from the suppressed spontaneous emission effect need to be characterized with quantum state tomography. Similar techniques have been carried out in previous project for state reconstruction of microwave lasing.(5)

9.3 squeezing

A squeezed state with noise lower than the standard quantum limit in one quadrature and higher in the orthogonal quadrature has been proved to improve the noise performance for measurements of mechanical motion. (6) Using the intrinsic parametric amplification of the cCPT could also improve the charge sensitivity of our charge detector in one quadrature.

9.4 magnetometer

The resonant frequency of the nonlinear resonator is shifted by both charge and flux modulation. Since It works as charge detector when charge on the gate is varied, it could similarly be operated as magnetometer when the flux on the flux port is varied.

Appendix A

Q FACTOR MEASUREMENT

This appendix presents the method that I have used to retrieve the resonance parameters Q_L, Q_o and ω_o from the reflection data of our microwave resonator.

This appendix presents the method that I have used to retrieve the resonance parameters Q_L, Q_o and ω_o from the reflection data of our microwave resonator.

A.1 model of reflection measurement

For reflective type measurement, the reflected signal measured by the network analyzer is: (34),(21)

$$\Gamma_i = ae^{-2\pi j f \tau}\Gamma_d\left[\frac{1-\kappa+j2Q_o\delta_i - jX_eR_o/(Z_o^2+X_e^2)}{1+\kappa+j2Q_o\delta_i - jX_eR_o/(Z_o^2+X_e^2)}\right] \tag{A.1}$$

$$= ae^{-2\pi j f \tau}\Gamma_d\left[\frac{1-\kappa+j2Q_o\delta_L}{1+\kappa+j2Q_o\delta_L}\right] \tag{A.2}$$

$$= ae^{-2\pi j f \tau}\Gamma_d\left[1-\frac{2\kappa}{1+\kappa+j2Q_o\delta_L}\right] \tag{A.3}$$

with the shifted resonance frequency

$$\delta_L = \delta_i - \frac{X_e R_o}{2Q_{o(}Z_o^2 + X_e^2)} \tag{A.4}$$

$$Q_L = \frac{Q_o}{1+\kappa} \tag{A.5}$$

Here Γ_d is the detuned reflection coefficient away from resonance, which rotates the resonance circle in the polar plot.

$$\Gamma_d = \left(\frac{jX_e - Z_o}{jX_e + Z_o}\right) = e^{-2j\ \mathrm{atan}(X_e/Z_o)} \tag{A.6}$$

and κ is the coupling coefficient defined as

$$Q_L = \frac{Q_o}{1+\kappa} \tag{A.7}$$

Finally, τ is the electrical delay, and a is a complex constant accounting for the gain and phase shift due to other parts of the measurement system.
The resonance traces out a circle when plotted in a polar format as shown in Fig. (A.1)

A.2 fitting procedures

A.2.1 Removing cable delay

The cable delay was indicated as a sloped phase away from the resonance point as shown in Fig.(A.2). The cable delay is exactly equal to the slope and can be retrieved by linear fit to the line segment either before or after the resonance. The two slopes from either side of the resonance are usually not the same due to other non-linear effect in the microwave line. The best result is taking the average or linear fit to the whole line if the resonance

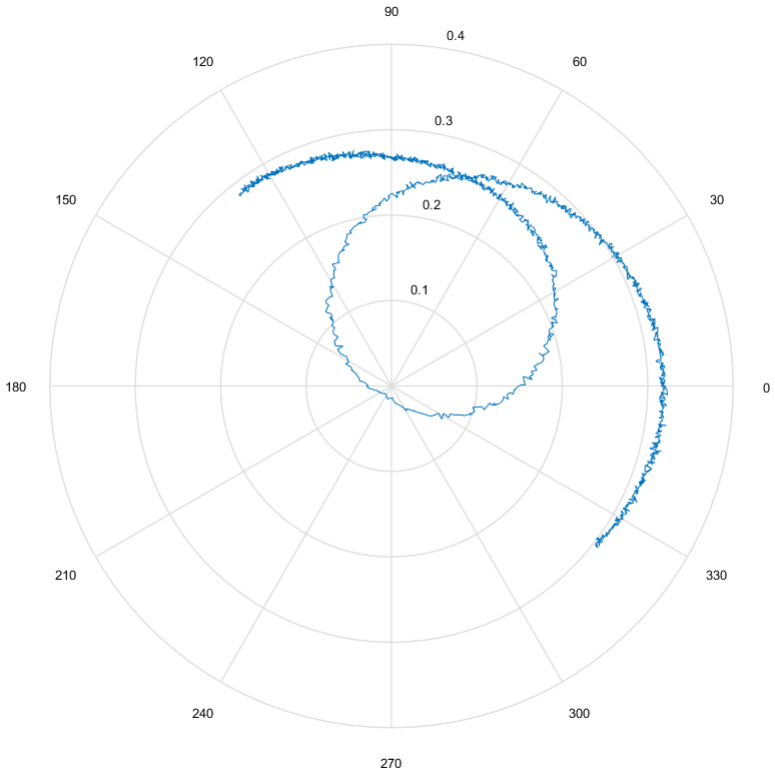

Figure A.1: frequency sweep response of the resonator in polar format. The resonator traced out a circle around the resonance frequency f_o

point is tunable. The discrepancy could be less significant for a high Q resonator since a narrower frequency span could be applied which cuts off other effects.

After correcting the cable delay, the phase away from the resonance point will be flat and the cross curves on either side of the resonance frequency in polar display will shrink to a semicircle as dispicted in Fig. (A.4), Fig. (A.3) shows the correction effect on the phase after cable delay correction.

A.2.2 Circle fit

The resonance circle is left with a rotation angle θ_d away from the real axis due to the coupling reactance X_e as shown in Eq. A.8. By Equation A.6. The resonance circle will

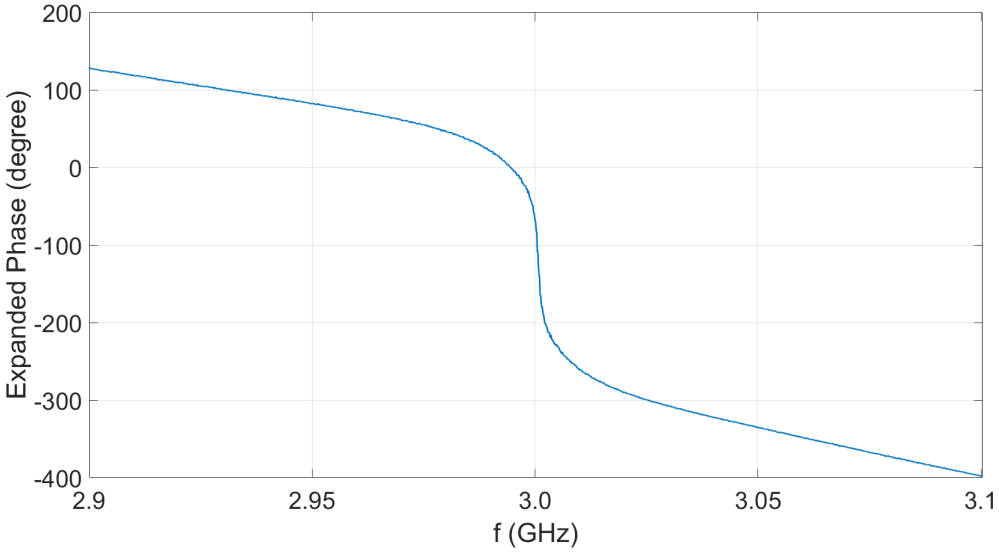

Figure A.2: Phase response around the resonance point. The sloped phase away from the resonance point indicates the cable delay and can be used to correct the cable delay after a linear fit

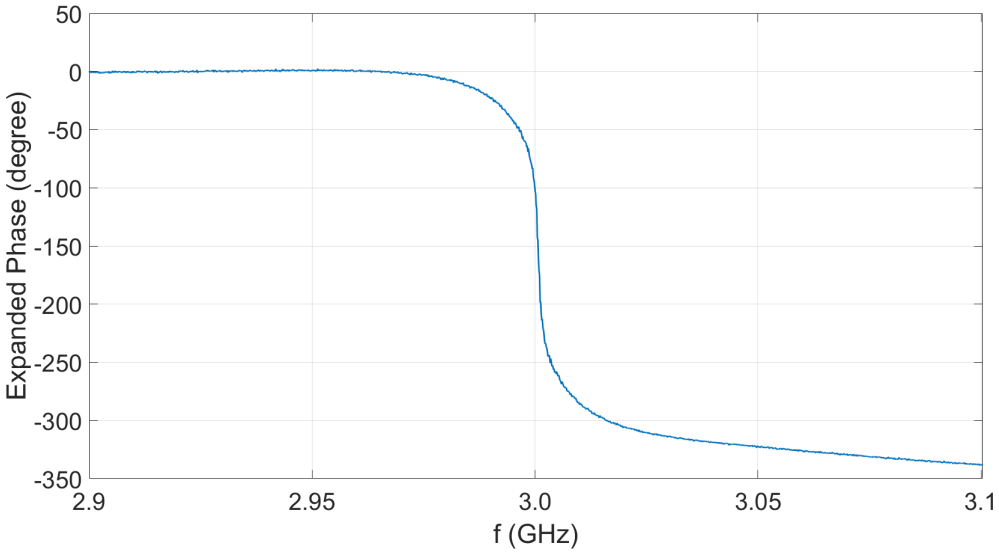

Figure A.3: After correcting the cable delay the phase away from the resonance point become a flat line.

be rotated further away from the real axis and shrink at the same time as the coupling reactance increases. Fig. (A.5) is a modeled resonance circle with different coupling reactances. Eq. A.9 shows that the diameter of the circle is determined by the coupling coefficient κ.

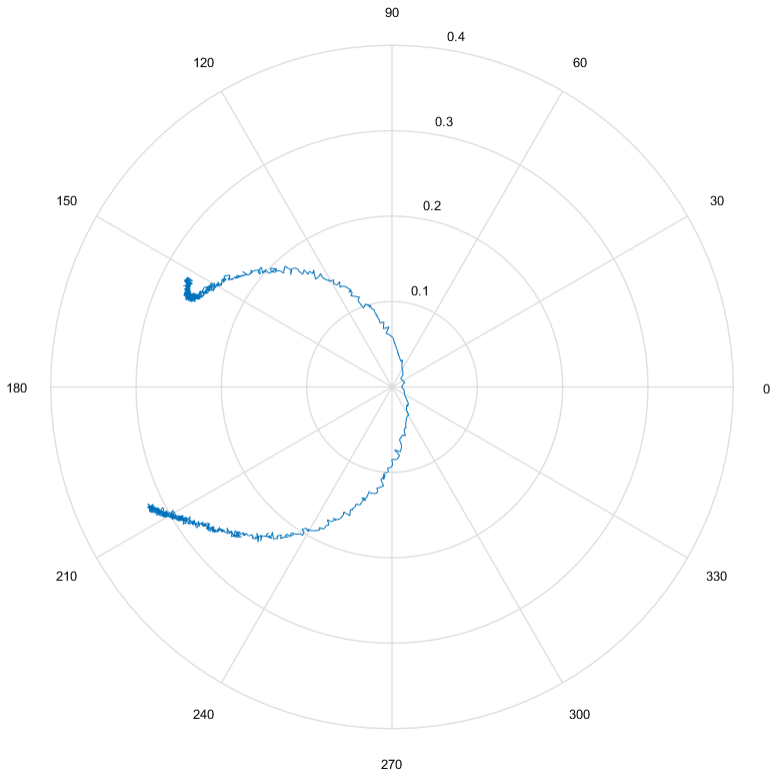

Figure A.4: After correcting the cable delay, the two cross over curves away from the resonance shrink to minimize size

$$\theta_d = -2\text{atan}(X_e/Z_o) \tag{A.8}$$

$$d = \frac{2\kappa}{1+\kappa} \tag{A.9}$$

Fig. A.6 shows that a circle is fitted to the curve and the coupling reactance X_e which comes from the coupling capacitor for our case and the coupling coefficient κ is retrieved. The fitted circle center (C_x, C_y) and radius R are given by

$$\theta_d = \text{atan}\left(\frac{C_y}{C_x}\right) \tag{A.10}$$

$$d = R \tag{A.11}$$

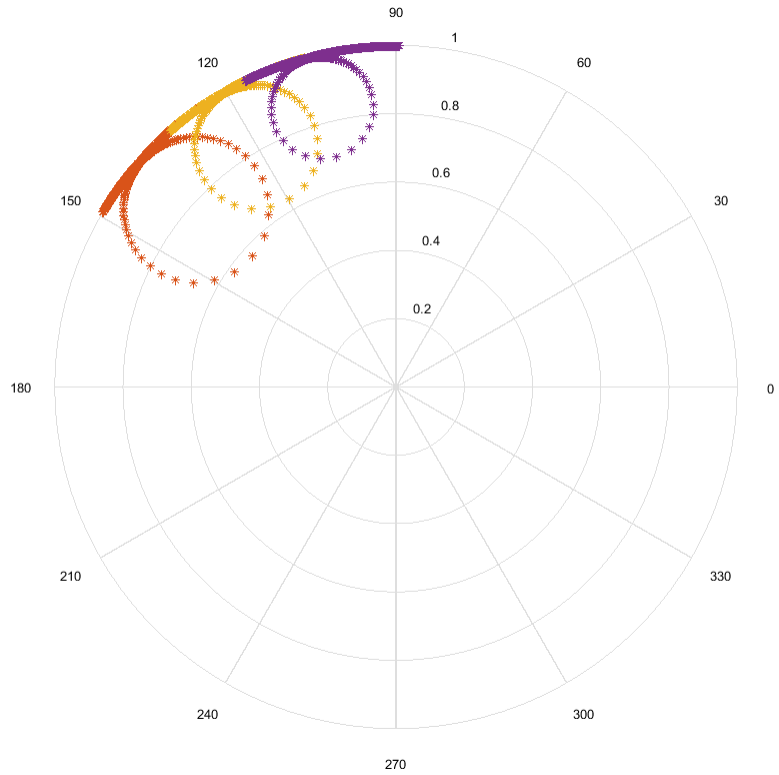

Figure A.5: resonance circles with various coupling reactance. With larger coupling reactance the cirlce rotats further away from the real axis and shrink to a smaller diameter at the same time.

Also

$$\tan\psi_L = -2Q_L\delta_L \tag{A.12}$$

A.2.3 translation to the origin

Eq. A.14 can be rewritten as

$$\Gamma_i = ae^{-2\pi jf\tau}\Gamma_d\left[1-\frac{2\kappa}{1+\kappa+j2Q_o\delta_L}\right] \tag{A.13}$$

$$= ae^{-2\pi jf\tau}\Gamma_d\left[1-\frac{\frac{2\kappa}{1+\kappa}}{1+j2Q_L\delta_L}\right] \tag{A.14}$$

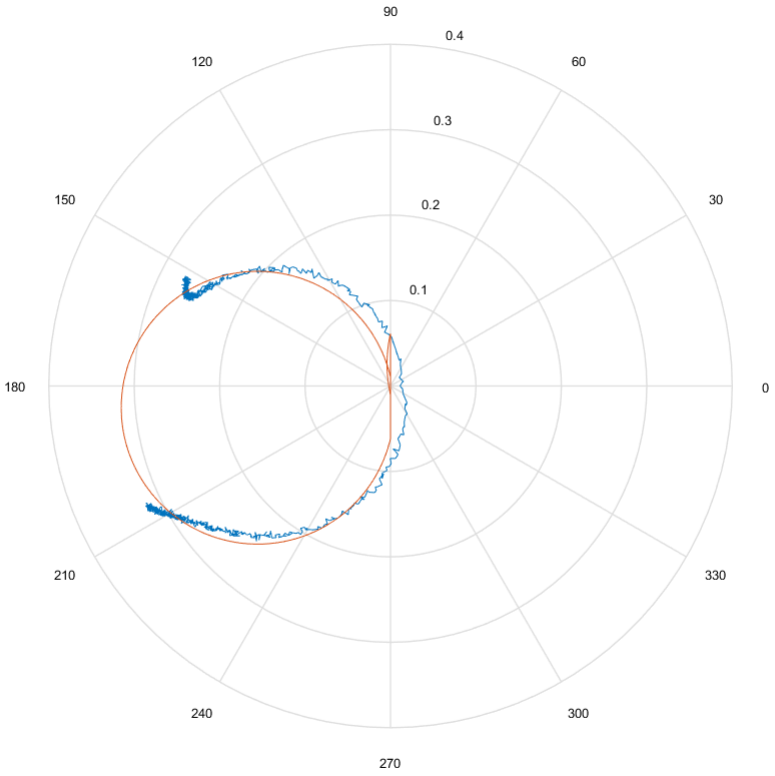

Figure A.6: Resonance circles with various coupling reactances. With larger coupling reactance the cirlce rotats further away from the real axis and shrinks to a smaller diameter at the same time.

After translation to the origin, the reflection coefficient becomes

$$\Gamma_i = -\frac{\frac{2\kappa}{1+\kappa}}{1+j2Q_L\delta_L} \tag{A.15}$$

which traces out a circle with diameter and phase

$$d = \frac{2\kappa}{1+\kappa} \tag{A.16}$$

$$\tan\phi = -2Q_L\delta_L \tag{A.17}$$

When one selects two frequencies f_3 and f_4 where $\psi_L = \pm 45°$, Q_L can be found as(21)

$$Q_L = \frac{f_L}{f_3 - f_4} \tag{A.18}$$

The reflection model A.14 ignores the coupling loss. When coupling loss present the circle will be distorted and

$$\tan\phi \approx -2Q_L\delta_L \tag{A.19}$$

Least square regression can be used to retrieve Q_L with higher accuracy.(34) The quantity to be minimized is

$$E = \sum_i^N \left[\tan\theta_i + \frac{2Q_L}{f_o}(f_i - f_L)\right]^2 \tag{A.20}$$

$$= \sum_i^N \left[y_i - (mx_i + c)\right]^2 \tag{A.21}$$

and

$$Q_L = \frac{c}{2} \tag{A.22}$$

Appendix B

4^{TH} ORDER CALCULATION

1. plus term.

$$
\begin{aligned}
& (\hat{a}_j + \hat{a}_j^\dagger)^4 \\
= \; & (\hat{a}_j + \hat{a}_j^\dagger)^2 (\hat{a}_j + \hat{a}_j^\dagger)^2 \\
= \; & (a_j^{\dagger 2} + a_j^2 + a_j^\dagger a_j + a_j a_j^\dagger)(a_j^{\dagger 2} + a_j^2 + a_j^\dagger a_j + a_j a_j^\dagger) \\
= \; & (a_j^{\dagger 2} + a_j^2 + 2a_j^\dagger a_j + 1)(a_j^{\dagger 2} + a_j^2 + 2a_j^\dagger a_j + 1) \\
= \; & a_j^{\dagger 2} a_j^{\dagger 2} + a_j^\dagger a_j^\dagger a_j a_j + 2a_j^{\dagger 2} a_j^\dagger a_j + 2a_j^{\dagger 2} \\
& + a_j a_j a_j^\dagger a_j^\dagger + a_j^2 a_j^2 + 2a_j^2 a_j^\dagger a_j + 2a_j^2 \\
& + 2a_j^\dagger a_j a_j^{\dagger 2} + 2a_j^\dagger a_j a_j^2 + 4a_j^\dagger a_j a_j^\dagger a_j + 4a_j^\dagger a_j + 1 \\
= \; & a_j^{\dagger 2} a_j^{\dagger 2} + a_j^\dagger (a_j a_j^\dagger - 1) a_j + 2a_j^{\dagger 2} a_j^\dagger a_j + 2a_j^{\dagger 2} \\
& + a_j (a_j^\dagger a_j + 1) a_j^\dagger + a_j^2 a_j^2 + 2a_j^2 a_j^\dagger a_j + 2a_j^2 \\
& + 2a_j^\dagger a_j a_j^{\dagger 2} + 2a_j^\dagger a_j a_j^2 + 4a_j^\dagger a_j a_j^\dagger a_j + 4a_j^\dagger a_j + 1 \\
= \; & a_j^{\dagger 2} a_j^{\dagger 2} + a_j^\dagger a_j a_j^\dagger a_j - a_j^\dagger a_j + 2a_j^{\dagger 2} a_j^\dagger a_j + 2a_j^{\dagger 2} \\
& + a_j a_j^\dagger a_j a_j^\dagger + a_j a_j^\dagger + a_j^2 a_j^2 + 2a_j^2 a_j^\dagger a_j + 2a_j^2 \\
& + 2a_j^\dagger a_j a_j^{\dagger 2} + 2a_j^\dagger a_j a_j^2 + 4a_j^\dagger a_j a_j^\dagger a_j + 4a_j^\dagger a_j + 1 \\
= \; & a_j^{\dagger 2} a_j^{\dagger 2} + a_j^\dagger a_j a_j^\dagger a_j - a_j^\dagger a_j + 2a_j^{\dagger 2} a_j^\dagger a_j + 2a_j^{\dagger 2} \\
& + (a_j^\dagger a_j + 1)(a_j^\dagger a_j + 1) + (a_j^\dagger a_j + 1) + a_j^2 a_j^2 + 2a_j^2 a_j^\dagger a_j + 2a_j^2
\end{aligned}
$$

$$
\begin{aligned}
& (\hat{a}_j + \hat{a}_j^\dagger)^2 (\hat{a}_k + \hat{a}_k^\dagger)^2 \\
= \; & (a_j^{\dagger 2} + a_j^2 + a_j^\dagger a_j + a_j a_j^\dagger)(a_k^{\dagger 2} + a_k^2 + a_k^\dagger a_k + a_k a_k^\dagger) \\
= \; & (a_j^{\dagger 2} + a_j^2 + 2a_j^\dagger a_j + 1)(a_k^{\dagger 2} + a_k^2 + 2a_k^\dagger a_k + 1) \\
= \; & a_j^{\dagger 2} a_k^{\dagger 2} + a_j^\dagger a_j^\dagger a_k a_k + 2a_j^{\dagger 2} a_k^\dagger a_k + a_j^{\dagger 2} \\
& + a_j a_j a_k^\dagger a_k^\dagger + a_j^2 a_k^2 + 2a_j^2 a_k^\dagger a_k + a_j^2 \\
& + 2a_j^\dagger a_j a_k^{\dagger 2} + 2a_j^\dagger a_j a_k^2 + 4a_j^\dagger a_j a_k^\dagger a_k + 2a_j^\dagger a_j \\
& + a_k^{\dagger 2} + a_k^2 + 2a_k^\dagger a_k + 1 \\
= \; & 4a_j^\dagger a_j a_k^\dagger a_k + 2a_j^\dagger a_j + 2a_k^\dagger a_k + 1 \\
& + a_j^{\dagger 2} a_k^{\dagger 2} + a_j^\dagger a_j^\dagger a_k a_k + 2a_j^{\dagger 2} a_k^\dagger a_k + a_j^{\dagger 2} \\
& + a_j a_j a_k^\dagger a_k^\dagger + a_j^2 a_k^2 + 2a_j^2 a_k^\dagger a_k + a_j^2 \\
& + 2a_j^\dagger a_j a_k^{\dagger 2} + 2a_j^\dagger a_j a_k^2 + a_k^{\dagger 2} + a_k^2 +
\end{aligned}
\tag{B.1}
$$

$$
\begin{aligned}
& (\hat{a}_j + \hat{a}_j^\dagger)^3 (\hat{a}_k + \hat{a}_k^\dagger) \\
= \; & (a_j^{\dagger 2} + a_j^2 + a_j^\dagger a_j + a_j a_j^\dagger)(\hat{a}_j + \hat{a}_j^\dagger)(\hat{a}_k + \hat{a}_k^\dagger) \\
= \; & (a_j^{\dagger 2} + a_j^2 + a_j^\dagger a_j + a_j a_j^\dagger)(a_j a_k + a_j a_k^\dagger + a_j^\dagger a_k + a_j^\dagger a_k^\dagger) \\
= \; & a_j^{\dagger 2} a_j a_k + a_j^{\dagger 2} a_j a_k^\dagger + a_j^{\dagger 2} a_j^\dagger a_k + a_j^{\dagger 2} a_j^\dagger a_k^\dagger \\
& + a_j^2 a_j a_k + a_j^2 a_j a_k^\dagger + a_j^2 a_j^\dagger a_k + a_j^2 a_j^\dagger a_k^\dagger \\
& + a_j^\dagger a_j a_j a_k + a_j^\dagger a_j a_j a_k^\dagger + a_j^\dagger a_j a_j^\dagger a_k + a_j^\dagger a_j a_j^\dagger a_k^\dagger \\
& + a_j a_j^\dagger a_j a_k + a_j a_j^\dagger a_j a_k^\dagger + a_j a_j^\dagger a_j^\dagger a_k + a_j a_j^\dagger a_j^\dagger a_k^\dagger \\
= \; & a_j^\dagger (a_j a_j^\dagger - 1) a_k + a_j^{\dagger 2} a_j a_k^\dagger + a_j^{\dagger 2} a_j^\dagger a_k + a_j^{\dagger 2} a_j^\dagger a_k^\dagger \\
& + a_j^2 a_j a_k + a_j^2 a_j a_k^\dagger + a_j^2 a_j^\dagger a_k + a_j (a_j^\dagger a_j + 1) a_k^\dagger \\
& + a_j^\dagger a_j a_j a_k + a_j^\dagger a_j a_j a_k^\dagger + a_j^\dagger a_j a_j^\dagger a_k + a_j^\dagger a_j a_j^\dagger a_k^\dagger \\
& + a_j a_j^\dagger a_j a_k + (1 + a_j^\dagger a_j) a_j a_k^\dagger + (1 + a_j^\dagger a_j) a_j^\dagger a_k + a_j a_j^\dagger a_j^\dagger a_k^\dagger \\
= \; & a_j^\dagger a_j a_j^\dagger a_k - a_j^\dagger a_k + a_j^{\dagger 2} a_j a_k^\dagger + a_j^{\dagger 2} a_j^\dagger a_k + a_j^{\dagger 2} a_j^\dagger a_k^\dagger \\
& + a_j^2 a_j a_k + a_j^2 a_j a_k^\dagger + a_j^2 a_j^\dagger a_k + a_j a_j^\dagger a_j a_k^\dagger + a_j a_k^\dagger \\
& + a_j^\dagger a_j a_j a_k + a_j^\dagger a_j a_j a_k^\dagger + a_j^\dagger a_j a_j^\dagger a_k + a_j^\dagger a_j a_j^\dagger a_k^\dagger \\
& + a_j a_j^\dagger a_j a_k + a_j a_k^\dagger + a_j^\dagger a_j a_j a_k^\dagger + a_j^\dagger a_k + a_j^\dagger a_j a_j^\dagger a_k + a_j a_j^\dagger a_j^\dagger a_k^\dagger \\
= \; & a_j^\dagger a_j a_j^\dagger a_k - a_j^\dagger a_k + a_j^{\dagger 2} a_k^\dagger a_j + a_j^{\dagger 2} a_j^\dagger a_k + a_j^{\dagger 2} a_j^\dagger a_k^\dagger \\
& + a_j^2 a_j a_k + a_j^2 a_j a_k^\dagger + a_j^2 a_j^\dagger a_k + (a_j^\dagger a_j + 1) a_k^\dagger a_j + a_k^\dagger a_j \\
& + a_j^\dagger a_j a_j a_k + a_j^\dagger a_j a_k^\dagger a_j + a_j^\dagger a_j a_j^\dagger a_k + a_j^\dagger a_j a_j^\dagger a_k^\dagger \\
& + a_j a_j^\dagger a_j a_k + a_k^\dagger a_j + a_j^\dagger a_j a_k^\dagger a_j + a_j^\dagger a_k + a_j^\dagger a_j a_j^\dagger a_k + a_j a_j^\dagger a_j^\dagger a_k^\dagger \\
= \; & a_j^\dagger a_j a_j^\dagger a_k - a_j^\dagger a_k + a_j^{\dagger 2} a_k^\dagger a_j + a_j^{\dagger 2} a_j^\dagger a_k + a_j^{\dagger 2} a_j^\dagger a_k^\dagger \\
& + a_j^2 a_j a_k + a_j^2 a_j a_k^\dagger + a_j^2 a_j^\dagger a_k + a_j^\dagger a_j a_k^\dagger a_j + a_k^\dagger a_j + a_k^\dagger a_j \\
& + a_j^\dagger a_j a_j a_k + a_j^\dagger a_j a_k^\dagger a_j + a_j^\dagger a_j a_j^\dagger a_k + a_j^\dagger a_j a_j^\dagger a_k^\dagger \\
& + a_j a_j^\dagger a_j a_k + a_k^\dagger a_j + a_j^\dagger a_j a_k^\dagger a_j + a_j^\dagger a_k + a_j^\dagger a_j a_j^\dagger a_k + a_j a_j^\dagger a_j^\dagger a_k^\dagger \\
= \; & (3 a_j^\dagger a_j)(a_j^\dagger a_k + a_k^\dagger a_j) + 3 a_j^\dagger a_k \\
& + a_j^{\dagger 2} a_k^\dagger a_j + a_j^{\dagger 2} a_j^\dagger a_k + a_j^{\dagger 2} a_j^\dagger a_k^\dagger \\
& + a_j^2 a_j a_k + a_j^2 a_j a_k^\dagger + a_j^2 a_j^\dagger a_k + a_j^\dagger a_j a_k^\dagger a_j + a_k^\dagger a_j + a_k^\dagger a_j \\
& + a_j^\dagger a_j a_j a_k + a_j^\dagger a_j a_k^\dagger a_j + a_j^\dagger a_j a_j^\dagger a_k + a_j^\dagger a_j a_j^\dagger a_k^\dagger \\
& + a_j a_j^\dagger a_j a_k + a_k^\dagger a_j + a_j^\dagger a_j a_k^\dagger a_j + a_j^\dagger a_k + a_j^\dagger a_j a_j^\dagger a_k + a_j a_j^\dagger a_j^\dagger a_k^\dagger
\end{aligned}
$$

$$
\begin{aligned}
& (\hat{a}_j + \hat{a}_j^\dagger)^2 (\hat{a}_k + \hat{a}_k^\dagger)(\hat{a}_l + \hat{a}_l^\dagger) \\
= \; & (a_j^{\dagger 2} + a_j^2 + a_j^\dagger a_j + a_j a_j^\dagger)(\hat{a}_k + \hat{a}_k^\dagger)(\hat{a}_l + \hat{a}_l^\dagger) \\
= \; & (a_j^{\dagger 2} + a_j^2 + a_j^\dagger a_j + a_j a_j^\dagger)(a_k a_l + a_k a_l^\dagger + a_k^\dagger a_l + a_k^\dagger a_l^\dagger) \\
= \; & a_j^{\dagger 2} a_k a_l + a_j^{\dagger 2} a_k a_l^\dagger + a_j^{\dagger 2} a_k^\dagger a_l + a_j^{\dagger 2} a_k^\dagger a_l^\dagger \\
& + a_j^2 a_k a_l + a_j^2 a_k a_l^\dagger + a_j^2 a_k^\dagger a_l + a_j^2 a_k^\dagger a_l^\dagger \\
& + a_j^\dagger a_j a_k a_l + a_j^\dagger a_j a_k a_l^\dagger + a_j^\dagger a_j a_k^\dagger a_l + a_j^\dagger a_j a_k^\dagger a_l^\dagger \\
& + a_j a_j^\dagger a_k a_l + a_j a_j^\dagger a_k a_l^\dagger + a_j a_j^\dagger a_k^\dagger a_l + a_j a_j^\dagger a_k^\dagger a_l^\dagger \\
= \; & a_j^{\dagger 2} a_k a_l + a_j^{\dagger 2} a_k a_l^\dagger + a_j^{\dagger 2} a_k^\dagger a_l + a_j^{\dagger 2} a_k^\dagger a_l^\dagger \\
& + a_j^2 a_k a_l + a_j^2 a_k a_l^\dagger + a_j^2 a_k^\dagger a_l + a_j^2 a_k^\dagger a_l^\dagger \\
& + a_j^\dagger a_j a_k a_l + a_j^\dagger a_j a_k a_l^\dagger + a_j^\dagger a_j a_k^\dagger a_l + a_j^\dagger a_j a_k^\dagger a_l^\dagger \\
& + a_j a_j^\dagger a_k a_l + (a_j^\dagger a_j + 1) a_k a_l^\dagger + (a_j^\dagger a_j + 1) a_k^\dagger a_l + a_j a_j^\dagger a_k^\dagger a_l^\dagger \\
= \; & (2 a_j^\dagger a_j + 1)(a_k a_l^\dagger + a_k^\dagger a_l) \\
& + a_j^{\dagger 2} a_k a_l + a_j^{\dagger 2} a_k a_l^\dagger + a_j^{\dagger 2} a_k^\dagger a_l + a_j^{\dagger 2} a_k^\dagger a_l^\dagger \\
& + a_j^2 a_k a_l + a_j^2 a_k a_l^\dagger + a_j^2 a_k^\dagger a_l + a_j^2 a_k^\dagger a_l^\dagger \\
& + a_j^\dagger a_j a_k a_l + a_j^\dagger a_j a_k^\dagger a_l^\dagger + a_j a_j^\dagger a_k a_l + a_j a_j^\dagger a_k^\dagger a_l^\dagger
\end{aligned}
\tag{B.3}
$$

2. minus term

$$
\begin{aligned}
& (\hat{a}_j - \hat{a}_j^\dagger)^4 \\
= \; & (\hat{a}_j - \hat{a}_j^\dagger)^2 (\hat{a}_j - \hat{a}_j^\dagger)^2 \\
= \; & (a_j^{\dagger 2} + a_j^2 - a_j^\dagger a_j - a_j a_j^\dagger)(a_j^{\dagger 2} + a_j^2 - a_j^\dagger a_j - a_j a_j^\dagger) \\
= \; & (a_j^{\dagger 2} + a_j^2 - 2a_j^\dagger a_j - 1)(a_j^{\dagger 2} + a_j^2 - 2a_j^\dagger a_j - 1) \\
= \; & a_j^{\dagger 2} a_j^{\dagger 2} + a_j^\dagger a_j^\dagger a_j a_j - 2a_j^{\dagger 2} a_j^\dagger a_j - a_j^{\dagger 2} \\
& + a_j a_j a_j^\dagger a_j^\dagger + a_j^2 a_j^2 - 2a_j^2 a_j^\dagger a_j - a_j^2 \\
& - 2a_j^\dagger a_j a_j^{\dagger 2} - 2a_j^\dagger a_j a_j^2 + 4a_j^\dagger a_j a_j^\dagger a_j + 2a_j^\dagger a_j \\
& - a_j^{\dagger 2} - a_j^2 + 2a_j^\dagger a_j + 1 \\
= \; & a_j^{\dagger 2} a_j^{\dagger 2} + a_j^\dagger (a_j a_j^\dagger - 1) a_j - 2a_j^{\dagger 2} a_j^\dagger a_j - a_j^{\dagger 2} \\
& + a_j (a_j^\dagger a_j + 1) a_j^\dagger + a_j^2 a_j^2 - 2a_j^2 a_j^\dagger a_j - a_j^2 \\
& - 2a_j^\dagger a_j a_j^{\dagger 2} - 2a_j^\dagger a_j a_j^2 + 4a_j^\dagger a_j a_j^\dagger a_j + 2a_j^\dagger a_j \\
& - a_j^{\dagger 2} - a_j^2 + 2a_j^\dagger a_j + 1 \\
= \; & a_j^{\dagger 2} a_j^{\dagger 2} + a_j^\dagger a_j a_j^\dagger a_j - a_j^\dagger a_j - 2a_j^{\dagger 2} a_j^\dagger a_j - a_j^{\dagger 2} \\
& + a_j a_j^\dagger a_j a_j^\dagger + a_j a_j^\dagger + a_j^2 a_j^2 - 2a_j^2 a_j^\dagger a_j - a_j^2 \\
& - 2a_j^\dagger a_j a_j^{\dagger 2} - 2a_j^\dagger a_j a_j^2 + 4a_j^\dagger a_j a_j^\dagger a_j + 2a_j^\dagger a_j \\
& - a_j^{\dagger 2} - a_j^2 + 2a_j^\dagger a_j + 1 \\
= \; & a_j^{\dagger 2} a_j^{\dagger 2} + a_j^\dagger a_j a_j^\dagger a_j - a_j^\dagger a_j - 2a_j^{\dagger 2} a_j^\dagger a_j - a_j^{\dagger 2} \\
& + (a_j^\dagger a_j + 1)(a_j^\dagger a_j + 1) + (a_j^\dagger a_j + 1) + a_j^2 a_j^2 - 2a_j^2 a_j^\dagger a_j - a_j^2 \\
& - 2a_j^\dagger a_j a_j^{\dagger 2} - 2a_j^\dagger a_j a_j^2 + 4a_j^\dagger a_j a_j^\dagger a_j + 2a_j^\dagger a_j \\
& - a_j^{\dagger 2} - a_j^2 + 2a_j^\dagger a_j + 1 \\
= \; & a_j^{\dagger 2} a_j^{\dagger 2} + a_j^\dagger a_j a_j^\dagger a_j - a_j^\dagger a_j - 2a_j^{\dagger 2} a_j^\dagger a_j - a_j^{\dagger 2} \\
& + a_j^\dagger a_j a_j^\dagger a_j + 2a_j^\dagger a_j + 1 + (a_j^\dagger a_j + 1) + a_j^2 a_j^2 - 2a_j^2 a_j^\dagger a_j - a_j^2 \\
& - 2a_j^\dagger a_j a_j^{\dagger 2} - 2a_j^\dagger a_j a_j^2 + 4a_j^\dagger a_j a_j^\dagger a_j + 2a_j^\dagger a_j \\
& - a_j^{\dagger 2} - a_j^2 + 2a_j^\dagger a_j + 1 \qquad 108 \\
= \; & 6a_j^\dagger a_j a_j^\dagger a_j + 6a_j^\dagger a_j + 3 \\
& - a_j^{\dagger 2} a_j^{\dagger 2} - \frac{3}{2} a_j^{\dagger 2} - \frac{3}{2} a_j^2 + a_j^\dagger a_j - \frac{1}{2}
\end{aligned}
$$

$$
\begin{aligned}
& (\hat{a}_j - \hat{a}_j^\dagger)^2 (\hat{a}_k - \hat{a}_k^\dagger)^2 \\
= \; & (a_j^{\dagger 2} + a_j^2 - a_j^\dagger a_j - a_j a_j^\dagger)(a_k^{\dagger 2} + a_k^2 - a_k^\dagger a_k - a_k a_k^\dagger) \\
= \; & (a_j^{\dagger 2} + a_j^2 - 2a_j^\dagger a_j - 1)(a_k^{\dagger 2} + a_k^2 - 2a_k^\dagger a_k - 1) \\
= \; & a_j^{\dagger 2} a_k^{\dagger 2} + a_j^\dagger a_j^\dagger a_k a_k - 2a_j^{\dagger 2} a_k^\dagger a_k - a_j^{\dagger 2} \\
& + a_j a_j a_k^\dagger a_k^\dagger + a_j^2 a_k^2 - 2a_j^2 a_k^\dagger a_k - a_j^2 \\
& - 2a_j^\dagger a_j a_k^{\dagger 2} - 2a_j^\dagger a_j a_k^2 + 4a_j^\dagger a_j a_k^\dagger a_k + 2a_j^\dagger a_j \\
& - a_k^{\dagger 2} - a_k^2 + 2a_k^\dagger a_k + 1 \\
= \; & 4a_j^\dagger a_j a_k^\dagger a_k + 2a_j^\dagger a_j + 2a_k^\dagger a_k + 1 \\
& + a_j^{\dagger 2} a_k^{\dagger 2} + a_j^\dagger a_j^\dagger a_k a_k - 2a_j^{\dagger 2} a_k^\dagger a_k - a_j^{\dagger 2} \\
& + a_j a_j a_k^\dagger a_k^\dagger + a_j^2 a_k^2 - 2a_j^2 a_k^\dagger a_k - a_j^2 \\
& - 2a_j^\dagger a_j a_k^{\dagger 2} - 2a_j^\dagger a_j a_k^2 - a_k^{\dagger 2} - a_k^2
\end{aligned}
\tag{B.4}
$$

$$
\begin{aligned}
& (\hat{a}_j - \hat{a}_j^\dagger)^3 (\hat{a}_k - \hat{a}_k^\dagger) \\
= \; & (a_j^{\dagger 2} + a_j^2 - a_j^\dagger a_j - a_j a_j^\dagger)(\hat{a}_j - \hat{a}_j^\dagger)(\hat{a}_k - \hat{a}_k^\dagger) \\
= \; & (a_j^{\dagger 2} + a_j^2 - a_j^\dagger a_j - a_j a_j^\dagger)(a_j a_k - a_j a_k^\dagger - a_j^\dagger a_k + a_j^\dagger a_k^\dagger) \\
= \; & a_j^{\dagger 2} a_j a_k - a_j^{\dagger 2} a_j a_k^\dagger - a_j^{\dagger 2} a_j^\dagger a_k + a_j^{\dagger 2} a_j^\dagger a_k^\dagger \\
& + a_j^2 a_j a_k - a_j^2 a_j a_k^\dagger - a_j^2 a_j^\dagger a_k + a_j^2 a_j^\dagger a_k^\dagger \\
& - a_j^\dagger a_j a_j a_k + a_j^\dagger a_j a_j a_k^\dagger + a_j^\dagger a_j a_j^\dagger a_k - a_j^\dagger a_j a_j^\dagger a_k^\dagger \\
& - a_j a_j^\dagger a_j a_k + a_j a_j^\dagger a_j a_k^\dagger + a_j a_j^\dagger a_j^\dagger a_k - a_j a_j^\dagger a_j^\dagger a_k^\dagger \\
= \; & a_j^\dagger (a_j a_j^\dagger - 1) a_k - a_j^{\dagger 2} a_j a_k^\dagger - a_j^{\dagger 2} a_j^\dagger a_k + a_j^{\dagger 2} a_j^\dagger a_k^\dagger \\
& + a_j^2 a_j a_k - a_j^2 a_j a_k^\dagger - a_j^2 a_j^\dagger a_k + a_j (a_j^\dagger a_j + 1) a_k^\dagger \\
& - a_j^\dagger a_j a_j a_k + a_j^\dagger a_j a_j a_k^\dagger + a_j^\dagger a_j a_j^\dagger a_k - a_j^\dagger a_j a_j^\dagger a_k^\dagger \\
& - a_j a_j^\dagger a_j a_k + (1 + a_j^\dagger a_j) a_j a_k^\dagger + (1 + a_j^\dagger a_j) a_j^\dagger a_k - a_j a_j^\dagger a_j^\dagger a_k^\dagger \\
= \; & a_j^\dagger a_j a_j^\dagger a_k - a_j^\dagger a_k - a_j^{\dagger 2} a_j a_k^\dagger - a_j^{\dagger 2} a_j^\dagger a_k + a_j^{\dagger 2} a_j^\dagger a_k^\dagger \\
& + a_j^2 a_j a_k - a_j^2 a_j a_k^\dagger - a_j^2 a_j^\dagger a_k + a_j a_j^\dagger a_j a_k^\dagger + a_j a_k^\dagger \\
& - a_j^\dagger a_j a_j a_k + a_j^\dagger a_j a_j a_k^\dagger + a_j^\dagger a_j a_j^\dagger a_k - a_j^\dagger a_j a_j^\dagger a_k^\dagger \\
& - a_j a_j^\dagger a_j a_k + a_j a_k^\dagger + a_j^\dagger a_j a_j a_k^\dagger + a_j^\dagger a_k + a_j^\dagger a_j a_j^\dagger a_k - a_j a_j^\dagger a_j^\dagger a_k^\dagger \\
= \; & a_j^\dagger a_j a_j^\dagger a_k - a_j^\dagger a_k - a_j^{\dagger 2} a_k^\dagger a_j - a_j^{\dagger 2} a_j^\dagger a_k + a_j^{\dagger 2} a_j^\dagger a_k^\dagger \\
& + a_j^2 a_j a_k - a_j^2 a_j a_k^\dagger - a_j^2 a_j^\dagger a_k + (a_j^\dagger a_j + 1) a_k^\dagger a_j + a_k^\dagger a_j \\
& - a_j^\dagger a_j a_j a_k + a_j^\dagger a_j a_k^\dagger a_j + a_j^\dagger a_j a_j^\dagger a_k - a_j^\dagger a_j a_j^\dagger a_k^\dagger \\
& - a_j a_j^\dagger a_j a_k + a_k^\dagger a_j + a_j^\dagger a_j a_k^\dagger a_j + a_j^\dagger a_k + a_j^\dagger a_j a_j^\dagger a_k - a_j a_j^\dagger a_j^\dagger a_k^\dagger \\
= \; & a_j^\dagger a_j a_j^\dagger a_k - a_j^\dagger a_k - a_j^{\dagger 2} a_k^\dagger a_j - a_j^{\dagger 2} a_j^\dagger a_k + a_j^{\dagger 2} a_j^\dagger a_k^\dagger \\
& + a_j^2 a_j a_k - a_j^2 a_j a_k^\dagger - a_j^2 a_j^\dagger a_k + a_j^\dagger a_j a_k^\dagger a_j + a_k^\dagger a_j + a_k^\dagger a_j \\
& - a_j^\dagger a_j a_j a_k + a_j^\dagger a_j a_k^\dagger a_j + a_j^\dagger a_j a_j^\dagger a_k - a_j^\dagger a_j a_j^\dagger a_k^\dagger \\
& - a_j a_j^\dagger a_j a_k + a_k^\dagger a_j + a_j^\dagger a_j a_k^\dagger a_j + a_j^\dagger a_k + a_j^\dagger a_j a_j^\dagger a_k - a_j a_j^\dagger a_j^\dagger a_k^\dagger \\
= \; & (3 a_j^\dagger a_j)(a_j^\dagger a_k + a_k^\dagger a_j) + 3 a_j^\dagger a_j \\
& - a_j^{\dagger 2} a_k^\dagger a_j - a_j^{\dagger 2} a_j^\dagger a_k + a_j^{\dagger 2} a_j^\dagger a_k^\dagger \\
& + a_j^2 a_j a_k - a_j^2 a_j a_k^\dagger - a_j^2 a_j^\dagger a_k
\end{aligned}
$$

$$
\begin{aligned}
& (\hat{a}_j - \hat{a}_j^\dagger)^2 (\hat{a}_k - \hat{a}_k^\dagger)(\hat{a}_l - \hat{a}_l^\dagger) \\
= \;& (a_j^{\dagger 2} + a_j^2 - a_j^\dagger a_j - a_j a_j^\dagger)(\hat{a}_k - \hat{a}_k^\dagger)(\hat{a}_l - \hat{a}_l^\dagger) \\
= \;& (a_j^{\dagger 2} + a_j^2 - a_j^\dagger a_j - a_j a_j^\dagger)(a_k a_l - a_k a_l^\dagger - a_k^\dagger a_l + a_k^\dagger a_l^\dagger) \\
= \;& a_j^{\dagger 2} a_k a_l - a_j^{\dagger 2} a_k a_l^\dagger - a_j^{\dagger 2} a_k^\dagger a_l + a_j^{\dagger 2} a_k^\dagger a_l^\dagger \\
& + a_j^2 a_k a_l - a_j^2 a_k a_l^\dagger - a_j^2 a_k^\dagger a_l + a_j^2 a_k^\dagger a_l^\dagger \\
& - a_j^\dagger a_j a_k a_l + a_j^\dagger a_j a_k a_l^\dagger + a_j^\dagger a_j a_k^\dagger a_l - a_j^\dagger a_j a_k^\dagger a_l^\dagger \\
& - a_j a_j^\dagger a_k a_l + a_j a_j^\dagger a_k a_l^\dagger + a_j a_j^\dagger a_k^\dagger a_l - a_j a_j^\dagger a_k^\dagger a_l^\dagger \\
= \;& a_j^{\dagger 2} a_k a_l - a_j^{\dagger 2} a_k a_l^\dagger - a_j^{\dagger 2} a_k^\dagger a_l + a_j^{\dagger 2} a_k^\dagger a_l^\dagger \\
& + a_j^2 a_k a_l - a_j^2 a_k a_l^\dagger - a_j^2 a_k^\dagger a_l + a_j^2 a_k^\dagger a_l^\dagger \\
& - a_j^\dagger a_j a_k a_l + a_j^\dagger a_j a_k a_l^\dagger + a_j^\dagger a_j a_k^\dagger a_l - a_j^\dagger a_j a_k^\dagger a_l^\dagger \\
& - a_j a_j^\dagger a_k a_l + (a_j^\dagger a_j + 1) a_k a_l^\dagger + (a_j^\dagger a_j + 1) a_k^\dagger a_l - a_j a_j^\dagger a_k^\dagger a_l^\dagger \\
= \;& (2 a_j^\dagger a_j + 1)(a_k a_l^\dagger + a_k^\dagger a_l) \\
& + a_j^{\dagger 2} a_k a_l - a_j^{\dagger 2} a_k a_l^\dagger - a_j^{\dagger 2} a_k^\dagger a_l + a_j^{\dagger 2} a_k^\dagger a_l^\dagger \\
& + a_j^2 a_k a_l - a_j^2 a_k a_l^\dagger - a_j^2 a_k^\dagger a_l + a_j^2 a_k^\dagger a_l^\dagger \\
& - a_j^\dagger a_j a_k a_l - a_j^\dagger a_j a_k^\dagger a_l^\dagger - a_j a_j^\dagger a_k a_l - a_j a_j^\dagger a_k^\dagger a_l^\dagger
\end{aligned}
\tag{B.6}
$$

Appendix C

SLOPED SIDE WALL GENERATION FOR THIN NIOBIUM FILM

Recipe:

Gas: 18 sccm Oxygen and 42 sccm CF4

Pressure: 100mTorr

Plasma: 30 Watts and zero reflection

Time: 11 :45 minutes for ≈ 100 nm thickness Niobium film on top of intrinsic high resistivity Silicon wafer

Results:

45 degree slope with ≈ 10nm over-etch on the Silicon substrate as shown in Fig. C.1. Shorter etching time has the risk of under-etching the Niobium thin film as shown in Fig. C.2. Fig. C.3 shows significant overetch due to longer etching time.

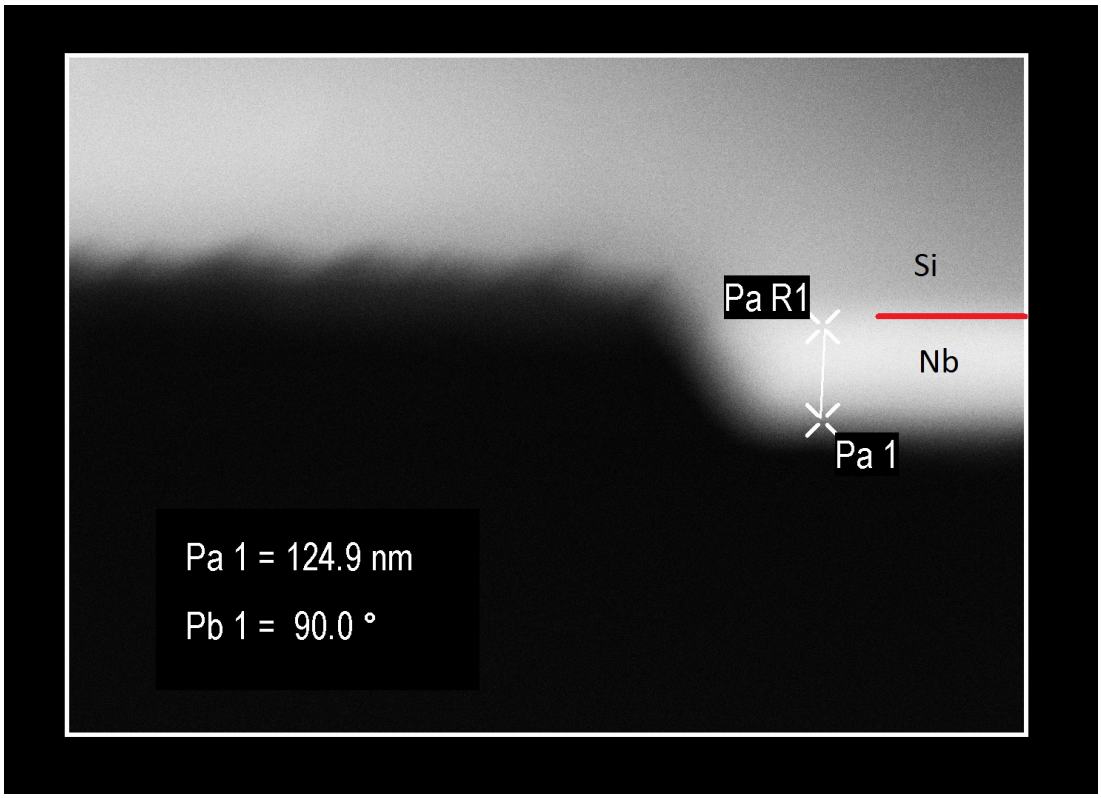

Figure C.1: SEM image of Nb film after 12 minutes plasma etch. There was $\approx 20nm$ over etch on the Si substrate, the side wall has about 45 degree slope

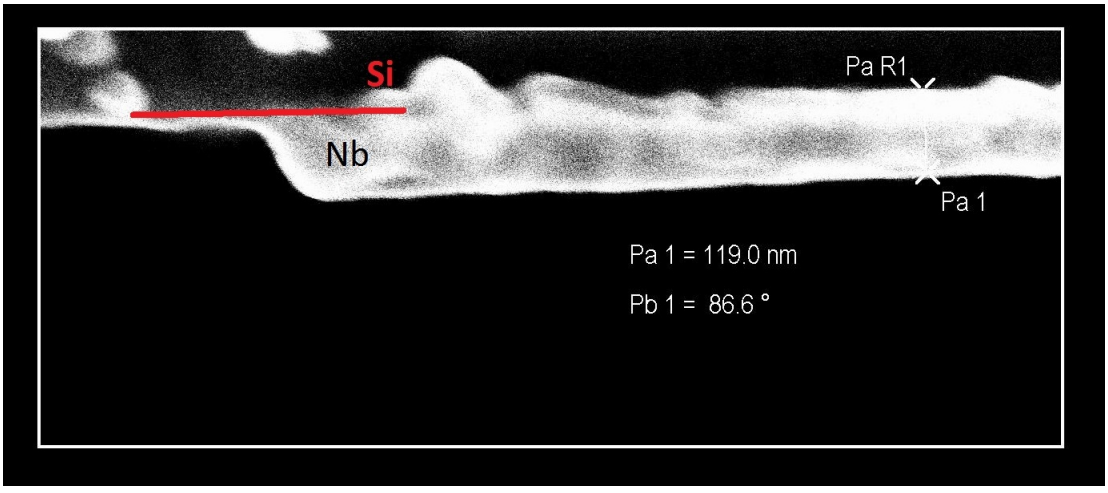

Figure C.2: SEM image of Nb film after 10 minutes plasma etch. The bright thin layer shows the Nb film was under etched

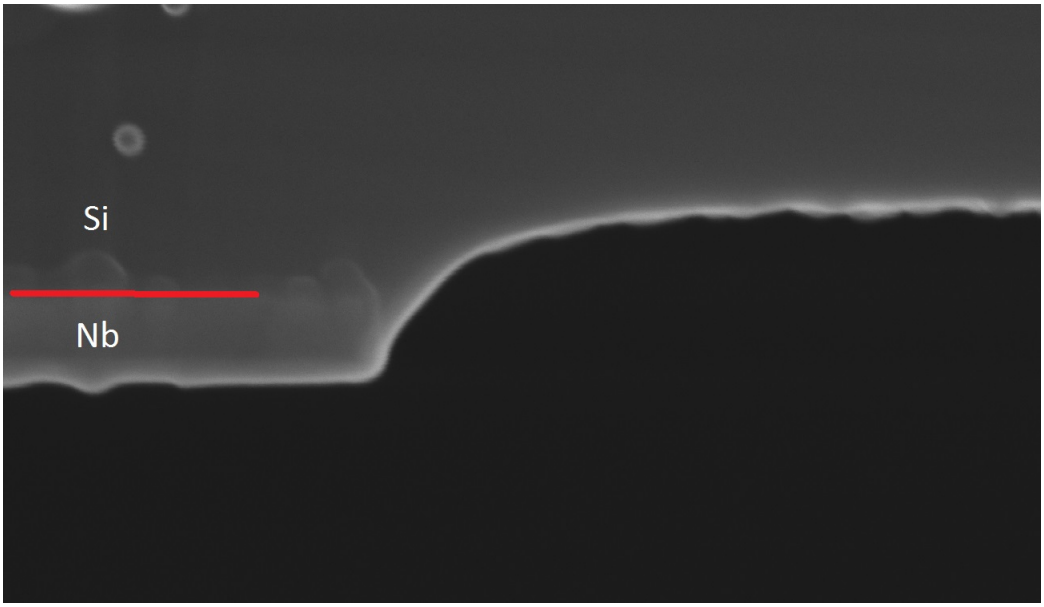

Figure C.3: SEM image of Nb film after 15 minutes plasma etch. Over-etch on the Si substrate was more than 100 nm

Appendix D

DOUBLE ANGLE EVAPORATION OF JOSEPHSON JUNCTION

Here I present an alternative method of evaporating Josephson junctions. It requires only one layer of PMMA 950 but needs to have the two layers evaporated at orthogonal angles. I came up with this idea at 2011 when I had problem fabricating Josephson junctions with consistent resistance. Having a consistent size of the junction is critical because resistance is a function of the size of the junction and the oxidation thickness. While writing this appendix I realized that a research group in China published similar idea on 2017 as in Ref. (16)

Comparing to shadow evaporation, double angle evaporation uses only one thicker resist layer. During evaporation the thin film deposited on the pattern in parallel with the evaporation angle will hit the substrate directly, but in the orthogonal evaporation angle the thin film will land on the side wall and is removed after development. Fig. D.1 (16) illustrates the principle of this method.

Recipe:

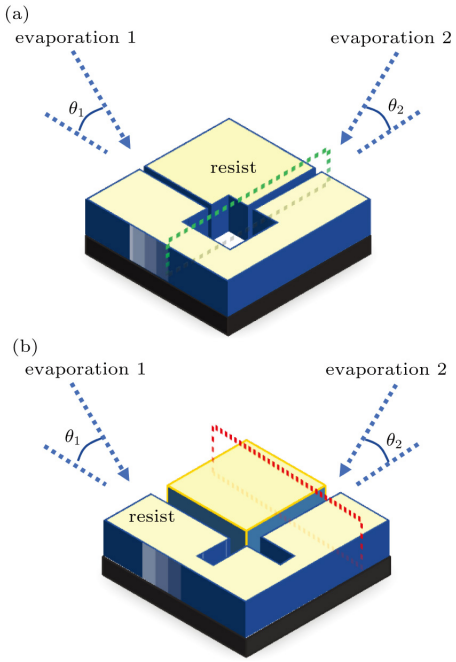

Figure D.1: Illustration of double angle evaporation

- PMMA 950 at spin speed of 1000rpm for 30 seconds.
- substrate tilted at $\theta \approx 30^\circ$ during evaporation.

After the first evaporation, patterns orthogonal to the tilting angle will leave a thin film on the wall, effectively narrowing the pattern width. This narrowing effect will be more significant with thicker film deposition or larger tilting angle. If equal pattern sizes are required the second deposition pattern could be generated wider to compensate for this effect.

Fig. D.3 show an image of a SET fabricated with double angle method on 2011. There is no island shdow as typical with shadow evaoration.

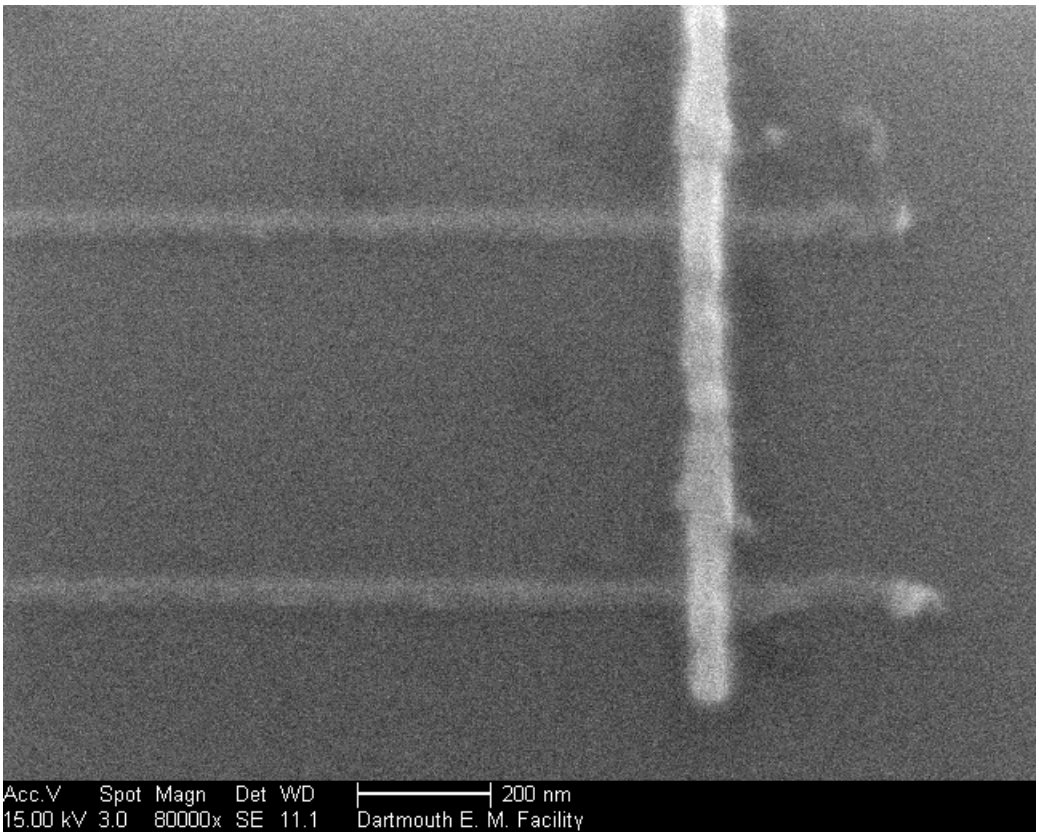

Figure D.2: SET fabricated with double angle method with line width of ≈ 50 *n*m

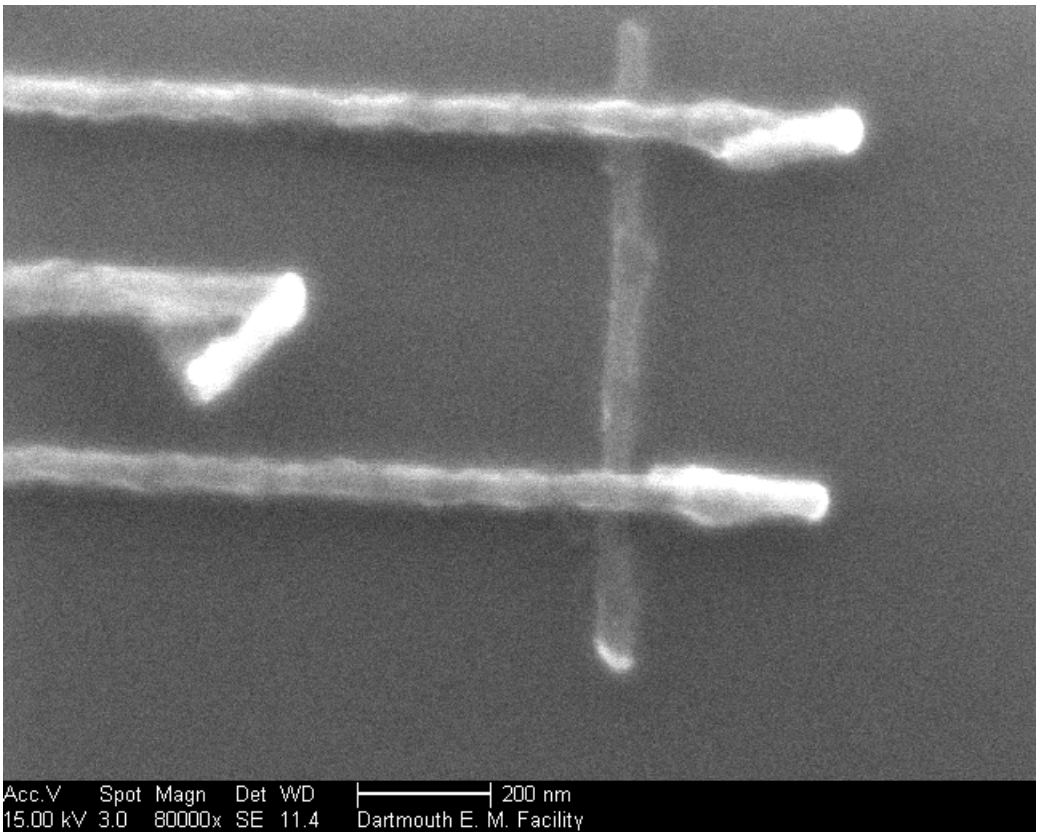

Figure D.3: SET fabricated with double angle method with larger tilting angle. The brighter parts to the right end of the horizontal patterns are Al film deposited on the resist wall, which become floating pieces after liftoff

Bibliography

[ble]

[2] Ambegaokar, V. and Baratoff, A. (1963). Tunneling between superconductors. *Phys. Rev. Lett.*, 10:486–489.

[3] Averin, D. V. and Likharev, K. K. (1986). Coulomb blockade of single-electron tunneling, and coherent oscillations in small tunnel junctions. *Journal of Low Temperature Physics*, 62(3):345–373.

[4] Beltran, M. A. C. (2010). *Development of a Josephson Parametric Amplifier for the Preparation and Detection of Nonclassical States of Microwave Fields.* Ph.d. diss.

[5] Chen, F., Li, J., Armour, A. D., Brahimi, E., Stettenheim, J., Sirois, A. J., Simmonds, R. W., Blencowe, M. P., and Rimberg, A. J. (2014). Realization of a single-cooper-pair josephson laser. *Phys. Rev. B*, 90:020506.

[6] Clark, J. B., Lecocq, F., Simmonds, R. W., Aumentado, J., and Teufel, J. D. (2016). Observation of strong radiation pressure forces from squeezed light on a mechanical oscillator. *Nature Physics*, 12:683 EP –.

[7] Clerk, A. A., Devoret, M. H., Girvin, S. M., Marquardt, F., and Schoelkopf, R. J. (2010). Introduction to quantum noise, measurement, and amplification. *Rev. Mod. Phys.*, 82:1155–1208.

[8] Colless, J. I., Mahoney, A. C., Hornibrook, J. M., Doherty, A. C., Lu, H., Gossard, A. C., and Reilly, D. J. (2013). Dispersive readout of a few-electron double quantum dot with fast rf gate sensors. *Phys. Rev. Lett.*, 110:046805.

[9] Court, N. A., Ferguson, A. J., and Clark, R. G. (2008). Energy gap measurement of nanostructured aluminium thin films for single cooper-pair devices. *Superconductor Science and Technology*, 21(1):015013.

[10] Dolan, G. J. (1977). Offset masks for liftâĂŘoff photoprocessing. *Applied Physics Letters*, 31(5):337–339.

[11] Fulton, T. A. and Dolan, G. J. (1987). Observation of single-electron charging effects in small tunnel junctions. *Phys. Rev. Lett.*, 59:109–112.

[12] GÃűppl, M., Fragner, A., Baur, M., Bianchetti, R., Filipp, S., Fink, J. M., Leek, P. J., Puebla, G., Steffen, L., and Wallraff, A. (2008). Coplanar waveguide resonators for circuit quantum electrodynamics. *Journal of Applied Physics*, 104(11):113904.

[13] Grabert, H. and Devoret., M. H. (1992). *Single charge tunneling: Coulomb blockage phenomena in nanostructures*. New York: Plenum Press.

[14] Griffiths, D. J. (2004). *Introduction to Quantum Mechanics (2nd Edition)*. PEARSON.

[15] gupta Ramesh Garg Inder Bahl Prakash Bhartia, K. C. (1996). *Microstrip Lines and Slotlines 2nd Ed.* Artech House Poblisher.

[16] Hai-Feng, Z. K. L. M.-M. L. Q. Y. and Yang, Y. (2017). Bridge-free fabrication process for $al/alox/al$ josephson junctions. *Chinese Physics B*, 7(26).

[17] Hover, D., Chen, Y.-F., Ribeill, G. J., Zhu, S., Sendelbach, S., and McDermott, R. (2012). Superconducting low-inductance undulatory galvanometer microwave amplifier. *Applied Physics Letters*, 100(6):063503.

[18] Jin, B., Yuan, J., Wang, K., Sang, X., Yan, B., Wu, Q., Li, F., Zhou, X., Zhou, G., Yu, C., Lu, C., Yaw Tam, H., and Wai, P. K. A. (2015). A comprehensive theoretical model for on-chip microring-based photonic fractional differentiators. *Scientific Reports*, 5:14216 EP –. Article.

[19] Josephson, B. (1962). Possible new effects in superconductive tunnelling. *Physics Letters*, 1(7):251 – 253.

[20] JOYEZ, P. (2010). *LE TRANSISTOR A UNE PAIRE DE COOPER : UN SYSTEME QUANTIQUE MACROSCOPIQUE*. Ph.d. diss.

[21] Kajfez, D. and Hwan, E. J. (1984). Q-factor measurement with network analyzer. *IEEE Transactions on Microwave Theory and Techniques*, 32(7):666–670.

[22] LaHaye, M. D., Suh, J., Echternach, P. M., Schwab, K. C., and Roukes, M. L. (2009). Nanomechanical measurements of a superconducting qubit. *Nature*, 459:960 EP –.

[23] Macha, P., van der Ploeg, S. H. W., Oelsner, G., IlâĂŹichev, E., Meyer, H.-G., WÃijnsch, S., and Siegel, M. (2010). Losses in coplanar waveguide resonators at millikelvin temperatures. *Applied Physics Letters*, 96(6):062503.

[24] Martinis, J. M., Devoret, M. H., and Clarke, J. (1987). Experimental tests for the quantum behavior of a macroscopic degree of freedom: The phase difference across a josephson junction. *Phys. Rev. B*, 35:4682–4698.

[25] Mueller, F., Schouten, R. N., Brauns, M., Gang, T., Lim, W. H., Lai, N. S., Dzurak, A. S., van der Wiel, W. G., and Zwanenburg, F. A. (2013). Printed circuit board metal powder filters for low electron temperatures. *Review of Scientific Instruments*, 84(4):044706–044706–7.

[26] Nabity, J. (1977). http://www.jcnabity.com/. *Applied Physics Letters*, 31(5):337–339.

[27] Nyquist, H. (1928). Thermal agitation of electric charge in conductors. *Phys. Rev.*, 32:110–113.

[28] Pozar, D. M. (1989). *Microwave Engineering*. John wiley Sons, INC.

[29] Ribeill, G. J., Hover, D., Chen, Y.-F., Zhu, S., and McDermott, R. (2011). Superconducting low-inductance undulatory galvanometer microwave amplifier: Theory. *Journal of Applied Physics*, 110(10):103901.

[30] Rimberg, A. J., Blencowe, M. P., Armour, A. D., and Nation, P. D. (2014). A cavity-cooper pair transistor scheme for investigating quantum optomechanics in the ultrastrong coupling regime. *New Journal of Physics*, 16(5):055008.

[31] Rossi, M., Kralj, N., Zippilli, S., Natali, R., Borrielli, A., Pandraud, G., Serra, E., Di Giuseppe, G., and Vitali, D. (2018). Normal-mode splitting in a weakly coupled optomechanical system. *Phys. Rev. Lett.*, 120:073601.

[32] Schoelkopf, R. J., Wahlgren, P., Kozhevnikov, A. A., Delsing, P., and Prober, D. E. (1998). The radio-frequency single-electron transistor (rf-set): A fast and ultrasensitive electrometer. *Science*, 280(5367):1238–1242.

[33] Schuster, D. I. (2007). *Circuit Quantum Electrodynamics*. Ph.d. diss., New Haven CT.

[34] Shahid, S., Ball, J. A. R., Wells, C. G., and Wen, P. (2011). Reflection type q-factor measurement using standard least squares methods. *IET Microwaves, Antennas Propagation*, 5(4):426–432.

[35] Sillanpää, M. A., Roschier, L., and Hakonen, P. J. (2004). Inductive single-electron transistor. *Phys. Rev. Lett.*, 93:066805.

[36] Teufel, J. D., Li, D., Allman, M. S., Cicak, K., Sirois, A. J., Whittaker, J. D., and Simmonds, R. W. (2011). Circuit cavity electromechanics in the strong-coupling regime. *Nature*, 471:204 EP –.

[37] Tinkham, M. (2004). *Introduction to Superconductivity: Second Edition*. DOVER.

[38] Tosi, L., Vion, D., and le Sueur, H. (2017). Design of a Cooper pair box electrometer for application to solid-state and astroparticle physics. *ArXiv e-prints*.

[39] Wallraff, A., Schuster, D. I., Blais, A., Frunzio, L., Majer, J., Devoret, M. H., Girvin, S. M., and Schoelkopf, R. J. (2005). Approaching unit visibility for control of a superconducting qubit with dispersive readout. *Phys. Rev. Lett.*, 95:060501.

[40] Williams, K. R., Gupta, K., and Wasilik, M. (2003). Etch rates for micromachining processing-part ii. *Journal of Microelectromechanical Systems*, 12(6):761–778.

[41] Williams, K. R. and Muller, R. S. (1996). Etch rates for micromachining processing. *Journal of Microelectromechanical Systems*, 5(4):256–269.

[42] Wilson, C. M., Duty, T., Sandberg, M., Persson, F., Shumeiko, V., and Delsing, P. (2010). Photon generation in an electromagnetic cavity with a time-dependent boundary. *Phys. Rev. Lett.*, 105:233907.

[43] Yuan, M., Yang, Z., Savage, D. E., Lagally, M. G., Eriksson, M. A., and Rimberg, A. J. (2012). Charge sensing in a si/sige quantum dot with a radio frequency superconducting single-electron transistor. *Applied Physics Letters*, 101(14):142103.